

# **Modeling of microstructure evolution in aluminum alloys during hot extrusion**

Von der Fakultät Maschinenbau  
der Technischen Universität Dortmund  
zur Erlangung des Grades eines  
Doktor-Ingenieurs  
(Dr.-Ing.)  
genehmigte Dissertation

von

**Farhad Parvizian**

Dissertation eingereicht am:  
Tag der mündlichen Prüfung:

13. Januar 2011  
08. April 2011

Referent:  
Korreferenten:

Prof. Dr. rer. nat. Bob Svendsen  
Prof. Dr.-Ing. Rolf Mahnken  
Jun. Prof. Björn Kiefer, Ph.D.

Financial support for the current work from the German Science Foundation (DFG) in the framework of the Cooperative Research Center 30 (TRR 30) "Process-integrated manufacturing of functionally graded structures on the basis of thermomechanically coupled phenomena" is gratefully acknowledged.

The examination commission:

Prof. Dr. rer. nat. Bob Svendsen, supervisor

Jun. Prof. Björn Kiefer, Ph.D.

Prof. Dr.-Ing. Rolf Mahnken

Prof. Dr.-Ing. Dirk Biermann

Prof. Dr.-Ing. A. Erman Tekkaya, chairman

# Contents

<b>Summary</b>	<b>vii</b>
<b>1 Introduction</b>	<b>1</b>
1.1 Aluminum alloys . . . . .	1
1.2 Extrusion of aluminum alloys . . . . .	1
1.3 Objective of this thesis . . . . .	2
<b>2 Thermomechanical modeling and simulation of aluminum alloy behavior during extrusion and cooling</b>	<b>7</b>
2.1 Introduction . . . . .	7
2.2 Material model . . . . .	8
2.3 Numerical simulation . . . . .	10
2.4 Results . . . . .	14
2.5 Summary and conclusions . . . . .	18
<b>3 Thermomechanically coupled modeling and simulation of hot metal forming processes using the adaptive remeshing method</b>	<b>21</b>
3.1 Introduction . . . . .	21
3.2 Material modeling . . . . .	22
3.3 Algorithmic formulation . . . . .	28
3.4 Boundary, contact and friction conditions . . . . .	30
3.5 Numerical aspects and adaptive remeshing . . . . .	31
3.6 Applications and results . . . . .	34
3.7 Conclusions . . . . .	37
<b>4 Modeling of dynamic microstructure evolution of EN AW-6082 alloy during hot forward extrusion</b>	<b>43</b>
4.1 Introduction . . . . .	43
4.2 Microstructure characterization . . . . .	44
4.3 Material Model . . . . .	52
4.4 Simulation of microstructure evolution . . . . .	54
4.5 Results and discussion . . . . .	58

<b>5</b>	<b>Comparison of two models for material behavior of Al-alloys during thermo-mechanical processing</b>	<b>59</b>
5.1	Introduction . . . . .	59
5.2	Material model framework . . . . .	60
5.3	First simple model . . . . .	64
5.4	Simple subgrain-based hardening model . . . . .	65
5.5	Algorithmic formulation . . . . .	67
5.6	Results . . . . .	69
5.7	Summary and conclusions . . . . .	73
<b>A</b>	<b>Basics of continuum mechanics</b>	<b>75</b>
A.1	Kinematics . . . . .	75
A.2	Strain . . . . .	76
A.3	Stress . . . . .	77
A.4	Balance equations . . . . .	77
<b>B</b>	<b>Microstructure of deformed materials</b>	<b>79</b>
B.1	Deformed state . . . . .	79
B.2	Recovery . . . . .	80
B.3	Recrystallization . . . . .	81
B.4	Grain growth . . . . .	82
B.5	Measurement of microstructure . . . . .	82
	<b>References</b>	<b>85</b>
	<b>Acknowledgments</b>	<b>91</b>
	<b>Curriculum Vitae</b>	<b>93</b>

# List of Figures

1.1	Components of direct extrusion process. . . . .	2
2.1	Finite element model of extrusion. . . . .	11
2.2	a) Penetration of the workpiece into the die without mesh refinement. b) Accurate contact between the die and the workpiece achieved with mesh refinement. . . . .	12
2.3	The Python-based system for mesh refinement and adaptivity developed in combination with FE-solver Abaqus. . . . .	13
2.4	Initial mesh for the adaptive approach (top) and geometric mesh refinement procedure (bottom). . . . .	14
2.5	Effect of contact heat conduction between the billet and the container on temperature (K) distribution of the workpiece a) without contact conduction, b) with contact conduction. . . . .	16
2.6	Equivalent plastic strain of the workpiece: a) without contact conduction, b) with applying contact conduction. . . . .	17
2.7	Displacement of material during extrusion simulation: a) without friction, b) with friction. . . . .	18
2.8	Temperature distribution (K) in the extruded profile: a) before cooling process, b) after 450 seconds of cooling, c) after 900 seconds of cooling. The legend in c) is the same as in b). . . . .	19
3.1	A linear segment of the master surface in contact with a node of slave surface in finite-sliding contact simulation. . . . .	30
3.2	Simulation of extrusion process using adaptive mesh refinement. . . . .	31
3.3	Element distortion and uneven contact surface during simulation of the the forging process without applying remeshing techniques. . . . .	32
3.4	Mesh topology in simulation of the forging process using remeshing scheme. . . . .	32
3.5	Remeshing system developed with the help of Python programming . . . . .	33
3.6	Geometry and configuration for simulation of extrusion process . . . . .	35
3.7	FE-discretization and remeshing for the extrusion simulation. I) mesh at beginning of one step, II) mesh at the end of the same step, III) mesh after new meshing of the deformed geometry of part II. . . . .	36
3.8	Distribution of equivalent plastic strain in simulation of extrusion process. . . . .	37
3.9	Distribution of non-dimensional subgrain size during simulation of extrusion process in absence of friction. . . . .	37

3.10	Distribution of non-dimensional subgrain size during simulation of the extrusion process with frictional interactions. . . . .	38
3.11	Evolution of non-dimensional subgrain size during the extrusion process in the die exit, the dead material zone (DMZ) and the main deformation zone (MDZ). . . . .	38
3.12	Experimental results showing dead material zone (DMZ), main deformation zone (MDZ), shear intensive zone (SIZ) and die exit area. . . . .	39
3.13	Geometry and configuration for simulation of forging process . . . . .	39
3.14	Development of mesh topology during simulation of forging process based on remeshing of deformed geometry in each step. . . . .	40
3.15	Distribution of temperature in simulation of forging process. . . . .	40
3.16	Distribution of equivalent plastic strain in simulation of forging process. . . . .	40
3.17	Distribution of volume fraction of martensite in simulation of forging process. . . . .	41
3.18	Grinding surface pattern of real structure obtained from experimental results of forging process. . . . .	41
4.1	Small-scale forward extrusion setup (Güzel et al., 2011). . . . .	45
4.2	True stress-true strain response of EN AW-6082 at 723 K for different cross head displacement rates. . . . .	46
4.3	True stress-true strain response of EN AW-6082 at cross head displacement rate of 1.0 mm/s for different temperatures. . . . .	47
4.4	Schematic representation of the small-scale extrusion with position of two measured paths (black path and red path). . . . .	47
4.5	High-angle ( $>15^\circ$ ) (left) and low-angle ( $<5^\circ$ ) (right) grains of undeformed material (O) obtained by the EBSD measurement. . . . .	48
4.6	High-angle ( $>15^\circ$ ) grains of investigated points (black path) of the extrusion butt obtained by the EBSD measurement. . . . .	49
4.7	High-angle ( $>15^\circ$ ) grains of investigated points (red path) of the extrusion butt obtained by the EBSD measurement. . . . .	49
4.8	Low-angle ( $<5^\circ$ ) grains of investigated points (black path) of the extrusion butt obtained by the EBSD measurement. . . . .	50
4.9	Low-angle ( $<5^\circ$ ) grains of investigated points (red path) of the extrusion butt obtained by the EBSD measurement. . . . .	50
4.10	The median grain size of undeformed material and six measured points of the black path in the billet obtained by the EBSD measurements. . . . .	51
4.11	The mean low-angle boundary misorientation ( $<15^\circ$ ) of undeformed material and measured points of the black path in the billet obtained by the EBSD measurements. . . . .	51
4.12	The mean low-angle boundary misorientation ( $<15^\circ$ ) of undeformed material and measured points of the red path in the billet obtained by the EBSD measurements. . . . .	52

4.13	The median grain size measured points of the red path in the billet obtained by the EBSD measurements. . . . .	52
4.14	Evolution of grain size at point 2 for different values of $c_\delta$ . . . . .	55
4.15	Simulated distribution of equivalent plastic strain in the billet at the end of the extrusion process. . . . .	56
4.16	Simulated distribution of temperature ( $^\circ\text{C}$ ) in the billet during extrusion process. . . . .	57
4.17	Simulated distribution of grain size ( $\mu\text{m}$ ) in the aluminum billet at the end of the extrusion process. . . . .	57
5.1	Comparison of experimental (lines with triangles) and simulation results of the first model (no hardening) for EN AW-6082 at 623 K for different head displacement rates. . . . .	69
5.2	Comparison of experimental (lines with triangles) and simulation results of the first model (no hardening) for EN AW-6082 at 673 K for different head displacement rates. . . . .	70
5.3	Comparison of experimental (lines with triangles) and simulation results of the first model (no hardening) for EN AW-6082 at 723 K for different head displacement rates. . . . .	70
5.4	Comparison of experimental (lines with triangles) and simulation results of the Orowan based hardening model for EN AW-6082 at 623 K for different head displacement rates. . . . .	71
5.5	Comparison of experimental (lines with triangles) and simulation results of the Orowan based hardening model for EN AW-6082 at 673 K for different head displacement rates. . . . .	71
5.6	Comparison of experimental (lines with triangles) and simulation results of the Orowan based hardening model for EN AW-6082 at 723 K for different head displacement rates. . . . .	72
5.7	Comparison of experimental and simulation results of the ram force during the extrusion process for the two presented models with and without hardening (by courtesy of the IUL, TU Dortmund). . . . .	72
A.1	The motion of a continuum body from its reference configuration $\Omega_r$ to the current configuration $\Omega_c$ in Euclidean space. . . . .	75
B.1	Edge dislocation in crystal structure. Burgers vector $\mathbf{b}$ represents the magnitude of the structural defect and is perpendicular to the dislocation line in the case of edge dislocation. . . . .	80
B.2	Screw dislocation in crystal structure. Burgers vector $\mathbf{b}$ is parallel to dislocation line in the case of screw dislocation. . . . .	81

# List of Tables

2.1	Material parameters of EN AW-6060 for Johnson-Cook model. . . . .	15
3.1	Thermoelastic and inelastic material parameters of the aluminum alloy EN AW-6060 used for simulation of extrusion process. . . . .	26
3.2	Single-phase thermoelastic, inelastic and phase transformation-related material parameter values used for simulation of low alloy steel. . . . .	28
4.1	Material parameters of the aluminum alloy EN AW-6082 used for simulation of extrusion process. . . . .	55
4.2	Comparison between experimental and simulated results for grain size ( $\mu\text{m}$ ) at six investigated points of the black path. . . . .	58
4.3	Comparison between experimental and simulated results for grain size ( $\mu\text{m}$ ) at six investigated points of the red path. . . . .	58



# Summary

Modeling and simulation of microstructure evolution of aluminum alloys in hot forming processes give an insight into the material properties of the final product and enable us to optimize or customize the material behavior of the final product by controlling the microstructure evolutions during and after forming process. An accurate and robust simulation of microstructure and material behavior during hot large deformation processes requires consideration of several numerical and structural aspects as well as an appropriate material model. The current work deals with the numerical aspects of the simulation of hot forming processes on the one hand, and with the material and microstructure modeling of such processes on the other.

The first chapter gives an overview of this work and related researches. Here the different aspects of modeling and simulation of the extrusion processes are discussed. Furthermore a summary of the recent models and efforts for modeling the microstructure evolution in hot forming processes is given in this chapter.

In the second chapter of this thesis attention is focused on aluminum alloys of the 6000 series (Al-Mg-Si) and 7000 series (Al-Zn-Mg). Here, a number of aspects of the structural simulation as well as that of extrusion as a thermomechanical process are considered. These aspects include contact and adaptive mesh refinement, heat transfer inside the billet, heat transfer between the workpiece and the container, frictional dissipation, mechanical energy and surface radiation.

The third chapter presents a general framework for modeling the material behavior of metals in forming processes. Moreover, to overcome the problems of simulation of large forming processes a new remeshing scheme is presented. Here the mesh refinement applied in the second chapter is replaced by the new remeshing of the deformed geometry. The application of the framework and developed simulation techniques in two forming processes is set out. In the new meshing scheme, in order to reduce the numeric costs and increase the accuracy of the results, the mesh quality is controlled during the simulation and the simulation is stopped when the quality of mesh is less than the allowed value. Simulation results for the microstructure development as a function of process conditions demonstrate the sensitivity of microstructure development to these conditions. Comparison of the simulation results for the microstructure evolution with corresponding experimental results show good qualitative agreement.

Chapter four focuses on the comparison of experimental and simulation results as well as a brief description of the applied model for prediction and simulation of the evolution of microstructure, in particular the evolution of grains, during hot forming processes of aluminum alloy EN AW-6082. The model is a physically motivated phenomenological model based on internal state dependent variables. The microstructure evolution is a temperature dependent process and is simulated in a fully-coupled thermomechanical process by help of the Finite Element software Abaqus. The results are compared and verified with experimental results obtained by the EBSD measurement of a small-scale extrusion process established for scientific purposes. The simulation results are in reasonable agreement with the experimental ones.

In the final chapter two models are formulated for the thermoelastic, viscoplastic behavior of aluminum alloys and applied to the case of extrusion. The first model is based on a common semi-empirical form of the (scalar) flow rule in the extrusion community and neglects all effects of the microstructure on the hardening behavior. This results in an ideal viscoplastic model. The second model formulates a scalar flow rule as based on the Taylor assumption. Furthermore the effect of the subgrain structure development on the inelastic free energy and the flow stress are considered. The predictions of both of these models for simple benchmark problems involving material testing and extrusion are compared.

# Zusammenfassung

Die Modellierung und Simulation der Mikrostrukturentwicklung von Aluminiumlegierungen in Warmumformverfahren liefern einen Einblick in die Materialeigenschaften des Endproduktes und ermöglichen die Optimierung und Anpassung des Materialverhaltens dieses Endproduktes durch die Steuerung der Mikrostrukturentwicklungen während und nach dem Umformprozess. Für die präzise und stabile Simulation der Mikrostruktur und des Materialverhaltens während Warmumformungsprozessen müssen zahlreiche numerische und strukturelle Aspekte berücksichtigt, sowie ein passendes Materialmodell gewählt werden. Die vorliegende Arbeit beschäftigt sich einerseits mit den numerischen Aspekten der Simulation von Warmumformungsprozessen, andererseits mit der Material- und Mikrostrukturmodellierung solcher Prozesse.

Das erste Kapitel gibt einen Überblick über diese Arbeit und ihr verwandte Forschungsgebiete. Hier werden die verschiedenen Aspekte der Modellierung und Simulation des Strangpressprozesses diskutiert. Im Übrigen umfasst dieses Kapitel eine Zusammenstellung der aktuellen Modelle zur Mikrostrukturentwicklung beim Warmumformungsprozess, ebenso wie die neuesten Bemühungen zur Modellierung dieser.

Im zweiten Kapitel dieser Doktorarbeit liegt das Augenmerk auf den Aluminiumlegierungen der Serien 6000 (Al-Mg-Si) und 7000 (Al-Zn-Mg). Es wird eine Reihe von Aspekten der Struktursimulation sowie des Strangpressens als thermomechanischen Prozess berücksichtigt. Diese Gesichtspunkte beinhalten den Kontakt, die adaptive Netzverfeinerung, die Wärmeübertragung im Inneren des Walzblocks, den Wärmeaustausch zwischen dem Werkstück und dem Behälter, den Reibungsverlust, die mechanische Energie und die Oberflächenstrahlung.

Im dritten Kapitel werden allgemeine Rahmenbedingungen für die Modellierung des Materialverhaltens von Metallen in Umformprozessen dargestellt. Ferner wird, um Simulationsprobleme von Umformprozessen zu überwinden, ein neues Modell zur Neuvernetzung präsentiert. Hier wird die im zweiten Kapitel dargestellte Netzverfeinerung durch die neue Vernetzung der deformierten Geometrie ersetzt. Die Anwendung der Grundstruktur und der entwickelten Simulationstechniken auf zwei Umformprozesse wird präsentiert. Um die numerischen Kosten zu reduzieren und die Ergebnisgenauigkeit zu verbessern, wird die Qualität des Netzes während der Simulation kontrolliert und die Simulation angehalten, falls die Netzqualität einen erlaubten Wert unterschreitet. Die Simulationsergebnisse für die Mikrostrukturentwicklung als Funktion der Prozessbedingungen demonstrieren die Empfindlichkeit der Mikrostrukturentwicklung gegenüber diesen Bedingungen. Ein Vergleich der Simulationsergebnisse für die Mikrostrukturentwicklung mit den jeweiligen experimentellen Werten zeigt gute qualitative Übereinstimmungen.

Im vierten Kapitel liegt der Fokus auf dem Vergleich der Ergebnisse aus Experiment und Simulation. Weiterhin wird ein Modell zur Vorhersage und Simulation der Mikrostrukturentwicklung, insbesondere der Kornentwicklung der Aluminiumlegierung EN AW-6082 während Warmumformprozessen kurz beschrieben. Dieses Modell ist ein physikalisch motiviertes phä-

nomenologisches Modell, welches auf vom inneren Zustand abhängigen Variablen basiert. Die Mikrostrukturentwicklung ist ein temperaturabhängiger Prozess und wird mit Hilfe der Finite Elemente Software Abaqus in einem vollständig gekoppelten thermomechanischen Verfahren simuliert. Die Ergebnisse werden mit experimentellen Werten, bestimmt mit Hilfe einer EBSD Messung eines kleinmaßstäbigen Strangpressungsprozesses, der sich für wissenschaftliche Zwecke etabliert hat, abgeglichen und verifiziert. Die Simulationsergebnisse weisen eine zufriedenstellende Übereinstimmung mit den Experimentalergebnissen auf.

Im letzten Kapitel werden für das thermoelastische, viskoplastische Verhalten von Aluminiumlegierungen zwei Modelle formuliert und auf den Fall der Strangpressung angewendet. Das erste Modell basiert auf einer gängigen semiempirischen Form der (skalaren) Fließregel der Strangpressgemeinde und vernachlässigt alle Effekte der Mikrostruktur auf das Aushärtungsverhalten. Dies resultiert in einem idealen viskoplastischen Modell. Im zweiten Modell wird eine skalare Fließregel basierend auf der Taylorannahme formuliert, außerdem werden der Einfluss der Subkornstrukturentwicklung auf die freie inelastische Energie sowie die Fließspannung berücksichtigt. Die Vorhersagen dieser beiden Modelle für einfache Benchmarkprobleme aus der Materialprüfung und der Strangpressung werden verglichen.

# Chapter 1

## Introduction

### 1.1 Aluminum alloys

Reducing the weight of structures has been the subject of industrial interests for many years. Low density aluminum alloys with high formability and strength are widely used to produce light-weight structures in the automotive and aerospace manufacturing industry. Aluminum alloys are categorized based on their composed elements. The main elements used in aluminum alloys are magnesium, copper, zinc, manganese and silicon. Each of these elements influences the strength and formability of the alloy. The aluminum alloy classes range from 1000 to 8000.

Aluminum alloys of series 6000 and 7000 are more often used in the automotive and aerospace industry. Alloys of the 6000 series have magnesium and silicon as main composed elements and can be hardened by precipitation. Alloys of the 7000 series have zinc as the main alloying element and can reach the highest strength among all of aluminum alloys by precipitation hardening.

The components made of aluminum alloys are produced in different technological processes such as rolling, casting and extrusion. Each of these processes influences the material behavior of the final product. The following section introduces the general aspects of the extrusion process of aluminum alloys.

### 1.2 Extrusion of aluminum alloys

Extrusion as a technological process is used to produce profiles with constant cross sections from materials such as aluminum, copper, stainless steel and various types of plastic. The advantages of aluminum and its alloys include high ductility, due to its face-center cubic crystal structure, making it particularly suitable for complex extrusion processes. Additionally, the ideal ratio of Young's modulus to mass density in aluminum makes it suitable for a wide range of application in automotive and aircraft manufacturing and for lightweight construction in general.

In industry there are mainly two types of extrusion processes: direct extrusion and indirect extrusion. In both cases, the extrusion tool consists of the parts shown in Figure 1.1. In the case of direct extrusion the material is forced to flow through the die by the ram, whereas in indirect extrusion the billet and the container move together and there is no relative displacement between billet and the container. This results in different material flow and consequently in different material properties of the extrusion in each case.

During the extrusion process, first of all the billet is warmed up in an oven up to a temperature which depends on the type of the alloy and process parameters. The billet will be kept at this

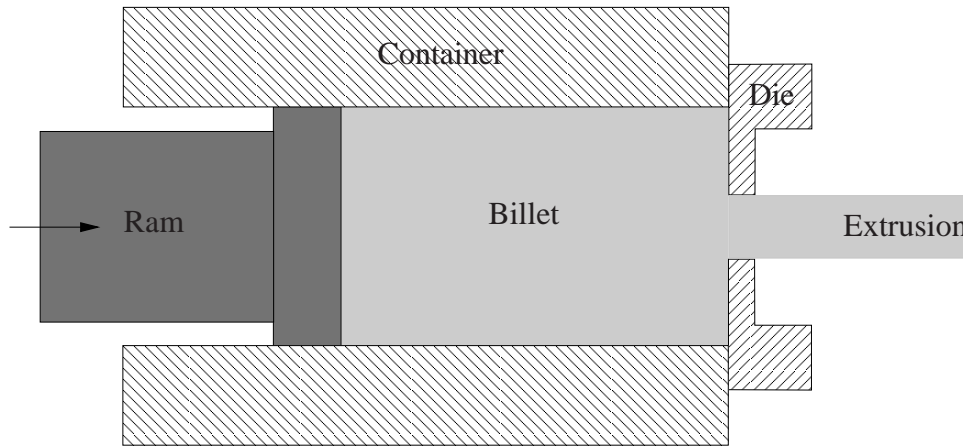


Figure 1.1: Components of direct extrusion process.

temperature for several hours to reach homogeneous material properties. After this step, the block will be inserted into the container and pressed by ram through the die. There are various types of profiles which can be produced by extrusion process, for example rods, hollow sections, semihollow sections and flat sections.

In the current work only direct extrusion, which is most widely used, is considered for the investigation. In order to reduce the complexity of simulation and also the undesired structural effects, only extrusion of rod is taken into account.

### 1.3 Objective of this thesis

The process of extrusion in combination with heat treatment and further processing, e.g. bending, leads to a complex development in the material's microstructure. An understanding of this development in each processing step, especially during extrusion and heat treatment, allows one to influence and control the resulting material properties.

Material properties of metal forming products are of industrial interest for product optimization or as the initial state for further processing purposes such as annealing. Simulation of hot forming processes by applying the finite element method (FEM) has been the subject of many recent works. Large plastic deformations and high temperature of the extrusion process cause developments in the microstructure of the material.

Finite element simulation of forming processes is now well established at macro level (e.g. Kobayashi et al., 1989) for optimization and prediction of process parameters for example, but does not provide enough information on the material properties of the final product. In order to obtain the material behavior of the final product, it is necessary to study the microstructure development of the material during forming processes. There are generally two approaches for the simulation of microstructure evolution during forming processes: phenomenological models and physically based models (Grong and Shercliff, 2002). In phenomenological models the final state of the recrystallized structure is modeled in a post-processing process without considering any evolution law for the microstructure. The empirical Johnson–Mehl–Avrami–Kolmogorov (JMAK) relation is widely used to determine the recrystallized grain size (Bontcheva et al.,

2006; Grass et al., 2003). The JMAK relation for nucleation and growth transformations works very well for most solid state transformations but regularly fails when applied to recrystallization of plastically deformed metals (Rollett et al., 1989). In contrast to the phenomenological models, physically based models give more insight into the material behavior at micro-scale. In physically based models the internal state dependent variables are used to describe the state of the microstructure parameters during the process (Shercliff and Lovatt, 1999). The internal state variables are well suited for describing the microstructure properties in forming processes. The evolution law of internal state variables

$$\frac{dS_i}{dt} = f_i(S_{1,\dots,n}, \dot{\alpha}_p(t), T(\dot{\alpha}_p), \dots) \quad (1.1)$$

in metal forming applications is usually given as a function of internal state dependent variables  $S_i$  ( $i = 1, \dots, n$ ), rate of equivalent plastic strain  $\dot{\alpha}_p$  and the temperature  $T$ . In thermo-mechanically coupled processes the temperature increases significantly during the process. In fully coupled models of more complex processes in which microstructure evolution leads to heat generation, e.g. solidification, the evolution of temperature is given as a function of internal state dependent variables  $S_i$  as well as time  $t$ . In a fully coupled approach the constitutive relation for material behavior

$$\sigma_f = g(S_{1,\dots,n}, \alpha, \dot{\alpha}_p, T) \quad (1.2)$$

is microstructurally based and coupled directly with the state dependent variables  $S_i$  ( $i = 1, \dots, n$ ). An appropriate coupled approach is given by describing the flow stress of work hardened microstructure as a function of two internal state variables, dislocation density  $\rho$  and subgrain size  $\delta$ , and the size of Burgers vector  $b$  (Furu et al., 1996; Nes and Furu, 1995).

Shercliff and Lovatt (1999) have presented various physical and statistical approaches for the modeling of microstructure evolution in hot deformation. In physically based state variable models, the microstructure and property evolution are modeled explicitly. In statistical approaches the process conditions are linked empirically to the final microstructure. Furu et al. (1996) have offered a physically based model to describe the development of microstructure during hot forming processes which is later developed by Sellars and Zhu (2000) by applying the concept of free energy as the driving force of microstructure evolutions. In the work of Velay (2009) the JMAK equation is applied for recrystallization kinetics and the evolutions of subgrain size during hot extrusion of aluminum alloys is obtained only at steady-state condition ( $\delta_{ss}$ ). In another work, Furu et al. (1995) presented a comprehensive study of heavily deformed annealing behavior of aluminum alloys based on experimental investigation and modeling of subgrain growth as a reaction controlled by sub-boundary migration. This model is based on growth depending on annealing time and temperature and is therefore not able to predict the dynamic evolution of microstructure. Bontcheva and Petzov (2003) considered three different models for different recrystallization steps: static recrystallization, dynamic recrystallization and metadynamic recrystallization (depending on the magnitude of accumulated deformation energy). All of these three models are based on Avrami equation, but the time for 50% recrystallization  $t_{50}$  is obtained by different equation in each case. Jiang et al. (2007) simulated the microstructure evolution of aluminum alloy during hot forging processes and heat treatment. Since no classical dynamic recrystallization occurs in aluminum alloy Al-1% Mg, only the static

recrystallization is considered by Jiang et al. (2007). Vatne et al. (1996) presented a physically based model for modeling recrystallization after hot deformation of aluminum which is different to the models developed for recrystallization behaviour of steels. This model is based on the calculation of nuclei density in deformed material and the final recrystallization texture is obtained by calculating the contribution of different types of nucleation sites (grain boundaries, cube sites and particle stimulated nucleation). Baxter et al. (1999) studied the influence of transient strain-rate conditions on evolution of microstructure of aluminum alloy Al-1% Mg. The experimental investigations of Baxter et al. (1999) showed that the grain sizes under transient strain-rate result in smaller grains compared to the constant strain rate. In the work of Nes and Marthinsen (2002) a model based on statistical approach is presented for work hardening of fcc alloys during plastic deformation. In this model the flow stress is related directly to grain size and dislocation density within cells. Yassar et al. (2008) investigated the microstructure history effect during thermo-mechanical processes of aluminum alloys by means of TEM (transmission electron microscopy), SEM (scanning electron microscope) and EBSD (Electron backscatter diffraction) in an experimental work. De Pari Jr. and Misiolak (2008) and Hurley et al. (2009) studied the evolution of grain structure on the surface of aluminum alloys during rolling. Static recrystallization and peripheral coarse grain (PCG) growth are two effects which influence the surface grain size. Abedrabbo et al. (2007) presented a coupled thermo-mechanical model for the anisotropic behavior of aluminum alloys during hot forming processes. Their proposed model for the flow rule depends on strain and strain rate with temperature dependent parameters.

Microstructure developments are temperature dependent processes. For modeling these developments it is therefore required to consider a coupled thermo-mechanical model. Several constitutive laws have been used by different research groups. Duan and Sheppard (2004) have investigated the influence of the constitutive equation on the simulation of a hot rolling process. Duan and Sheppard (2003) have applied the isotropic viscoplastic Norton-Hoff law as the flow rule. Nes (1995) has used the hyperbolic sine law as the governing constitutive equation which is a purely empirical model suggested for metal forming processes such as hot rolling, forging and extrusion. This model is also employed by Sheppard (2006) for the prediction of structure during extrusion processes and also by Zhang et al. (2007) for material behavior of some new aluminum alloys in hot forming processes. In another work Bontcheva et al. (2006) have applied the “Shvarzbart” model for large deformations to describe the thermo-mechanical behavior of the material.

Thermo-mechanical modeling of the forming process requires a reliable numeric approach on the one hand and an appropriate material model on the other. Lagrangian approach, Eulerian approach, Arbitrary Lagrangian Eulerian (ALE) and meshless methods have been applied by different groups. Guo and Nakanishi (2003) have applied the rigid-plastic integralless–meshless method to the analysis of plane strain backward extrusion. In the works of Coupez et al. (1998) and Parvizian et al. (2009) adaptive refinement algorithms based on the Lagrangian approach are presented for simulation of large forming processes. Gautham et al. (2003) proposed a background mesh for 2D simulation of metal forming processes. Lou et al. (2008) have applied the Finite Volume Method to overcome the element distortion and contact problems occurring during the simulation of the extrusion process. Williams et al. (Williams et al., 2002) have also



applied finite volume methods on the unstructured mesh in simulation of forging and extrusion. The Eulerian approach has generally been used for the simulation of the steady state metal forming with the assumption that the die is entirely rigid which is not usually the case (Williams et al., 2002). Applying some remeshing or mesh refinement techniques is unavoidable when the Lagrangian approach is used for the simulation.

In chapter two of this thesis, attention is focused on certain aspects of the numerical simulation of extrusion and cooling including (1) contact and friction conditions, (2) adaptive mesh refinement, (3) thermo-mechanical behavior of material during extrusion and (4) conductive, convective and surface radiation cooling. The presented approach is based on a continuum thermodynamic model formulation for thermoelastic, thermoviscoplastic material behavior of metallic materials. Rather than the more realistic model of Sellars and Zhu (2000), the applied material model assumes for simplicity a Johnson-Cook-like approach for the evolution of the accumulated equivalent inelastic deformation as a function of the stress, accumulated inelastic deformation and temperature.

Chapter three presents a more realistic model for microstructure evolution of aluminum alloy in hot forming processes and also presents a remeshing scheme of the deformed geometry instead of the mesh refinement strategy which is introduced in the second chapter. This method is applied for two examples of metal forming: extrusion of aluminum and forging of steel. An accurate numeric simulation of these two processes requires appropriate material models. The material model presented in the chapter three is based on the isotropic thermoelastic viscoplastic approach. The corresponding model for each case in combination with the numerical implementation and the necessary modifications of the model for use with the remeshing system are discussed. These models are implemented as user material (UMAT) in the commercial FEM software Abaqus.

In chapter four the thermo-elastic visco-plastic empirical model presented in the previous chapter is used to describe the macroscopic behavior of the material and a physically based model is applied to model the evolution of microstructure properties as internal state dependent variables. In this chapter the focus lies on verifying and validating the model by experimental results obtained by the EBSD measurement of a small scaled extrusion process.

During industrial thermo-mechanical processing such as hot forging, rolling or extrusion, processing conditions drive an evolution of the dislocation and grain microstructures in the metallic materials of interest, resulting in a change of shape of the work piece. In the case of high stacking-fault energy materials such as aluminum alloys for example, mobile dislocations glide, cross-slip, and at higher temperatures, climb. Depending on the nature of the energetic and dissipative-kinetic mechanisms involved, dislocation motion results in the development of dislocation microstructures within existing grains consisting of dislocation-rich wall-like regions separating dislocation-poor cell-like regions, leading to subgrain formation.

Dislocations interacting with obstacles such as other dislocations, solutes, or precipitates, subgrain- or grain boundaries, result in various forms of hardening behavior. Face-center cubic (fcc) materials such as aluminum and its alloys are generally characterized by four stages of work hardening. Stage I (easy glide) represents a glide of dislocations over “long” distances, little interaction with other dislocations, and little hardening. Stage II is characterized by a linear

hardening rate and slight temperature-dependence. Stage III begins when cross-slip of screw dislocations is activated. Especially at low temperatures where climb is too slow, cross-slip is the major recovery mechanism. In general, both mechanisms will be important.

The interpretation of polycrystal hardening on the basis of single crystal behavior also involves the average grain size and the distribution of grain orientations, i.e. the texture. At least for pure fcc materials and for grain sizes much smaller than the specimen size, texture rather than grain size is important here in the sense that the distribution of grain orientations influences the distribution of active glide systems.

In the simplest case, one can regard the microstructure of a polycrystal to consist of (i) (high-angle) grain boundaries separating grains, (ii) (low-angle) subgrain boundaries separating subgrains within grains, (iii) dislocation walls separating cells within subgrains, (iv) individual dislocations, (v) solutes and (vi) precipitates.

From a phenomenological viewpoint, the behavior of polycrystalline aluminum alloys during technological processes like extrusion is fundamentally thermoelastic and viscoplastic (i.e. rate-dependent) in nature.

In the final chapter two models are formulated for the thermoelastic, viscoplastic behavior of aluminum alloys and applied to the case of extrusion. The first model is based on a common semi-empirical form of the (scalar) flow rule in the extrusion community and neglects all effects of the microstructure on the hardening behavior. This results in an ideal viscoplastic model. The second model formulates a scalar flow rule as based on the Taylor assumption. Furthermore, the effect of the subgrain structure development on the inelastic free energy and the flow stress are considered. The predictions of both of these models for simple benchmark problems involving material testing and extrusion are compared.

The experimental results presented in this work are carried out by Institute of Forming Technology and Lightweight Construction (IUL) at TU Dortmund. The raw data of EBSD measurements of the extrusion samples are provided by Lehrstuhl für Werkstoffkunde (Materials Science) at University of Paderborn.

## Chapter 2

# Thermomechanical modeling and simulation of aluminum alloy behavior during extrusion and cooling\*

**Abstract** The purpose of this work is the modeling and simulation of aluminum alloys during extrusion processes. In particular, attention is focused here on aluminum alloys of the 6000 series (Al-Mg-Si) and 7000 series (Al-Zn-Mg). In the current paper, a number of aspects of the structural simulation as well as that of extrusion as a thermomechanical process are considered. These aspects include contact and adaptive mesh refinement, heat transfer inside the billet, heat transfer between the workpiece and the container, frictional dissipation, mechanical energy and surface radiation. The friction is considered to model the so called “dead material zone”. The radiation constant has been estimated so that the results are close to the experimental results.

### 2.1 Introduction

Extrusion as a technological process is used to produce profiles with constant cross sections from materials such as aluminum, copper, stainless steel and various types of plastic. The advantages of aluminum and its alloys include high ductility (due to its fcc crystal structure), making it particularly suitable for complex extrusion processes. Additionally, the ideal ratio of Young’s modulus to mass density in aluminum makes it suitable for a wide range of application in automotive and aircraft manufacturing, as well as for lightweight construction in general. The process of extrusion in combination with heat treatment and further processing, e.g. bending, leads to a complex microstructure development in the material. An understanding of this development in each processing step especially during extrusion and heat treatment allows one to influence and control the resulting material properties.

Simulation of hot forming processes by application of the finite element method (FEM) has been the subject of many recent works. Large plastic deformations and high temperature of the extrusion process cause developments in the microstructure of the material. Shercliff and Lovatt (1999) have presented various physical and statistical approaches for the modeling of microstructure evolution in hot deformation. In physically based state variable models, the microstructure and property evolution are modeled explicitly. In statistical approach the process conditions are linked empirically to the final microstructure. Furu et al. (1996) have offered a physically based model to describe the development of microstructure during hot forming processes which was later developed further by Sellars and Zhu (2000) by applying the concept

---

\*Results partly published in Parvizian et al. (2009)

of free energy as the driving force of microstructure evolutions. Microstructure developments are temperature dependent processes, therefore for modeling these developments it is required to consider a coupled thermomechanical model. Several constitutive laws have been used by different research groups. Duan and Sheppard (2004) have investigated the influence of the constitutive equation on the simulation of a hot rolling process. Duan and Sheppard (2003) have applied the isotropic viscoplastic Norton-Hoff law as the flow rule. Nes (1995) has used the hyperbolic sine law as the governing constitutive equation which is a purely empirical model suggested for metal forming processes such as hot rolling, forging and extrusion. This model is also employed by Sheppard (2006) for prediction of structure during extrusion process and also by Zhang et al. (2007) for material behavior of some new aluminum alloys in hot forming processes. In another work Bontcheva et al. (2006) have applied the ‘‘Shvarzbart’’ model for large deformations to describe the thermomechanical behavior of the material.

In the current work, attention is focused on certain aspects of the numerical simulation of extrusion and cooling including (1) contact and friction conditions, (2) adaptive mesh refinement, (3) thermomechanical behavior of material during extrusion and (4) conductive, convective and surface radiation cooling. The current approach is based on a continuum thermodynamic model formulation for thermoelastic-thermoviscoplastic material behavior of metallic materials. Rather than on the more realistic model of Sellars and Zhu (2000), the current material model assumes for simplicity a Johnson-Cook-like approach for the evolution of the accumulated equivalent inelastic deformation as a function of the stress, accumulated inelastic deformation and temperature.

## 2.2 Material model

Although not the principle focus of the current work, we outline the formulation of the material model used in this work in this section for completeness. The same general approach sketched below is also that used for much more detailed material modeling in work in progress building on that of Sellars and Zhu (2000).

The current approach is based on a large-deformation thermoelastic, thermoviscoplastic description of aluminum alloys at high temperature. In this context, local inelastic deformation is represented by a deformation-like quantity  $\mathbf{F}_P$ . This induces the part

$$\mathbf{F}_E = \mathbf{F} \mathbf{F}_P^{-1} \quad (2.1)$$

of the deformation gradient  $\mathbf{F}$  interpreted to be elastic in this context and a measure of energy storage in the material. The free energy density depends on the temperature  $\theta$ , local elastic deformation  $\mathbf{F}_E$  and internal state variables  $\epsilon_1, \dots$

$$\psi = \psi(\theta, \mathbf{F}_E, \epsilon_1, \dots). \quad (2.2)$$

This in turn determines the Kirchhoff stress

$$\mathbf{K} = \mathbf{P} \mathbf{F}^T = (\partial_{\mathbf{F}_E} \psi) \mathbf{F}_E^T \quad (2.3)$$

and the flow rule

$$\dot{\mathbf{F}}_P = \dot{\alpha}_P \mathbf{N}_{P_i} \mathbf{F}_P. \quad (2.4)$$

Here,  $\alpha_P$  is the accumulated inelastic deformation and  $\mathbf{N}_{P_i}$  is the flow direction. The evolution of internal variables  $\epsilon_1, \dots$  takes an analogous form

$$\dot{\epsilon}_i = \dot{\alpha}_P \pi_i \quad (2.5)$$

depending on  $\alpha_P$ . In more advanced models such as Sellars and Zhu (2000),  $\epsilon_1, \dots$  represent such quantities as the subgrain size, grain misorientation and dislocation density.

Next, attention is restricted to isotropic material behavior. In addition, the simplifying assumption of constant heat capacity is made here. Assuming then that the free energy density can be split into a sum of elastic and inelastic parts, one obtains

$$\psi = \psi_E(\theta, \ln \mathbf{V}_E) + \psi_P(\theta, \epsilon_1, \dots), \quad (2.6)$$

where  $\ln \mathbf{V}_E$  is the elastic left logarithmic stretch tensor following from the polar decomposition of  $\mathbf{F}_E = \mathbf{V}_E \mathbf{R}_E = \mathbf{R}_E \mathbf{U}_E$ . Here,

$$\begin{aligned} \psi_E(\theta, \ln \mathbf{V}_E) &= \varepsilon_{E0}(\ln \mathbf{V}_E) - \theta \eta_{E0}(\ln \mathbf{V}_E) \\ &\quad + \rho c_0 \{ \theta - \theta_0 - \theta \ln(\theta/\theta_0) \} \end{aligned} \quad (2.7)$$

represents the elastic part of this energy,  $\rho$  is the density of the material and  $c_0$  is the specific heat capacity of the material. The elastic part of energy consists of internal energetic

$$\begin{aligned} \varepsilon_{E0}(\ln \mathbf{V}_E) &= \kappa_0 \text{tr}(\ln \mathbf{V}_E)^2 / 2 + 3\kappa_0 \alpha_0 \theta_0 \text{tr}(\ln \mathbf{V}_E) \\ &\quad + \mu_0 \text{mag}(\text{dev}(\ln \mathbf{V}_E))^2 \end{aligned} \quad (2.8)$$

and configurational entropic

$$\eta_{E0}(\ln \mathbf{V}_E) = 3\kappa_0 \alpha_0 \mathbf{I} \cdot \ln \mathbf{V}_E \quad (2.9)$$

parts. Here  $\text{mag}(\mathbf{A}) = \sqrt{\mathbf{A} \cdot \mathbf{A}}$ ,  $\kappa_0$  is the bulk modulus of the material and  $\mu_0$  and  $\alpha_0$  represent the shear modulus and thermal expansion coefficient of the material, respectively. Likewise, the inelastic free energy density is given by

$$\psi_P = \varepsilon_{P0}(\epsilon_1, \dots) - \theta \eta_{P0}(\epsilon_1, \dots) \quad (2.10)$$

as a linear function of the temperature  $\theta$  and internal state variables  $\epsilon_i, \dots$ . From (2.7), the isotropic Kirchhoff stress takes the form

$$\begin{aligned} \mathbf{K} &= \partial_{\ln \mathbf{V}_E} \psi_E \\ &= \kappa_0 \{ \text{tr}(\ln \mathbf{V}_E) - 3\alpha_0(\theta - \theta_0) \} \mathbf{I} \\ &\quad + 2\mu_0 \text{dev}(\ln \mathbf{V}_E). \end{aligned} \quad (2.11)$$

On the basis of assuming Fourier heat conduction

$$\mathbf{q} = -k_0 \nabla \theta, \quad (2.12)$$

temperature changes due to elastic and inelastic heating can be found from

$$\rho c_0 \dot{\theta} = -3\kappa_0 \alpha_0 \theta \overline{\dot{\ln}(\det(\mathbf{F}))} + \beta \sigma \dot{\alpha}_P + k_0 \nabla^2 \theta, \quad (2.13)$$

where  $k_0$  is the material conductivity and  $\sigma$  the effective stress given by the von Mises stress

$$\sigma = \sqrt{\frac{3}{2}} |\text{dev}(\mathbf{K})|. \quad (2.14)$$

In addition,

$$\beta \equiv 1 - \sigma^{-1} \underbrace{\sum_i (\partial_{\epsilon_i} \varepsilon_{P0}) \pi_i}_{\text{"cold work"}} \quad (2.15)$$

represents the Taylor-Quinney factor. The current flow direction is determined by

$$\mathbf{F}_E \mathbf{N}_{P_i} \mathbf{F}_E^{-1} \equiv \partial_{\mathbf{K}} \sigma. \quad (2.16)$$

In turn, this results in the isotropic flow rule

$$-\ln \dot{\mathbf{V}}_E^* \equiv \ln(\mathbf{F} \dot{\mathbf{C}}_P^{-1} \mathbf{F}^T)/2 = \dot{\alpha}_P (\partial_{\mathbf{K}} \sigma_{vM}). \quad (2.17)$$

Finally, the Johnson-Cook model is introduced via the implicit evolution relation

$$\sigma = \partial_{\dot{\alpha}_P} \chi \quad (2.18)$$

for  $\dot{\alpha}_P$  in terms of the dissipation potential

$$\chi = \sigma_{jc} \dot{\alpha}_0 \left\{ (1 - C_0) \frac{\dot{\alpha}_P}{\dot{\alpha}_{P0}} + C_0 \left( 1 + \frac{\dot{\alpha}_P}{\dot{\alpha}_{P0}} \right) \ln \left( 1 + \frac{\dot{\alpha}_P}{\dot{\alpha}_{P0}} \right) \right\} \quad (2.19)$$

compatible with the Johnson-Cook model in terms of the corresponding material parameters  $\dot{\alpha}_{P0}$ ,  $A_0$ ,  $B_0$ ,  $n_0$ ,  $m_0$ ,  $\theta_M$  and  $C_0$  at the reference temperature  $\theta_0$ . In this case,

$$\sigma_{jc} = (A_0 + B_0 \dot{\alpha}_P^{n_0}) \left\{ 1 - \left( \frac{\theta - \theta_0}{\theta_M - \theta_0} \right)^{m_0} \right\}. \quad (2.20)$$

Indeed, we then have

$$\sigma = \sigma_{jc} \left\{ 1 + C_0 \ln \left( 1 + \frac{\dot{\alpha}_P}{\dot{\alpha}_{P0}} \right) \right\} \quad (2.21)$$

$A_0$  represents the initial flow stress of the material,  $\dot{\alpha}_{P0}$  is the initial plastic strain rate and  $\theta_M$  is the melting point of the material.

## 2.3 Numerical simulation

A robust and effective finite element simulation of the extrusion process requires special consideration of numerical aspects such as contact and element distortion. A general schematic view of the finite element model used in the current work is shown in Figure 2.1. Due to large deformations occurring during the process of extrusion, elements will be extremely distorted especially in the area where material flows through the die. The distorted elements will cause inaccurate results or termination of the simulation.

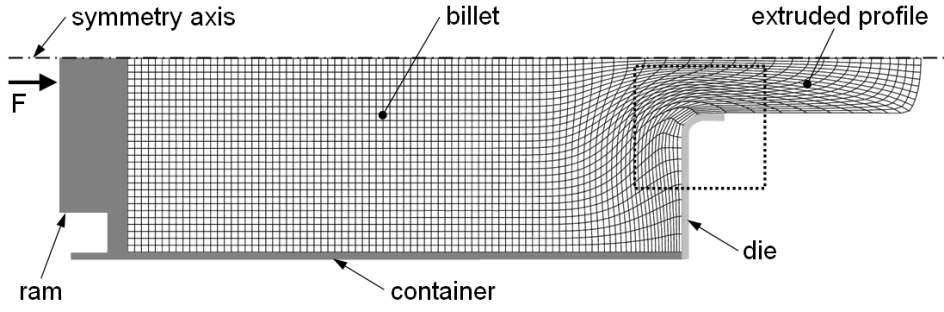


Figure 2.1: Finite element model of extrusion.

### 2.3.1 Contact

The contact between billet and die is modeled as a pure master-slave contact pair with hard surface behavior which represents the real contact condition. In this case no penetration of the slave nodes in the master surface is allowed. Due to negligible deformation of the die during the simulation, we are allowed to model the die as a rigid body. Problems occur when using a coarsely discretized billet surface (slave surface). Here, a penetration of the die surface (master surface) into the element surface (slave surface) may occur and would be unphysical. This mainly takes place where the material flows through the die (the dashed square region shown in Figure 2.1). Here the curved surface of the die has penetrated into the elements which are in contact with the die. As can be seen in Figure 2.2(a), the nodes of the contacted element are lying on the surface of the die, but the die has penetrated the edge of the element. This can be avoided and a much better contact simulation can be achieved with mesh refinement as shown in Figure 2.2(b).

The thermal contact between the billet and the container walls is formulated by

$$q = k(\theta_A - \theta_B), \quad (2.22)$$

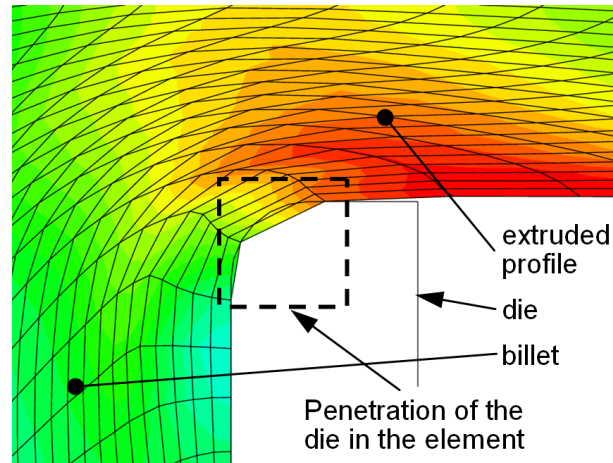
where  $q$  is the heat flux per unit area crossing the interface from point A on one surface to point B on the other surface,  $\theta_A$  and  $\theta_B$  are the temperatures of points A and B on the interacting surfaces and  $k$  is the gap conductance between the surfaces.

The frictional behavior of interacting surfaces can be modeled by applying *cohesive* or *adhesive* friction. In cohesive friction the sliding stresses depend on the yield stress of the workpiece, and the sliding actually occurs in a small boundary layer in the workpiece. In adhesive friction, the sliding stresses are proportional to the contact stress. In this case, sliding occurs between the die and the workpiece. The adhesive friction which is used in this work is modeled by using the standard Coulomb friction model in Abaqus. In this model it is assumed that no relative motion will occur unless the equivalent shear stress  $\tau_e$  is higher than the critical friction stress  $\tau_c = \mu P$ , where  $\mu$  and  $P$  are the friction coefficient and contact pressure, respectively.

### 2.3.2 Adaptive meshing

To avoid extreme element distortion and the penetration of the die surface in the extrusion elements, a well refined mesh with small edges can be used. To have less numeric costs, the

a)



b)

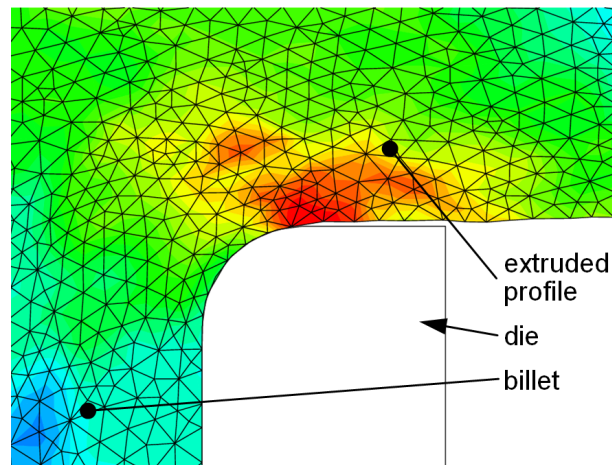


Figure 2.2: a) Penetration of the workpiece into the die without mesh refinement. b) Accurate contact between the die and the workpiece achieved with mesh refinement.

mesh should be refined locally only where it is required. Abaqus offers the ALE (Arbitrary Lagrangian Eulerian) method for adaptive meshing. In this method the mesh moves independently of the material without changing the element topology of the mesh (Gosh, 1990). ALE adaptive meshing can control the mesh distortion problem but it uses only a single mesh which will be smoothed within analysis steps. Therefore ALE is useful only when a single mesh can be used efficiently for the duration of the process. In the current work, a system (shown in Figure 2.3) based on the scripting language Python is developed to combine a mesh generator software and Abaqus as an FE-solver. In this system, an initial mesh is created for the first step of the simulation as shown in Figure 2.4. As explained before, the mesh should be refined when it is flowing through the die. To have a smooth change in mesh size, some refinement boundaries are defined. After fixed time steps, the Python code will call the mesh generator software to refine the elements which passed these defined geometric boundaries. In the example shown in Figure 2.4 the elements are refined in four different levels before flowing through the die. The



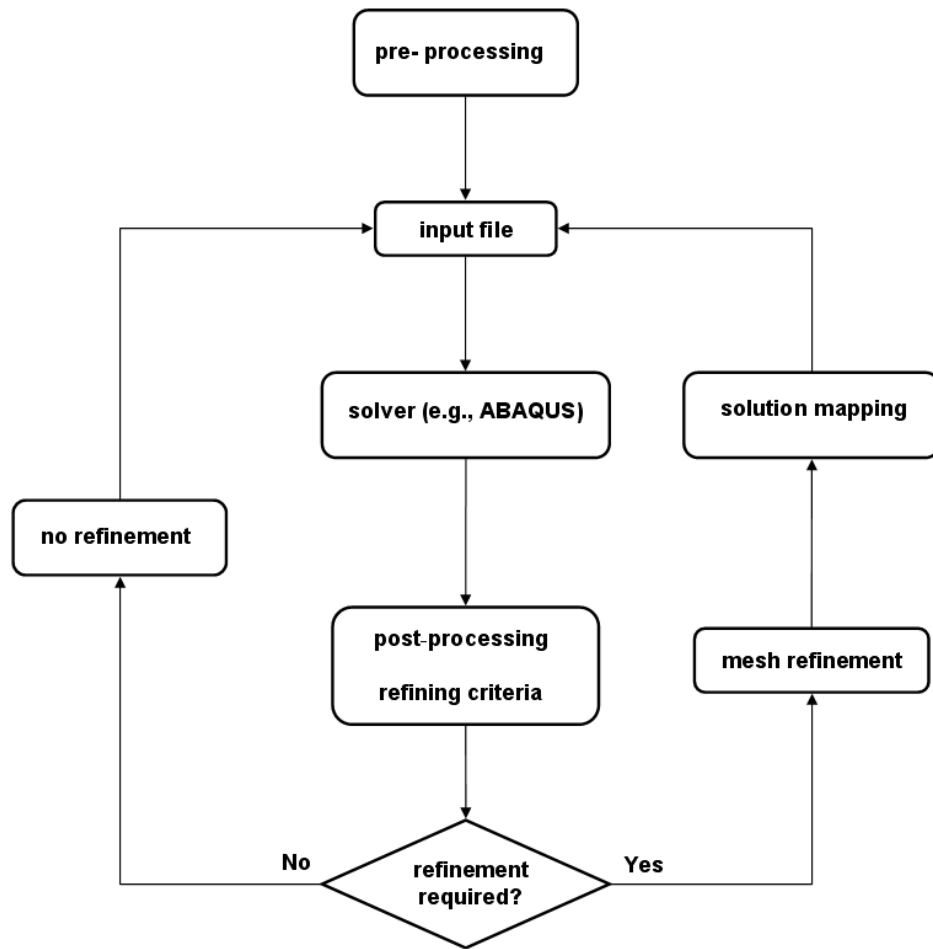


Figure 2.3: The Python-based system for mesh refinement and adaptivity developed in combination with FE-solver Abaqus.

adaptive mesh produced with this system controls the excessive mesh distortion and, as shown in Figure 2.2(b), no penetration happens in the contact between the elements and the die. After generating a new mesh, it is required to map the solution to the new mesh. This data transfer to the new mesh is carried out by the help of Python.

### 2.3.3 Cooling process

To simulate the cooling process after the extrusion, it is first required to cut the extruded part from the billet. This is done by help of Python scripting. Cooling is simulated as an uncoupled heat transfer process while considering convection and surface radiation. The surface heat flux due to radiation is modeled by:

$$q = A[(\theta - \theta_Z)^4 - (\theta_0 - \theta_Z)^4] \quad (2.23)$$

where  $q$  is the surface heat flux,  $A$  is the radiation constant which is dependent on Stefan-Boltzmann constant and the emissivity of the surface,  $\theta$  is the surface temperature,  $\theta_0$  is the ambient temperature and  $\theta_Z$  is the value of absolute zero on the applied temperature scale.

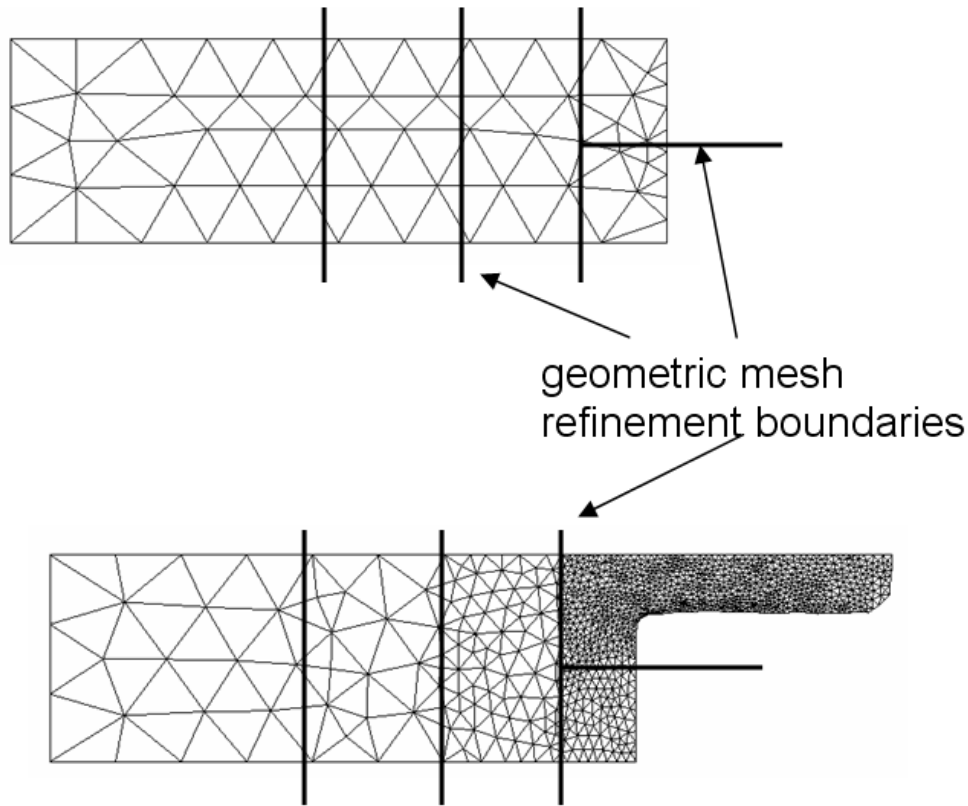


Figure 2.4: Initial mesh for the adaptive approach (top) and geometric mesh refinement procedure (bottom).

## 2.4 Results

The extrusion simulation in the current work is carried out as a coupled temperature-displacement process in Abaqus. The element type CPE3T, a 3-node plane strain thermally coupled triangle with linear displacement and temperature, is used. The initial temperature of the billet is 723 K. Several thermal and thermomechanical phenomena influence the extrusion process. The values of all the material parameters of EN AW-6060 for the Johnson-Cook model are given in Table 2.1. It is assumed that the flow stress depends only on the temperature  $\theta$  and the strain rate  $\dot{\alpha}_P$ , therefore  $B_0$  and  $n_0$  are both zero. The value of other material parameters are as follows: shear modulus  $\mu_0 = 26$  GPa, density  $\rho = 2700$  kg/m<sup>3</sup>, conductivity  $k = 237$  W/(m · K), thermal expansion coefficient  $\alpha = 2.34 \cdot 10^{-6}$  1/K, Poisson ratio  $\nu = 0.35$  and specific heat  $c_0 = 900$  J/(kg · K).

Mechanical dissipation acts as a heat source and results in an increase of temperature in the workpiece. It is common to assume that 90% of this dissipation is transformed into heat. This corresponds to a value of the Taylor-Quinney parameter  $\beta$  of 0.9. Another source of heating is the dissipation of friction sliding energy between the workpiece and the container. The whole

Table 2.1: Material parameters of EN AW-6060 for Johnson-Cook model.

Parameter	Value
$A_0$	48.98 MPa
$B_0$	0.0
$n_0$	0.0
$m_0$	2.06861
$\theta_0$	693.0 K
$\theta_M$	933.0 K
$C_0$	0.069693
$\dot{\alpha}_{P0}$	$0.1077771 \text{ s}^{-1}$

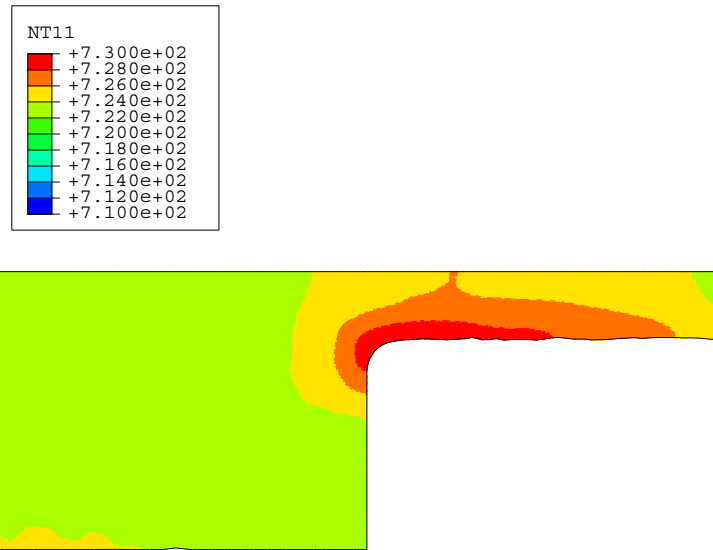
of this energy is assumed to be converted to heat energy. The heat generated due to friction is equally divided between the billet and the container. The friction coefficient  $\mu$  for the Coulomb friction model has the value of 0.4.

The temperature difference between the die and the billet leads to heat conduction across their surface of contact. Having a higher temperature than the container (623 K), the workpiece will cool down during the contact with the container.

Figure 2.5 shows the effect of heat conduction between the billet and the container on the temperature distribution of the billet. In absence of conduction, the temperature will increase in the workpiece due to mechanical dissipation in the bulk and friction between billet and container. As it can be seen in Figure 2.5(b), by applying contact conduction due to the temperature difference of the billet and the die, the temperature decreases in the outer surface of the workpiece, but at the same time it increases where material flows through the die. As shown in Figure 2.6 this region has the highest value of equivalent plastic strain and therefore more inelastic energy is dissipated to heat. The increase of temperature in the area close to the container's wall resulting from dissipation of friction energy can be seen in Figure 2.5(a).

Schikorra et al. (2007b) have investigated the influence of friction between the billet and the container on the material flow through the die. As shown by Schikorra et al. (2007a,e) friction between the billet and container results in a region of little or no deformation known as the dead material zone. To correctly model the formation of this zone, information is required on the friction properties of the interface between the billet and the container. In addition, modeling this dead zone is only possible by applying an adaptive mesh method which enables us to change the topology of the mesh. Because of very small deformations of the material in the dead zone, no element distortion arises in this area and therefore no new mesh is generated for this zone during the adaptive mesh refining, whereas the mesh topology will change for the rest of the workpiece. Figure 2.7 shows the effect of applying friction on displacement of the material in the last step of the simulation. In Figure 2.7(a) no friction is applied between the contact surfaces and, as can be seen, no dead material zone is created, whereas by applying friction, the forming of the dead material zone is visible in Figure 2.7(b) which is in acceptable agreement with experimental results of Schikorra et al. (2007a).

a)



b)

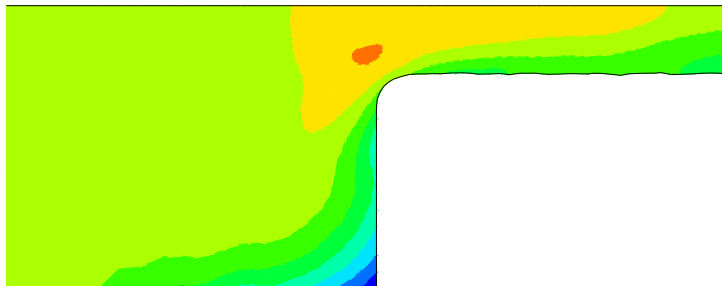
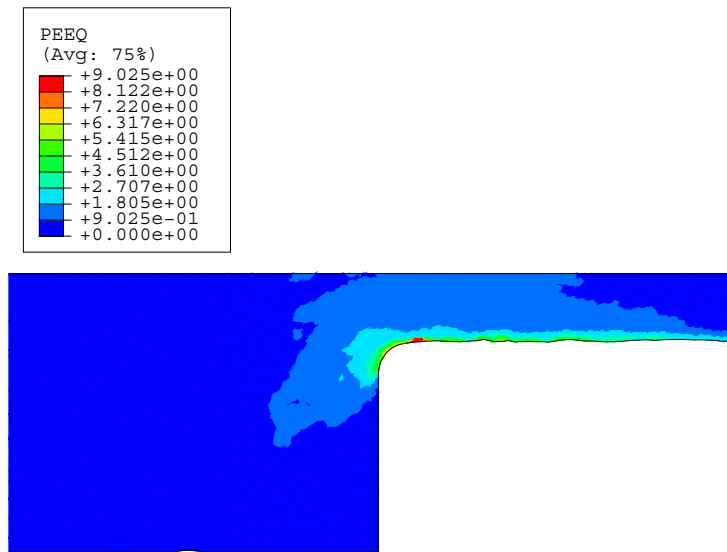


Figure 2.5: Effect of contact heat conduction between the billet and the container on temperature (K) distribution of the workpiece a) without contact conduction, b) with contact conduction.

Applying room temperature as an artificial boundary condition for the simulation of the cooling process with considering heat conduction inside the profile results in quick decrease of temperature down to the room temperature in about 1 second. To have a realistic heat transfer simulation, it is necessary to model the heat convection as well as the surface radiation. To avoid the complexity of the simulation, the convection effect can be simulated with modifying heat radiation parameters. Here the radiation constant  $A$  in (2.23) has the numerical value of  $5.67 \times 10^{-4} \text{W/m}^2 \cdot \text{C}^4$ . With this estimation we reach the cooling time of about 900 seconds which coincides with the experimental results.

The temperature distribution of the extruded part before and after the cooling process is shown in Figure 2.8. At the beginning of the process the middle part of the profile has a higher temperature. As explained before, the conduction between the billet and the die causes a lower temperature on the outer surface of the extruded profile. Because of the short time of the extru-

a)



b)

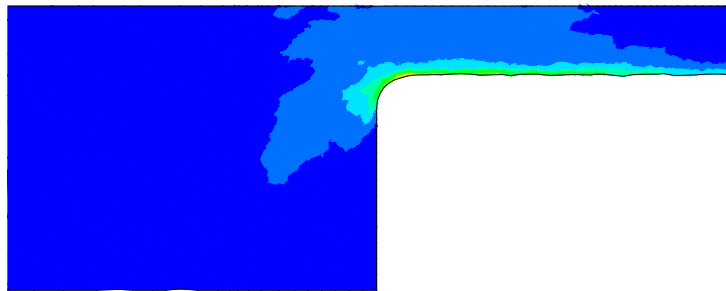
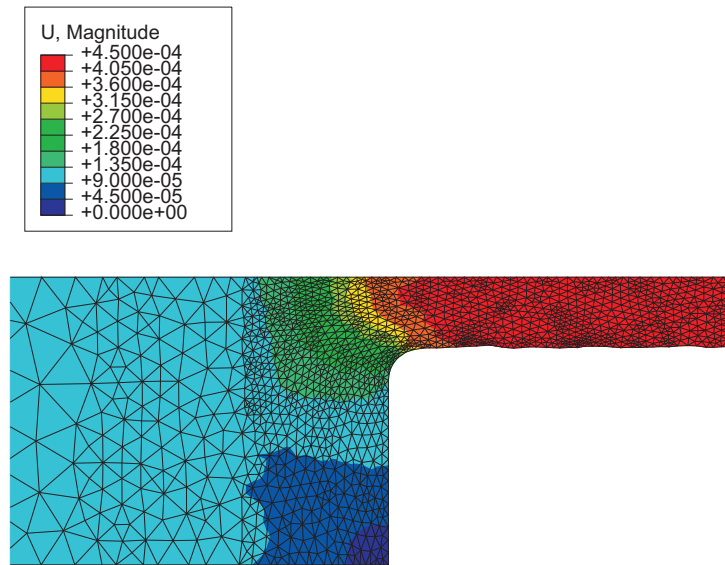


Figure 2.6: Equivalent plastic strain of the workpiece: a) without contact conduction, b) with applying contact conduction.

sion process (6 seconds) compared to cooling process (900 seconds), the cooling of the profile during the extrusion is not included in the cooling process. Figure 2.8(b) shows the profile after 450 seconds of cooling. In Figure 2.8(c) the temperature distribution of the profile after 900 seconds cooling is shown.

As it can be seen in Figure 2.8(a), the temperature distribution before the cooling process is heterogeneous and the material which firstly flows has a higher temperature. This can be explained as a result of heat transfer between the billet and the die. The material which comes out first has less contact with the container walls with lower temperature. Therefore this part of the extruded profile has a higher temperature. The heat transfer inside the material takes place much faster than the surface radiation. This results in a homogeneous temperature distribution inside the extruded profile during the cooling process. The temperature drop in the first half of the cooling time is much higher than in the second half and the profile cools down almost to the room temperature in the first 450 seconds. This difference is due to the dependency of surface

a)



b)

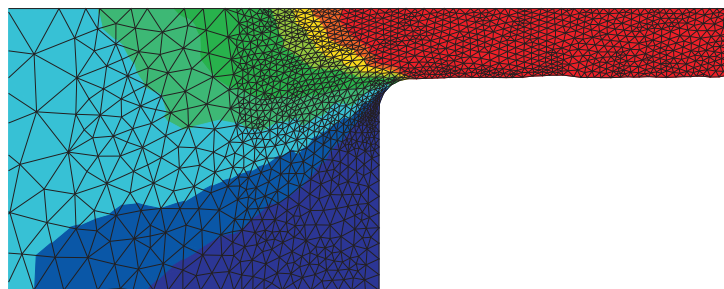


Figure 2.7: Displacement of material during extrusion simulation: a) without friction, b) with friction.

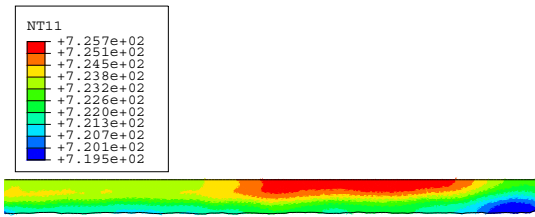
radiation to the fourth power of temperature. When the temperature difference between the extruded profile and the room temperature decreases, the cooling process quickly slows down.

## 2.5 Summary and conclusions

In this work the thermomechanical behavior of aluminum alloys during the extrusion process was investigated. The necessity of using the adaptive remeshing method to overcome element distortion and ensure proper contact modeling was shown. In addition, modeling of material flow and formation of the dead material zone also require the use of adaptive methods.

Moreover, the influence of the friction, heat flux between the contacted surfaces and dissipated inelastic energy on the thermomechanical behavior of the workpiece during the simulation process was shown. Friction is crucial for the formation of the “dead material zone” and also

a)



b)



c)



Figure 2.8: Temperature distribution (K) in the extruded profile: a) before cooling process, b) after 450 seconds of cooling, c) after 900 seconds of cooling. The legend in c) is the same as in b).

causes the increase of temperature in the billet due to dissipated frictional energy. Another source of heating is the dissipated inelastic energy which also increases the temperature of the billet especially in the areas with high plastic deformations, whereas the heat flux between the contacted surfaces of the billet and the container cools down the billet. In the final step, the cooling process was simulated considering heat radiation and convection. To avoid the complexity of the simulation, the effect of convection was simulated by modifying the surface radiation constants.

To model the extrusion process, a material model is required to describe the material behavior which is controlled by various microstructural processes. In the current case, these are predominantly recovery and subgrain evolution. Apart from a high ductility due to its fcc crystal structure, aluminum has a relatively high stacking fault energy. Because of this, recovery and subgrain evolution are favored over recrystallization at high temperature during the extrusion process. Such processes are accounted for in the approach in the work of Sellars and Zhu (2000) and more recent models and are discussed in detail in the following chapters of this thesis.





## Chapter 3

# Thermomechanically coupled modeling and simulation of hot metal forming processes using the adaptive remeshing method\*

**Abstract** The purpose of this work is to model and simulate hot metal forming processes in which material undergoes large deformations with the help of the Finite Element (FE) software Abaqus using the Lagrangian formulation. Extrusion of aluminum alloys and forging of steels as two examples are taken into account in this work. To this end, a material model based on thermoelastic viscoplasticity is formulated for each case. The microstructural evolution is modeled effectively with the help of internal state variables. Element distortion and contact during the simulation of large deformation processes is controlled with the help of a custom adaptive remeshing system based on Python scripting and utilizable in commercial programs such as Abaqus. Simulation results for the microstructural development during extrusion as a function of process conditions demonstrate the sensitivity of microstructure development to these conditions. Comparison of the simulation results for the microstructure evolution with corresponding experimental results show good qualitative agreement.

### 3.1 Introduction

Modeling and simulation of large deformation processes have been the subject of many researches in recent years. Thermomechanical modeling of the forming process requires a reliable numeric approach on the one hand and an appropriate material model on the other. The Lagrangian approach, the Eulerian approach, Arbitrary Lagrangian Eulerian (ALE) and meshless methods have been applied by different groups. Guo and Nakanishi (2003) have applied the rigid-plastic integralless–meshless method to the analysis of plane strain backward extrusion. In the works of Coupez et al. (1998) and Parvizian et al. (2009) adaptive refinement algorithms based on the Lagrangian approach are presented for the simulation of large forming processes. Gautham et al. (2003) proposed a background mesh with advancing front based mesh generation for the 2D simulation of the metal forming processes. Lou et al. (2008) have applied the Finite Volume Method to overcome the element distortion and contact problems occurring during the simulation of the extrusion process. Williams et al. (2002) have also applied finite volume methods on the unstructured mesh in simulation of forging and extrusion. The Eulerian approach has generally been used for the simulation of the steady state metal forming with the assumption that the die is entirely rigid which is not usually realistic (Williams et al., 2002).

---

\*Results partly published in Parvizian et al. (2010)

Applying some remeshing or mesh refinement techniques is unavoidable when the Lagrangian approach is used for the simulation. In this work a remeshing scheme of the deformed geometry is presented. This method is applied for two examples of metal forming: extrusion of aluminum and forging of steel.

An accurate numeric simulation of these two processes requires appropriate material models. The material modeling in this work is based on the isotropic thermoelastic viscoplastic approach. The corresponding model for each case in combination with the numerical implementation and the necessary modifications of the model in order to use with the remeshing system are represented in the following sections. These models are implemented as user material (UMAT) in the commercial FEM software Abaqus.

## 3.2 Material modeling

### 3.2.1 Single-phase deformation behavior

The purpose of this section is to establish the continuum thermodynamic framework for the formulation of material models for single- or multiphase thermoelastic, viscoplastic behavior. For simplicity, we assume that the material behavior of each phase is isotropic. More generally, non-trivial distributions of grain orientation (i.e. texture), grain size, and grain shape, will result in anisotropic behavior. In the current work, however, this is neglected. In addition, for simplicity, attention is restricted here to the case of two (metallic) solid phases. For example, in the case of steels, these could be austenite and martensite. In the case of aluminum alloys, these could be (aluminum) matrix and precipitate. In the current thermoelastic, viscoplastic context, the deformation behavior of a given phase is determined by the constitutive form of the free energy density  $\psi$  and the dissipation potential  $\chi$ . Rather than  $\chi$ , one can alternatively work with the inelastic potential  $\phi$ , i.e. its thermodynamic conjugate. For simplicity, we assume that the temperature field  $\theta$ , the deformation gradient  $\mathbf{F} = \nabla_{\mathbf{r}}\chi$ , and the referential temperature gradient  $\mathbf{g}_r = \nabla_r\theta$  are the same in all phases. Here,  $\chi$  represents the deformation field and  $\nabla_r$  the gradient operator with respect to the reference (e.g. initial) configuration of the material. The inelastic state of each phase is characterized by a local inelastic deformation  $\mathbf{F}_P$  and the accumulated equivalent inelastic strain  $\alpha_P$ . Modeling  $\mathbf{F}_P$  as a change of local reference configuration (Svendsen, 2001), and assuming that the evolution of  $\alpha_P$  results in energy storage in the material, the free energy of each phase is modeled by the additive split

$$\psi(\theta, \ln \mathbf{V}_E, \alpha_P) = \psi_E(\theta, \ln \mathbf{V}_E) + \psi_P(\theta, \alpha_P) \quad (3.1)$$

into elastic  $\psi_E$  and inelastic  $\psi_P$  parts, again in the case of isotropic behavior. Here,  $\ln \mathbf{V}_E := \frac{1}{2} \ln(\mathbf{B}_E)$  is the elastic left logarithmic stretch tensor,  $\mathbf{B}_E = \mathbf{F}_E \mathbf{F}_E^T = \mathbf{F} \mathbf{C}_P^{-1} \mathbf{F}^T$  represents the elastic left Cauchy-Green deformation,  $\mathbf{F}_E := \mathbf{F} \mathbf{F}_P^{-1}$  is the elastic part of  $\mathbf{F}$ , and  $\mathbf{C}_P = \mathbf{F}_P^T \mathbf{F}_P$  represents the inelastic right Cauchy-Green deformation. In the current isotropic case,  $\psi_E(\theta, \ln \mathbf{V}_E)$  is an isotropic function of  $\ln \mathbf{V}_E$ . In addition to isotropy, we exploit the fact that the magnitude  $\text{mag}(\ln \mathbf{V}_E) := \sqrt{\ln \mathbf{V}_E \cdot \ln \mathbf{V}_E}$  of  $\ln \mathbf{V}_E$  remains small in the case of metals. This results in the form

$$\begin{aligned} \psi_E(\theta, \ln \mathbf{V}_E) &= \psi_E(\theta, \mathbf{0}) + \zeta_E(\theta) \text{tr}(\ln \mathbf{V}_E) \\ &+ \frac{1}{2} \kappa_E(\theta) \text{tr}(\ln \mathbf{V}_E)^2 + \mu_E(\theta) \text{mag}(\text{dev}(\ln \mathbf{V}_E))^2 \end{aligned} \quad (3.2)$$

to second-order in terms of the thermal expansion modulus  $\zeta_E(\theta)$ , the bulk modulus  $\kappa_E(\theta)$  and the shear modulus  $\mu_E(\theta)$ . Here,  $\text{dev}(\ln \mathbf{V}_E) := \ln \mathbf{V}_E - \frac{1}{3} \text{tr}(\ln \mathbf{V}_E) \mathbf{I}$  is the deviatoric part of  $\ln \mathbf{V}_E$ . In particular, (3.2) implies the form

$$\begin{aligned} \mathbf{K}(\theta, \ln \mathbf{V}_E) &= \partial_{\ln \mathbf{V}_E} \psi(\theta, \ln \mathbf{V}_E, \alpha_P) \\ &= \{\zeta_E(\theta) + \kappa_E(\theta) \text{tr}(\ln \mathbf{V}_E)\} \mathbf{I} + 2 \mu_E(\theta) \text{dev}(\ln \mathbf{V}_E) \end{aligned} \quad (3.3)$$

for the Kirchhoff stress. Assume that there exists a reference temperature  $\theta = \theta_0$  at which the material is stress-free, i.e.  $\mathbf{K}(\theta_0, \mathbf{0}) = \mathbf{0}$ . In this case,  $\zeta_E(\theta_0) = 0$  must hold. This results in the form  $\zeta_E(\theta) = 3 \kappa_E(\theta) \alpha_0 (\theta_0 - \theta)$  of  $\zeta_E(\theta)$  for  $\zeta_E(\theta)$  in terms of the coefficient of thermal expansion  $\alpha_0$ . Assuming that  $\kappa_E(\theta)$  and  $\mu_E(\theta)$  are at most linear functions of temperature, the heat capacity

$$\begin{aligned} c_E(\theta, \ln \mathbf{V}_E) &= -\theta \partial_\theta \partial_\theta \psi_E(\theta, \ln \mathbf{V}_E) \\ &= c_E(\theta, \mathbf{0}) - 3 \kappa_E'(\theta) \alpha_0 \theta \text{tr}(\ln \mathbf{V}_E) \\ &= c_0 \{\theta - \theta_0 - \theta \ln(\theta/\theta_0)\} - 3 \kappa_E'(\theta) \alpha_0 \theta \text{tr}(\ln \mathbf{V}_E) \end{aligned} \quad (3.4)$$

is independent of  $\mu_E(\theta)$ . Here,  $\psi_E(\theta, \mathbf{0}) = c_0 \{\theta - \theta_0 - \theta \ln(\theta/\theta_0)\}$  holds in terms of the heat capacity  $c_0$  at the reference temperature  $\theta_0$ . Since  $\text{mag}(\ln \mathbf{V}_E) \ll 1$ , the second term in (3.4) is assumed to remain small and is neglected in what follows. In this case, we work with the reduced form

$$\begin{aligned} \psi_E(\theta, l_H, l_D) &= \frac{1}{2} \kappa_E(\theta) l_H^2 + \mu_E(\theta) l_D^2 \\ &\quad + 3 \kappa_E(\theta) \alpha_0 (\theta_0 - \theta) l_H \\ &\quad + c_0 \{\theta - \theta_0 - \theta \ln(\theta/\theta_0)\} \end{aligned} \quad (3.5)$$

of (3.2), and so that

$$\psi(\theta, l_H, l_D, \alpha_P) = \psi_E(\theta, l_H, l_D) + \psi_P(\theta, \alpha_P) \quad (3.6)$$

of (3.1), in terms of the scalar elastic strain measures

$$\begin{aligned} l_H &:= \text{tr}(\ln \mathbf{V}_E), \\ l_D &:= \text{mag}(\text{dev}(\ln \mathbf{V}_E)), \end{aligned} \quad (3.7)$$

derived from  $\ln \mathbf{V}_E$ , such that  $\ln \mathbf{V}_E = \frac{1}{3} l_H \mathbf{I} + l_D \text{dir}(\text{dev}(\ln \mathbf{V}_E))$  holds. Here,  $\text{dir}(\mathbf{A}) := \mathbf{A}/\text{mag}(\mathbf{A})$  is the direction of any non-zero tensor  $\mathbf{A}$ . The relation (3.5) and these last results determine in particular the form

$$\mathbf{K} = \partial_{\ln \mathbf{V}_E} \psi = k_H \mathbf{I} + k_D \text{dir}(\text{dev}(\ln \mathbf{V}_E)) \quad (3.8)$$

of the Kirchhoff stress  $\mathbf{K}$ , with

$$\begin{aligned} k_H &:= \frac{1}{3} \text{tr}(\mathbf{K}) &= \partial_{l_H} \psi &= \kappa_E \{l_H + 3 \alpha_0 (\theta_0 - \theta)\}, \\ k_D &:= \text{mag}(\text{dev}(\mathbf{K})) &= \partial_{l_D} \psi &= 2 \mu_E l_D, \end{aligned} \quad (3.9)$$

its scalar hydrostatic and deviatoric parts, respectively. In the current model class, then,  $(k_H, l_H)$  and  $(k_D, l_D)$  are thermodynamic conjugates. Assuming quasi-static conditions, the deformation field  $\chi$  is determined as usual via the corresponding form

$$\text{div}_r(\mathbf{K} \mathbf{F}^{-T}) = \mathbf{0} \quad (3.10)$$

of the momentum balance. Analogously, in the current Clausius-Duhem context, the field relation

$$c_E \dot{\theta} = \omega - \operatorname{div}_r \mathbf{q}_r \quad (3.11)$$

for the temperature  $\theta$  is derived from the momentum, entropy and energy balances. In this relation,  $\omega$  represents the rate of heating, and

$$-\mathbf{q}_r/\theta = \partial_{\mathbf{g}_r} \chi_C \quad (3.12)$$

the referential heat flux. This is determined constitutively by the conduction part

$$\chi_C(\theta, \mathbf{F}, \mathbf{g}_r) = \frac{1}{2} \theta^{-1} k_0 \mathbf{F}^{-T} \mathbf{g}_r \cdot \det(\mathbf{F}) \mathbf{F}^{-T} \mathbf{g}_r \quad (3.13)$$

of the total dissipation potential. The form of  $\chi_C$  is based on Fourier heat conduction, with  $k_0$  being the coefficient of thermal conductivity. Neglecting any deformation-dependent damage and assuming inelastically incompressible von-Mises flow, the evolution of  $\ln \mathbf{V}_E$  is given by the (objective) associated flow rule

$$-\ln \mathbf{V}_E^* := \frac{1}{2} \ln(\mathbf{F} \overline{\mathbf{C}}_P^{-1} \mathbf{F}^T) = \dot{\alpha}_P \partial_{\mathbf{K}} \sigma_{vM} \quad (3.14)$$

in terms of the accumulated equivalent inelastic deformation  $\alpha_P$  and the von Mises equivalent stress

$$\sigma_{vM} = \sqrt{\frac{3}{2}} k_D = \sqrt{6} \mu_E l_D \quad (3.15)$$

determining the direction  $\partial_{\mathbf{K}} \sigma_{vM}$  of inelastic flow. The latter also determines the effective stress measure

$$\sigma_P := \mathbf{K} \cdot \partial_{\mathbf{K}} \sigma_{vM} - \partial_{\alpha_P} \psi = \sigma_{vM} - \partial_{\alpha_P} \psi_P \quad (3.16)$$

thermodynamically conjugate to  $\alpha_P$ . The single-phase model formulation is completed by specification of either form

$$\begin{aligned} \dot{\alpha}_P &= \partial_{\sigma_P} \phi_P, \\ \sigma_P &= \partial_{\dot{\alpha}_P} \chi_P, \end{aligned} \quad (3.17)$$

of the constitutive relation for the evolution of  $\alpha_P$  determined by  $\sigma_P$  via the inelastic stress potential  $\phi_P(\theta, \sigma_P, \dots)$  or the inelastic dissipation potential  $\chi_P(\theta, \dot{\alpha}_P, \dots)$ .

In summary, particular forms of the above single-phase model are obtained via specification of (i) the temperature-dependence of  $\kappa_E(\theta)$  and  $\mu_E(\theta)$  in (3.5), (ii) the form  $\psi_P(\theta, \alpha_P)$  of the inelastic part of  $\psi$  in (3.6), and (iii) the form of either  $\chi_P$  or  $\phi_P$ . On this basis, we now apply this approach to two specific cases: (i) high-temperature extrusion of aluminum alloys and (ii) thermomechanical loading of steels.

### 3.2.2 Extrusion of aluminum alloys

If the material (e.g. an aluminum alloy) under consideration is in a strain- and stress-free state at room temperature, it will not remain so after placing it in the extrusion device and heating it to 673 K. Indeed, the resulting thermal expansion of the material and a reduction in the elastic properties will affect the stress state in general. On the other hand, if given enough time before loading begins, local inelastic processes in the material will relax any significant local stress

build-up. On this basis, we make the modeling simplification  $\mathbf{K}(\theta = \theta_0, \mathbf{0}) = \mathbf{0}$  with  $\theta_0$  chosen to be the initial temperature of the extrusion process. During this process, the temperature varies, for example, due to mechanical dissipation, friction of the block with the walls of the extrusion device and heat conduction. Generally speaking, the former two result in a temperature increase, and the latter in a temperature decrease, near  $\theta_0$ . Assuming this temperature variation is not large,  $\kappa_E(\theta) \approx \kappa_0$  and  $\mu_E(\theta) \approx \mu_0$  in (3.5) can be assumed to be approximately constant. The high stacking-fault energy of materials like aluminum alloys implies that, at high homologous temperatures, dislocation-based dynamic recovery and cell-wall microstructure development leading subgrain formation are energetically favorable in comparison to kinetics-based dynamic recrystallization. As such, the activation and dynamics of inelastic flow in such materials is dislocation-based, motivating the semi-empirical activation form

$$\dot{\alpha}_P = \partial_{\sigma_P} \phi_P = \dot{\alpha}_0 e^{g_0/k\theta_0} e^{-g_0/k\theta} \sinh^{n_0} \left( \frac{\sigma_P - \sigma_{AP}}{\sigma_{DP}} \right) \quad (3.18)$$

of the (explicit) flow rule for  $\dot{\alpha}_P$  adapted from e.g. Sellars and Zhu (2000); Sheppard (2006). Here,  $\sigma_{AP}$  represents the initial activation stress for dislocation motion (i.e. initial yield stress),  $\sigma_{DP}$  is the drag stress on moving dislocations and  $n_0$  is the rate exponent. This can be inverted to obtain

$$\sigma_P = \partial_{\dot{\alpha}_P} \chi = \sigma_{AP} + \sigma_{DP} \sinh^{-1} \left( \frac{z^{1/n_0}}{z_0^{1/n_0}} \right) \quad (3.19)$$

for the implicit form of the flow rule in terms of the Zener-Hollomon parameter

$$z := \dot{\alpha}_P \exp(g_0/k\theta). \quad (3.20)$$

Formally, (3.18) and (3.19) can be integrated to yield the corresponding potential; for example, the latter is consistent with the form

$$\begin{aligned} \chi_P &= \sigma_{AP} \dot{\alpha}_P \\ &+ \sigma_{DP} \dot{\alpha}_P \sinh^{-1} \left( \frac{z^{1/n_0}}{z_0^{1/n_0}} \right) \\ &- \sigma_{DP} \dot{\alpha}_P \frac{1}{1+n_0} \frac{z^{1/n_0}}{z_0^{1/n_0}} {}_2F_1 \left( \frac{1}{2}, \frac{1+n_0}{2}; \frac{3+n_0}{2}; -\frac{z^{2/n_0}}{z_0^{2/n_0}} \right) \end{aligned} \quad (3.21)$$

for the inelastic dissipation potential in terms of the hypergeometric function  ${}_2F_1(a, b; c; z)$  of the second kind. For the purposes of the current work, we also neglect  $\psi_P(\theta, \alpha_P)$  for simplicity, something which is generally not a reasonable assumption. In this case,  $\sigma_P = \sigma_{VM}$  follows from (3.16), leading to an overestimate of  $\sigma_P$ . The evolution of  $\alpha_P$  drives that of the (immobile) dislocation density  $\rho$ , the misorientation  $\varphi$ , and the subgrain size  $\delta$ . To characterize the evolution of these, it is useful to scale each of them by their corresponding saturation values, yielding the (non-dimensional) quantities  $\epsilon_\rho := \sqrt{\rho}/\sqrt{\rho_{sat}}$ ,  $\epsilon_\varphi := \varphi/\varphi_{sat}$  and  $\epsilon_\delta := \delta/\delta_{sat}$ . In this context, the evolution of the first two is modeled via the experimentally-established Voce form

$$\begin{aligned} \dot{\epsilon}_\rho &= c_\rho (1 - \epsilon_\rho) \dot{\alpha}_P, \\ \dot{\epsilon}_\varphi &= c_\varphi (1 - \epsilon_\varphi) \dot{\alpha}_P, \end{aligned} \quad (3.22)$$

(e.g. Sellars, 1997; Sellars and Zhu, 2000; Zhu et al., 1997). According to these,  $\epsilon_{\rho,\varphi}$  vary between 0 and 1 at a rate determined by  $c_{\rho,\varphi}$ . On the other hand, the subgrain size is observed to decrease with increasing  $\dot{\alpha}_P$ . Consequently, its non-dimensional form  $\epsilon_\delta := \delta/\delta_{\text{sat}}$  is initially larger than 1 and decreases to this value with increasing  $\alpha_P$ . Indeed, its development is described by the experimentally-established Holt relation

$$\dot{\epsilon}_\delta = c_\delta \epsilon_\delta (1 - \epsilon_\delta) \dot{\alpha}_P \quad (3.23)$$

(e.g. Sellars and Zhu, 2000). On this basis,  $\epsilon_\delta$  decreases from its initial value  $\epsilon_\delta(0) > 1$  to 1 at a rate determined by  $c_\delta$ . Assuming no external supplies and the Taylor-Quinney approximation, we have

$$\begin{aligned} \omega &= \theta (\partial_\theta \mathbf{K}) \cdot \mathbf{D} + (\sigma_P - \theta \partial_\theta \sigma_P) \dot{\alpha}_P \\ &\approx \theta (\partial_\theta \mathbf{K}) \cdot \mathbf{D} + \beta_P \sigma_P \dot{\alpha}_P, \end{aligned} \quad (3.24)$$

again in the context of  $\text{mag}(\ln \mathbf{V}_E) \ll 1$ . Here,  $\beta_P$  represents the Taylor-Quinney coefficient. It has been shown for example in Rosakis et al. (2000) that  $\beta_P$  is in fact not a constant but rather depends on strain and strain-rate to varying degrees. Since no experimental data relevant to the determination of such dependence is available for the materials of interest here, however, we assume  $\beta_P$  is constant in this work.

For the simulations of aluminum alloy EN AW-6060, the thermoelastic and inelastic parameter values presented in Table 3.1 have been used.

$\kappa_0$	$\mu_0$	$\alpha_0$	$\theta_0$	$c_0$	$k_0$
70 GPa	20.5 GPa	$2.3 \times 10^{-5} / \text{K}$	673 K	$2.376 \times 10^6 \text{ J} / \text{m}^3 \text{ K s}$	$237 \text{ J} / \text{m K s}$
$g_0/k$	$n_0$	$z_0$	$\sigma_{AP}$	$\sigma_{DP}$	$\epsilon_\rho(0)$
$1.8 \times 10^4 \text{ K}$	4.27	$3.3 \times 10^8 / \text{s}$	0.0 MPa	62.5 MPa	$5 \times 10^{-3}$
$c_\rho$	$\epsilon_\varphi(0)$	$c_\varphi$	$\epsilon_\delta(0)$	$c_\delta$	$\beta_P$
1	0	1	67	1	0.9

Table 3.1: Thermoelastic and inelastic material parameters of the aluminum alloy EN AW-6060 used for simulation of extrusion process.

### 3.2.3 Thermomechanical loading of steels

The following is an adaptation of the model of Mahnken and Schneidt (2010) for steels transforming from austenite to martensite upon thermomechanical loading. This model is geared toward technological process simulation. To this end, it is assumed for simplicity that  $\theta$ ,  $\mathbf{F}$ ,  $\mathbf{g}_T$ ,  $\mathbf{F}_P$ , and  $\alpha_P$ , are the same in each phase. This results in the simple mixture model

$$\begin{aligned} \psi(\theta, l_H, l_D, \alpha_P, z) &= (1 - z) \psi_a(\theta, l_H, l_D) + z \psi_m(\theta, l_H, l_D) \\ &+ \psi_P(\theta, \alpha_P, z) + \psi_T(\theta, l_H, z) \\ &= \psi_E(\theta, l_H, l_D, z) + \psi_P(\theta, \alpha_P) + \psi_T(\theta, l_H, z) \end{aligned} \quad (3.25)$$

for the total free energy of the two-phase system in terms of the volume fraction  $z$  of martensite. The thermoelastic parts  $\psi_{E_{a,m}}(\theta, l_H, l_D)$  of austenite (subscript a) and martensite (subscript m) are given by (3.5). Consequently,

$$\begin{aligned} \psi_E(\theta, l_H, l_D, z) &= \frac{1}{2} \kappa_E(\theta) l_H^2 + \mu_E(\theta) l_D^2 \\ &+ 3 \kappa_E(\theta) \{(1 - z) \alpha_{a0} + z \alpha_{m0}\} (\theta_0 - \theta) l_H \\ &+ c_0 \{\theta - \theta_0 - \theta \ln(\theta/\theta_0)\} \end{aligned} \quad (3.26)$$

for the thermoelastic free energy density of the two-phase system. Attention is restricted here to the case that the transformation is from fcc-austenite to bcc-martensite, i.e. cubic symmetry in both cases. For simplicity, assume then that the bulk and shear modulus of the two phases are equal, i.e.

$$\begin{aligned}\kappa_E(\theta) &= \kappa_a(\theta) = \kappa_m(\theta) = \kappa_0 + \kappa_1(\theta - \theta_0), \\ \mu_E(\theta) &= \mu_a(\theta) = \mu_m(\theta) = \mu_0 + \mu_1(\theta - \theta_0).\end{aligned}\quad (3.27)$$

Likewise, we assume  $c_0 = c_{a0} = c_{m0}$ . On the other hand, the change in unit cell volume upon transformation is significant, leading to significantly different thermal expansion properties. Consequently,  $\alpha_{a0} \neq \alpha_{m0}$ . Assuming further that the inelastic properties are also equal in both phases, one obtains the mixture form

$$\psi_P(\theta, \alpha_P) = q_0 \left\{ \alpha_P + b_0^{-1} (e^{-b_0 \alpha_P} - 1) \right\} + \frac{1}{2} h_0 \alpha_P^2 \quad (3.28)$$

for the inelastic part of  $\psi$ . Lastly, the transformation contribution

$$\psi_T(\theta, l_H, z) = \psi_0 - z(\psi_{m0} - \psi_{a0}) - 3z \kappa_E(\theta) k_{tv} l_H \quad (3.29)$$

to the stored energy of the system consists of two parts. Here,  $\psi_{m0}$  and  $\psi_{a0}$  represent the chemical energies of the respective phases at  $\theta_0$ , and  $k_{tv}$  represents the relative change in unit cell volume between the two phases. Since  $\psi_T$  depends on  $l_H$ , it contributes to  $\mathbf{K}$ , i.e.

$$\mathbf{K} = \partial_{\ln \mathbf{V}_E} \psi = (k_H - 3z \kappa_E k_{tv}) \mathbf{I} + k_D \text{dir}(\text{dev}(\ln \mathbf{V}_E)) \quad (3.30)$$

now holds for the Kirchhoff stress in the two-phase system.

Given that the phase transformation is being modeled as a dissipative, stress-activated process, the extended flow rule

$$- \ln \mathbf{V}_E^* = \dot{\alpha}_P \partial_{\mathbf{K}} \sigma_{vM} + \dot{z} \partial_{\mathbf{K}} \sigma_{vT} \quad (3.31)$$

depending on both dislocation- and transformation-based processes is now relevant. Here,

$$\sigma_{vT} = (1 - z) \left\{ \frac{1}{2} k_{tp1} \sigma_{vM}^2 + \frac{1}{3} k_{tp2} \sigma_{vM}^3 \right\} \quad (3.32)$$

represents the equivalent stress measure considered by Mahnken and Schneidt (2010) determining the direction of inelastic flow resulting from the stress- or loading-induced phase transformation. This also determines the stress measure

$$\sigma_T := \mathbf{K} \cdot \partial_{\mathbf{K}} \sigma_{vT} - \partial_z \psi = (1 - z) \{ k_{tp1} \sigma_{vM}^2 + k_{tp2} \sigma_{vM}^3 \} - \partial_z \psi \quad (3.33)$$

thermodynamically conjugate to  $z$ . Rather than a rate-dependent model for inelastic and other activation processes like phase transformation outlined above, Mahnken and Schneidt (2010) work for simplicity with the rate-independent approximation. In this context,  $\dot{\alpha}_P$  is determined in the context of the yield relation  $a_P = \sigma_P - \sigma_{AP} \leq 0$  via the constraint  $\dot{\alpha}_P = 0$  when  $a_P = 0$ . Analogously, Mahnken and Schneidt (2010) model the  $\dot{z}$  in a rate- and stress-independent fashion via the Koistinen-Marburger relation

$$\dot{z} = -c_z (1 - z) \dot{\theta} \quad (3.34)$$

for  $z$  in terms of the saturation rate  $c_z$ . Note the formal analogy with the evolution relations (3.22) for dislocation density and misorientation in the case of aluminum alloys. Assuming  $c_z$  is constant, this can be integrated to yield

$$z(t) = \begin{cases} 0 & \theta \geq m_s \\ 1 - e^{-c_z(m_s - \theta)} & \theta < m_s \end{cases} \quad (3.35)$$

in terms of the starting temperature  $m_s := \theta(z = 0)$  for the transformation to martensite. For the transformation to martensite to be kinetically possible at all in the context of for example, quenching, it has been experimentally observed in addition that  $\theta$  at the start of quenching must lie above the so-called austenite starting temperature  $A_{c3}$ . Assuming no external supplies and the Taylor-Quinney approximation, the rate of heating  $\omega$  is given by

$$\begin{aligned} \omega &= \theta (\partial_\theta \mathbf{K}) \cdot \mathbf{D} + (\sigma_P - \theta \partial_\theta \sigma_P) \dot{\alpha}_P + (\sigma_T - \theta \partial_\theta \sigma_T) \dot{z} \\ &\approx \theta (\partial_\theta \mathbf{K}) \cdot \mathbf{D} + \beta_P \sigma_P \dot{\alpha}_P + \beta_T \sigma_T \dot{z}, \end{aligned} \quad (3.36)$$

again in the context of  $\text{mag}(\ln \mathbf{V}_E) \ll 1$ . Here,  $\beta_T$  represents the Taylor-Quinney coefficient associated with the transformation process.

Single-phase thermoelastic, inelastic and phase transformation-related material parameter values used for simulation of low alloy steel are presented in Table 3.2 (Mahnken and Schneidt, 2010).

$\kappa_0$	$\kappa_1$	$\mu_0$	$\mu_1$	$\alpha_{a0}$
139.4 GPa	-131.43 GPa/K	367.2 GPa	-346.21 GPa/K	$2.14 \times 10^{-5} / \text{K}$
$\alpha_{m0}$	$\theta_0$	$k_{0,\theta=293}$	$k_{0,\theta=623}$	$k_{0,\theta=973}$
$1.28 \times 10^{-5} / \text{K}$	273 K	25.3 J / m K s	27.5 J / m K s	30.5 J / m K s
$c_0$	$q_0$	$b_0$	$h_0$	$\sigma_Y$
$3.616 \times 10^6 \text{ J/m}^3 \text{Ks}$	2808.5 MPa	36.2	5.27 MPa	252.0 MPa
$\sigma_{Y1}$	$\beta_P$	$k_{tv}$	$k_{tp1}$	$k_{tp2}$
-0.344 MPa / K	0	$1.86 \times 10^{-2}$	$12.3 \times 10^{-5} / \text{MPa}$	$11.74 \times 10^{-7} / \text{MPa}^2$
$\sigma_{AT} \equiv Z_0$	$c_z$	$m_s$	$A_{c3}$	$\beta_T$
0	$1.21 \times 10^{-2}$	564.2 K	973 K	0

Table 3.2: Single-phase thermoelastic, inelastic and phase transformation-related material parameter values used for simulation of low alloy steel.

### 3.3 Algorithmic formulation

For brevity, attention is restricted here to the algorithmic formulation of the current model class for the case of aluminum alloys. Details concerning the numerical implementation of the model for steels discussed above can be found in Mahnken and Schneidt (2010). As usual, we consider an arbitrary time interval  $[t_n, t_{n+1}]$  with time-step size  $t_{n+1,n} := t_{n+1} - t_n$ . As usual, the  $\theta_n$ ,  $\mathbf{F}_n$ ,  $\alpha_{Pn}$ ,  $\epsilon_{\rho n}$ ,  $\epsilon_{\varphi n}$ , and  $\epsilon_{\delta n}$  at time  $t = t_n$  are known. In addition,  $\theta_{n+1}$  and  $\mathbf{F}_{n+1}$  are given.



The current implementation is based on backward-Euler integration of the flow rule (3.14). Projecting the result onto its trace and deviatoric parts, we obtain the system

$$\begin{aligned} l_{H_{n+1}} &= l_{H_{n+1}}^{\text{tr}}, \\ \text{dir}(\text{dev}(\ln \mathbf{V}_{E_{n+1}})) &= \text{dir}(\text{dev}(\ln \mathbf{V}_{E_{n+1}}^{\text{tr}})), \\ l_{D_{n+1}} + \sqrt{\frac{3}{2}} \alpha_{P_{n+1},n} &= l_{D_{n+1}}^{\text{tr}}. \end{aligned} \quad (3.37)$$

via (3.7). Here,  $\alpha_{P_{n+1},n} := \alpha_{P_{n+1}} - \alpha_{P_n}$ . Further,  $l_{H_{n+1}}^{\text{tr}}$  and  $l_{D_{n+1}}^{\text{tr}}$ , represent the so-called trial values of  $l_{H_{n+1}}$  and  $l_{D_{n+1}}$  determined by that

$$\ln \mathbf{V}_{E_{n+1}}^{\text{tr}} = \frac{1}{2} \ln(\mathbf{F}_{n+1} \mathbf{C}_{P_n}^{-1} \mathbf{F}_{n+1}^{\text{T}}) = \frac{1}{2} \ln(\mathbf{F}_{n+1,n} \mathbf{B}_{E_n} \mathbf{F}_{n+1,n}^{\text{T}}) \quad (3.38)$$

of the elastic left logarithmic stretch, where  $\mathbf{F}_{n+1,n} := \mathbf{F}_{n+1} \mathbf{F}_n^{-1}$  is the relative deformation gradient. In turn, (3.37) yields the algorithmic relations

$$\begin{aligned} k_{H_{n+1}} &= \kappa_0 \{l_{H_{n+1}}^{\text{tr}} + 3\alpha_0(\theta_0 - \theta_{n+1})\}, \\ k_{D_{n+1}} &= 2\mu_0 l_{D_{n+1}}^{\text{tr}} - \sqrt{6}\mu_0 \alpha_{P_{n+1},n}, \end{aligned} \quad (3.39)$$

for  $k_H$  and  $k_D$ , respectively, via (3.9). On the other hand, backward-Euler integration of (3.17)<sub>1</sub> yields the algorithmic relations

$$\begin{aligned} \text{if } \sigma_{P_{n+1}}^{\text{tr}} \leq \sigma_{\text{AP}} \quad \alpha_{P_{n+1}} &= \alpha_{P_n} \\ \text{else solve} \quad \sigma_{P_{n+1}} &= \sigma_{\text{AP}} + \sigma_{\text{DP}} \sinh^{-1} \left( \frac{z_{n+1}^{1/n_0}}{z_0^{1/n_0}} \right) \end{aligned} \quad (3.40)$$

in the usual predictor-corrector fashion via (3.19) to solve for  $\alpha_{P_{n+1}}$ . Here,

$$\sigma_{P_{n+1}}^{\text{tr}} = \sigma_{\text{vM}_{n+1}}^{\text{tr}} - (\partial_{\alpha_P} \psi)_n = \sqrt{\frac{3}{2}} k_{D_{n+1}}^{\text{tr}} - (\partial_{\alpha_P} \psi)_n \quad (3.41)$$

represents the trial-predictor value of  $\sigma_{P_{n+1}}$  as usual from (3.39)<sub>2</sub>. In any case, this yields the update  $\alpha_{P_{n+1}}$  of the accumulated equivalent inelastic deformation. In post-processing, the solution for  $\alpha_{P_{n+1}}$  obtained in this way yields the forward-Euler updates

$$\begin{aligned} \epsilon_{\rho_{n+1}} &= \epsilon_{\rho_n} + c_{\rho}(1 - \epsilon_{\rho_n}) \alpha_{P_{n+1},n}, \\ \epsilon_{\varphi_{n+1}} &= \epsilon_{\varphi_n} + c_{\varphi}(1 - \epsilon_{\varphi_n}) \alpha_{P_{n+1},n}, \\ \epsilon_{\delta_{n+1}} &= \epsilon_{\delta_n} + c_{\delta} \epsilon_{\delta_n} (1 - \epsilon_{\delta_n}) \alpha_{P_{n+1},n} \end{aligned} \quad (3.42)$$

from (3.22) and (3.23), respectively, for the non-dimensional dislocation density, misorientation and subgrain size, respectively. In addition,  $k_{D_{n+1}}$  then follows from (3.39)<sub>2</sub>. Since  $\text{dir}(\text{dev}(\ln \mathbf{V}_{E_{n+1}}))$  and  $k_{H_{n+1}}$  are determined by the trial state via (3.37)<sub>2</sub> and (3.39)<sub>1</sub>, respectively,

$$\mathbf{K}_{n+1} = k_{H_{n+1}} \mathbf{I} + k_{D_{n+1}} \text{dir}(\text{dev}(\ln \mathbf{V}_{E_{n+1}})) \quad (3.43)$$

follows from (3.8). Likewise, the forward-Euler form

$$t_{n+1,n} \omega_{n+1} = \beta_P \sigma_{P_n} \alpha_{P_{n+1},n} - 3\kappa_0 \alpha_0 \theta_n \mathbf{I} \cdot \text{sym}(\mathbf{F}_{n+1,n} - \mathbf{I}) \quad (3.44)$$

for the rate of heating then follows from (3.24).

### 3.4 Boundary, contact and friction conditions

The contact simulation in this work is based on finite-sliding interaction between deformable bodies which allows the separation and sliding of finite amplitude and arbitrary rotation of the the surfaces. The contact type used here is surface-to-surface contact which represents a more physical condition compared to node-to-surface contact. One of the surfaces is considered as the master surface and the other as the slave surface. Here the surface of the material block which undergoes larger deformation is defined as the slave surface. A linear segment of the master surface as shown in Figure 3.1 has two nodes at the vertices whereas the number of nodes for a quadratic segment is 3. Point  $x$  on the master surface determines the closest point to  $x_1$  on the slave surface. Vectors  $n$  and  $t$  represent the normal and tangent to the segment at

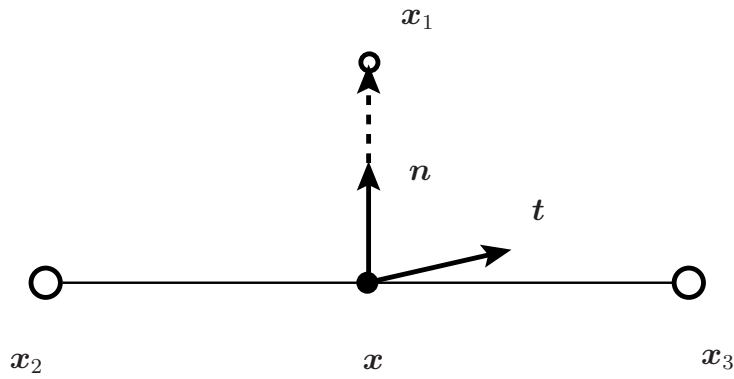


Figure 3.1: A linear segment of the master surface in contact with a node of slave surface in finite-sliding contact simulation.

point  $x$ , respectively. The point  $x$  and the normal vector  $n$  can be related to the overclosure  $h$  with the relation

$$nh = x_1 - x. \quad (3.45)$$

The position of  $x$  on the master surface can be obtained by using an interpolation function for the segment.

In this work an extended isotropic Coulomb friction model is used for the contact analysis. The classical Coulomb friction model assumes that no relative motion between the contact surfaces occurs if the frictional stress  $\tau$  is less than the critical stress  $\tau_c$

$$\tau_c = \mu_{f0}p \quad (3.46)$$

where  $\mu_{f0}$  is the friction coefficient and  $p$  is the contact pressure. In some hot metal forming processes such as extrusion, the material sticks to the container walls. To model this sticking condition we can put a limit to the critical friction stress  $\tau_c$ , being the maximum shear stress  $\tau_{\max}$  which material can undergo before sliding. Therefore  $\tau_c$  can be obtained by

$$\tau_c = \min(\mu_{f0}p, \tau_{\max}). \quad (3.47)$$

The rate of energy dissipated by contact friction forces between the contact surfaces can be obtained by

$$\dot{E}_f = \int_S \mathbf{v} \cdot \boldsymbol{\tau}_f dS, \quad (3.48)$$

where  $\tau_f$  is the friction force and  $\mathbf{v}$  is the velocity field vector.

On the free surface, radiation is modeled by the normal heat flux boundary condition

$$q_r = \varepsilon_0 \varsigma_0 (\theta^4 - \theta_0^4) \quad (3.49)$$

for the normal component  $q_c$  of the current heat flux, where  $\varepsilon_0$  is the emissivity,  $\varsigma_0$  the Stefan constant and  $\theta_0$  the temperature of the surroundings. On the surface of contact with the tool, we have

$$q_c = h_0 (\theta - \theta_{\text{tool}}) + \frac{e_{\text{billet}}}{e_{\text{billet}} + e_{\text{tool}}} \mu_{f0} p |v|, \quad (3.50)$$

where  $h_0$  is the heat transfer coefficient between the billet and container at temperature  $\theta_{\text{tool}}$ ,  $\mu_{f0}$  represents the friction coefficient,  $e_{\text{billet}}$  and  $e_{\text{tool}}$  the respective effusivities,  $p$  is the contact pressure, and  $v$  is the velocity jump across the billet-tool interface. The heat transfer coefficient  $h_0$  can be defined as

$$h_0 = h_0(\bar{\theta}, d, p, \bar{f}) \quad (3.51)$$

where  $\bar{\theta} = \frac{\theta + \theta_{\text{tool}}}{2}$  is the average of the temperatures on the surface of the tool and the material block,  $d$  is the spacing between two surfaces,  $p$  is the contact pressure transmitted across the interface between the material and the tool and  $\bar{f}$  is the average of any predefined field variable at the interacted surfaces (Abaqus, 2009). This model is also applied to the cooling process after the extruded profile is in contact with the air.

### 3.5 Numerical aspects and adaptive remeshing

Several numerical aspects should be considered for the accurate simulation of hot metal forming processes. Element distortion due to the large deformation of material can be prevented by using an adaptive remeshing scheme. The approach applied in this work is based on new meshing of the deformed geometry after each step of the simulation. In contrast to mesh refinement, this method helps us to improve the quality of the mesh and prevent rapid increase of the number of elements during the simulation.

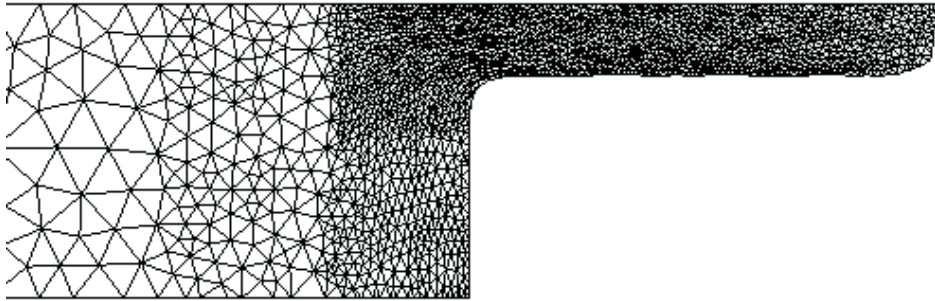


Figure 3.2: Simulation of extrusion process using adaptive mesh refinement.

As an example, the simulation of the extrusion process shown in Figure 3.2 is carried out using the adaptive refinement method (Parvizian et al., 2009). In this method after each small time step, the distorted elements will be identified in a postprocessing step. Then the distorted

elements will be divided into smaller elements. The disadvantage of this method is that the number of the element increases rapidly during the simulation though the quality of mesh does not necessarily increase. This is due to the fact that dividing distorted elements to smaller elements does not always increase the mesh quality. The distorted elements along the boundary of the model may cause a poor contact condition which can lead to numerical convergence problems. In this simulation (Figure 3.2) the number of elements starts from approximately 2000 at beginning of the simulation and increases up to approximately 8000 at the end of the simulation.

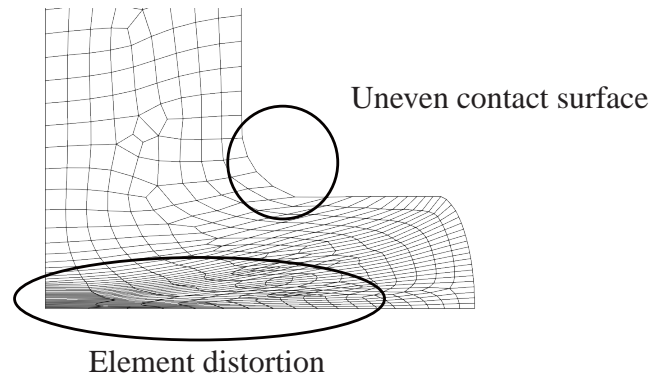


Figure 3.3: Element distortion and uneven contact surface during simulation of the the forging process without applying remeshing techniques.

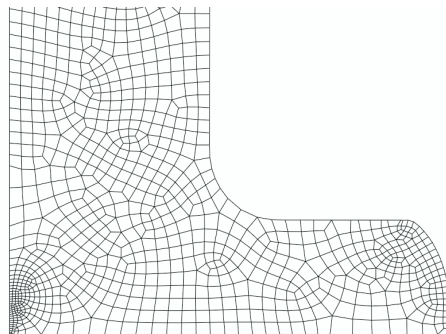


Figure 3.4: Mesh topology in simulation of the forging process using remeshing scheme.

Figure 3.3 and Figure 3.4 represent the mesh topology during simulation of forging process without and with applying the remeshing technique, respectively. The excessive element distortion and uneven contact surface in Figure 3.3 results in the numerical convergence problem and inaccuracy of the results. Applying a remeshing technique as shown in Figure 3.4 helps increase the mesh quality and to avoid a high number of contact iterations by having a smooth contact surface between the material and the tool. As shown in the schematic algorithm of our remeshing system in Figure 3.5, an initial input file for the simulation is created in a preprocessing step. This input file is solved for one small time step using an FE-solver, which is Abaqus in our case. The size of the time step should be small enough to prevent any element distortion or convergence problems due to the high number of contact iterations. After each remeshing step, the solution of the old mesh including all the internal state dependent variables is transferred to the new mesh. Here the values of the internal dependent state variables (SDVs) at the end of

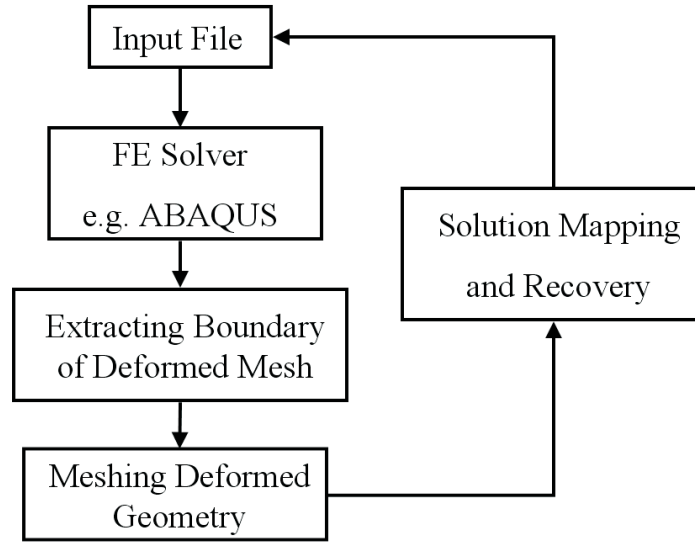


Figure 3.5: Remeshing system developed with the help of Python programming

every step are given as the initial values of SDVs in the new step after remeshing. A common transfer procedure is for example working with the finite element interpolation ansatz

$$\epsilon(\xi) = \sum_{i=1}^n \epsilon_i N_i(\xi) \quad (3.52)$$

with  $\epsilon_i$  as recovered values. In contrast to refinement, remeshing does not change the element density in the new mesh. This means that less interpolation of the result is required and therefore the accuracy of the final solution will be higher.

A standard method to recover a solution to the nodes is nodal averaging. This method is simple to implement and very efficient from the numerical point of view. The disadvantage of the simple nodal averaging is the strong effect of numerical diffusion when performing a large number of remeshing steps.

More advanced recovery procedures are based on polynomial smoothing techniques such as, e.g. the well known superconvergent patch recovery method (Zienkiewicz and Zhu, 1992, 1995) or local projection techniques (Hinton and Campbell, 1974). All of these methods are based on the existence of certain points at the interior of the element, where the finite element values are closer to the exact solution than elsewhere. These super convergence or best-fit points are sampling points for the recovery procedure. Using the finite element value at the position of the centroid or Gauss point, we can perform a super convergence patch recovery (Zienkiewicz and Zhu, 1992) to obtain a smoothed field of internal variables. For this purpose we assume an enhanced representation of any internal variable in the form of

$$\epsilon^*(\mathbf{x}) = \mathbf{p}(\mathbf{x}) \cdot \mathbf{a} \quad (3.53)$$

with  $\mathbf{p}(\mathbf{x})$  being a polynomial array and  $\mathbf{a}$  a set of unknown parameters. Minimizing the common least square fit objective function for a set of  $n$  sample points

$$F(\mathbf{a}) = \sum_{i=1}^n (\epsilon_i - \epsilon^*)^2 = \sum_{i=1}^n (\epsilon_i - \mathbf{p}(\mathbf{x}_i) \cdot \mathbf{a})^2 \quad (3.54)$$

yields the linear system of equations

$$\mathbf{A}\mathbf{a} = \mathbf{b}, \quad (3.55)$$

with

$$\mathbf{A} = \sum_{i=1}^n \mathbf{p}(\mathbf{x}_i); \quad \mathbf{b} = \sum \mathbf{p}(\mathbf{x}_i)^T \epsilon_i \quad (3.56)$$

Solving the above minimization problem, gives us the smooth field of the internal state variables.

### 3.6 Applications and results

The above model and remeshing strategy are now applied to the numerical simulation of the thermomechanically-coupled extrusion process of aluminum alloys and forging of steels. Both models are implemented as user material subroutines (UMAT) in the FE-software Abaqus. Element type CAX4TR, a quadrilateral axisymmetric element with temperature as a degree of freedom, is applied in a coupled temperature-displacement simulation for both cases. Abaqus provides access to the output database of the simulation results by using the Python programming language. Using this advantage, the described remeshing system including a graphical user interface (GUI) is developed with the help of Python programming. This system enables us to check the mesh quality or any other remeshing criteria in a postprocessing step. Due to the axisymmetric geometry, both processes are partly modeled. All of the tools in both cases are modeled as deformable bodies with elastic behavior and meshed with quadrilateral elements.

#### 3.6.1 Extrusion of aluminum alloys

The geometry and configuration for simulation of the extrusion process is presented in Figure 3.6. The ram with  $v = 5$  mm/s forces the material to pass through the die. Temperature of the material is 673 K, and that of the container and the die is 573 K and the ratio  $\frac{R}{r} = 5$ . The material model and parameters are as described in the material model section for aluminum alloys.

The application of the described remeshing system for simulation of the extrusion process is presented in Figure 3.7. Figure 3.7 (I) shows the starting mesh at the beginning of one step. Figure 3.7 (II) represents the same mesh at the end of the step. As can be seen in the area inside the box, the elements are deformed excessively at the end of the step. Figure 3.7 (III) is the same deformed geometry as in part II but with a new mesh which is used for starting a new simulation step. This procedure is repeated in every remeshing step. The number of required remeshing steps depends on the complexity of the geometry and contact conditions.

Figure 3.8 shows the distribution of equivalent plastic strain in simulation of the extrusion process. In the die exit area where material is excessively deformed, the equivalent plastic strain is higher. The high value of equivalent plastic strain in the area close to the corner of the container is due to friction and the sticking condition. In Figure 3.9 and Figure 3.10 the distribution of the non-dimensional subgrain size as an example of an internal state variable is presented in absence and presence of the frictional boundary conditions, respectively. As can be seen from these two figures, the evolution of subgrain size shows quite a different behavior

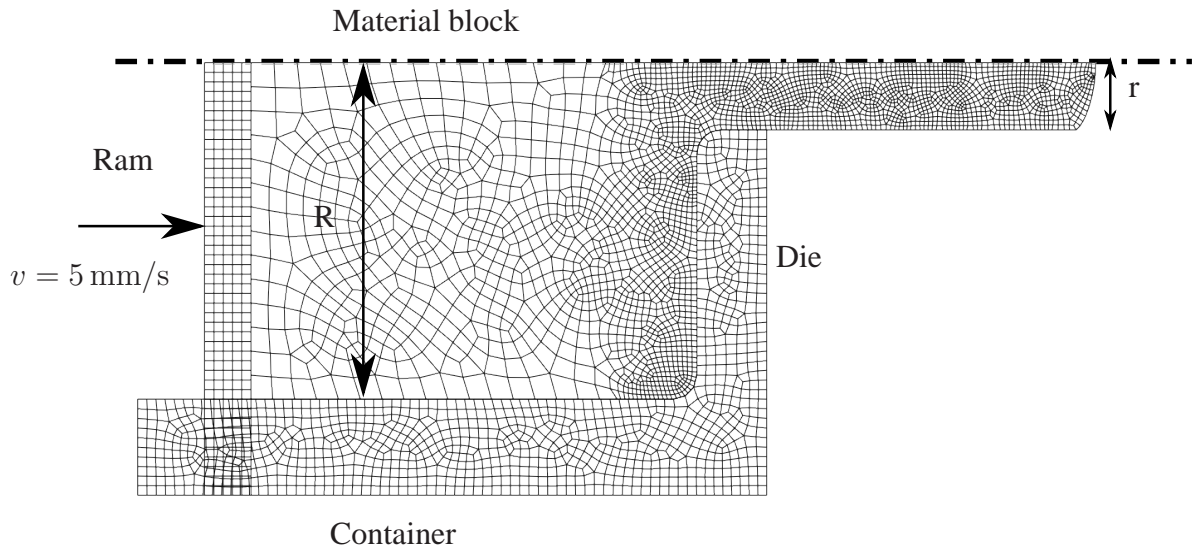


Figure 3.6: Geometry and configuration for simulation of extrusion process

in these two cases. In absence of friction, the subgrain size decreases in the die exit area and in areas close to the die, whereas in Figure 3.10, while applying friction, a so-called dead material zone (DMZ) (Saha, 2000) can be observed. This DMZ, which is also detected in experimental studies of the extrusion process (Schikorra et al., 2007d) shown in Figure 3.12, represents an area where the material has small or no movement and deformation. The equivalent plastic strain as well as the internal state variable with its evolution law depending on equivalent plastic strain do not develop in the DMZ. This shows the significant influence of accurate modeling of boundary and interaction conditions on the simulation of metal forming processes. The decreasing tendency of subgrain size in a path from ram to the die exit area, which is presented in Figure 3.10, is also observed in experimental investigation (Kayser et al., 2009).

The evolution of subgrain size in the MDZ, the die exit and the DMZ area during the simulation is shown in Figure 3.11, the points of measurements are shown in Figure 3.12 and denoted by 1, 2 and 3 respectively. The evolution of subgrain size occurs slowly in DMZ, whereas in MDZ and the die exit area the size of subgrains decreases rapidly towards the saturation value.

### 3.6.2 Forging of steel

The forging process used here for the simulation is described in (Steinhoff et al., 2005) and (Weidig et al., 2008). The geometry and configuration of the model is shown in Figure 3.13. This process consists of three steps: heating, forming and cooling. During the heating step, the workpiece will warm up by a heat flux on its surface for 12 seconds. During the forming step the cold forming die at temperature  $\theta_0 = 693$  K with velocity  $v = 1$  mm/s presses the material block to take the desired shape in 28 seconds. Finally, during the cooling phase the deformed material cools down. The results presented in this work represent the state of the material block at the end of the forming step.

Figs. 3.15, 3.16 and 3.17 show the distribution of the temperature, the equivalent plastic strain and the volume fraction of martensite, respectively. In Figure 3.17 the value of 1.0 is pure martensite and 0.0 is pure austenite. The distribution of the volume fraction of martensite is

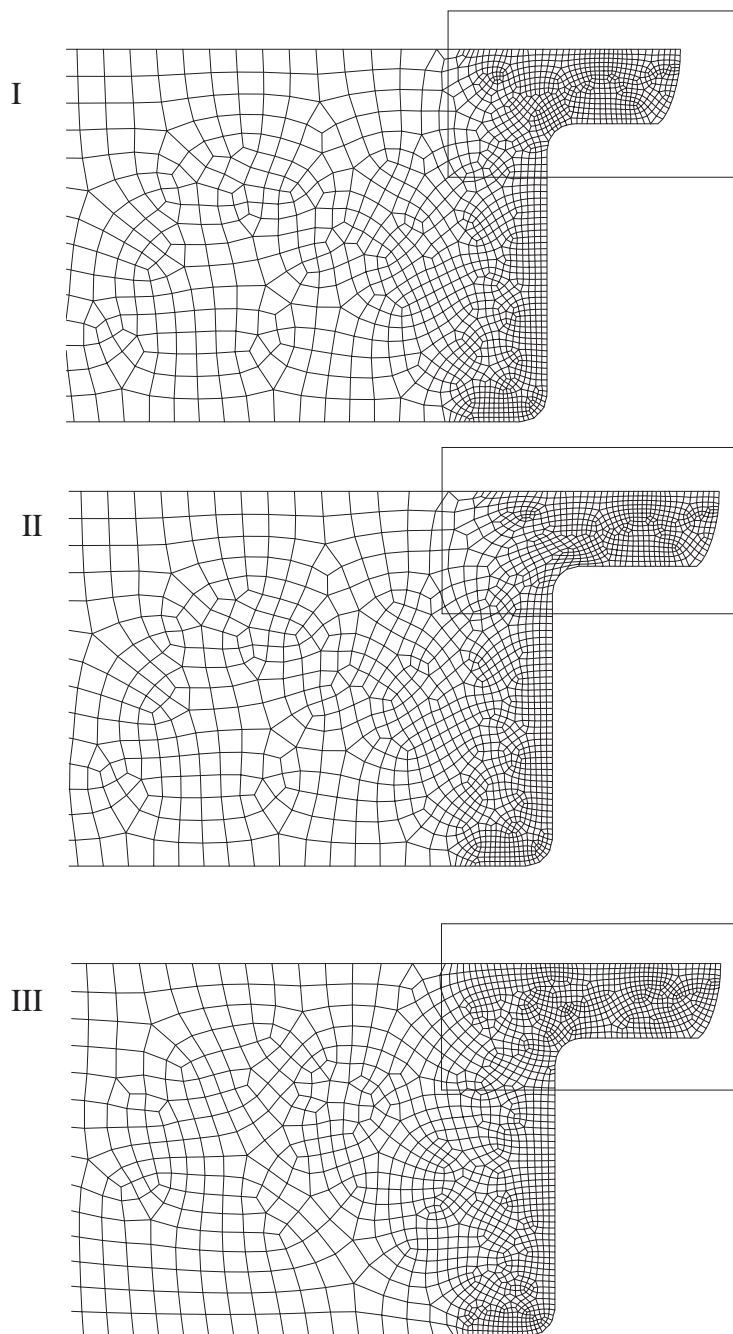


Figure 3.7: FE-discretization and remeshing for the extrusion simulation. I) mesh at beginning of one step, II) mesh at the end of the same step, III) mesh after new meshing of the deformed geometry of part II.

in good qualitative agreement with the experimental results of Steinhoff et al. (2005) shown in Figure 3.18. As can be expected, the value of equivalent plastic strain in the middle of the material block is relatively higher. A quantitative comparison of the results with experiment requires better knowledge of the material parameters for the steel 51CrV4 used in the experiment.

Figure 3.14 shows the development of the mesh during the simulation of the forging process. To avoid extra interpolations, no mesh coarsening is applied here. Therefore the element size



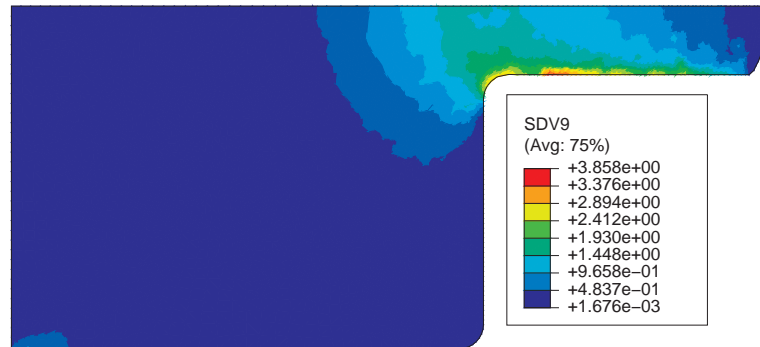


Figure 3.8: Distribution of equivalent plastic strain in simulation of extrusion process.

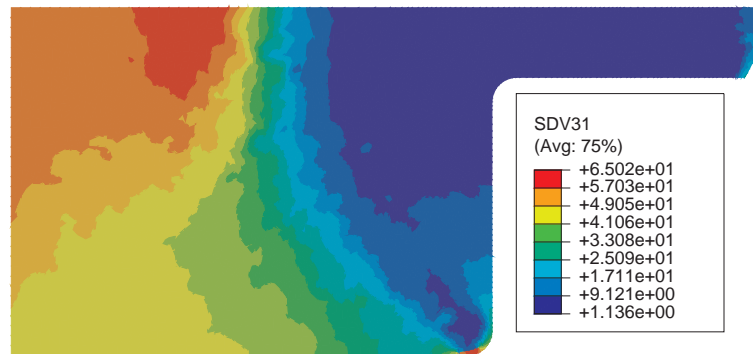


Figure 3.9: Distribution of non-dimensional subgrain size during simulation of extrusion process in absence of friction.

decreases in some parts of the model, e.g. left corner in Figure 3.14, where material undergoes more pressure during the simulation.

### 3.7 Conclusions

In this chapter, a continuum thermodynamic framework for the thermoelastic, viscoplastic material behavior of Al- and steel-alloys and the evolution of microstructural properties as internal variables has been formulated and applied to the FE-simulation of extrusion and forging processes. For prediction of microstructure parameters, i.e. subgrain size, misorientation angle and dislocation density, a phenomenological model is presented which is based on the physical assumption that microstructure parameters saturate after reaching a steady-state condition. As shown by the comparison of the simulation predictions and corresponding experimental results,

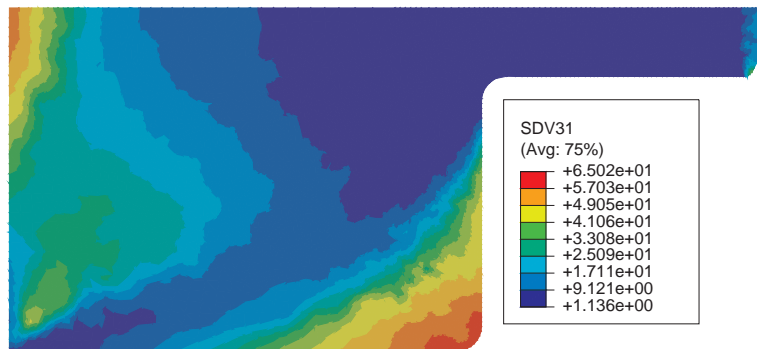


Figure 3.10: Distribution of non-dimensional subgrain size during simulation of the extrusion process with frictional interactions.

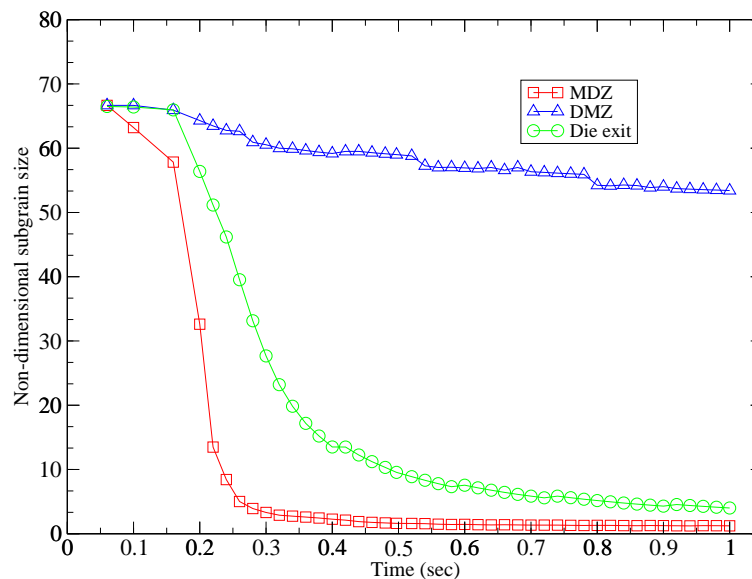


Figure 3.11: Evolution of non-dimensional subgrain size during the extrusion process in the die exit, the dead material zone (DMZ) and the main deformation zone (MDZ).

the predictions of the model are in qualitatively good agreement with experimental observations in different zones of the material block. The remeshing of the deformed geometry instead of mesh refinement increases the numerical efficiency and accuracy of the results by reducing the number of elements. It was also shown that boundary conditions such as friction and thermal contact conditions have a significant influence on the evolution of microstructure in the material block. In the following chapters, a more quantitative comparison of the results with experimental results will be given using material parameter identification.

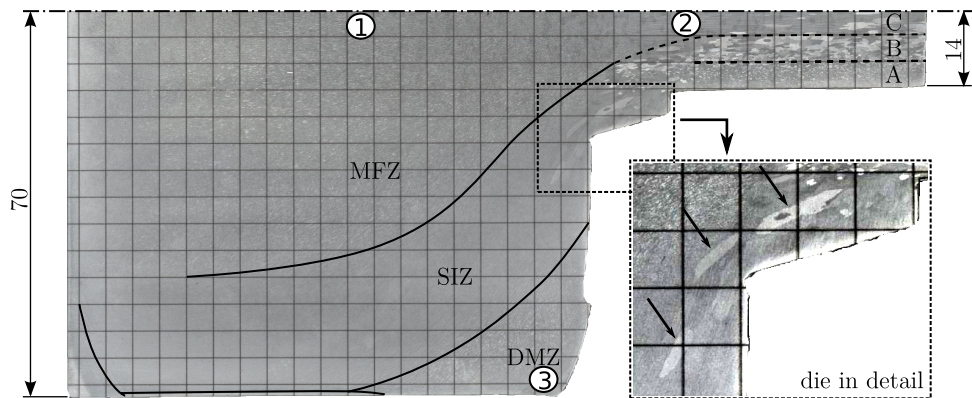


Figure 3.12: Experimental results showing dead material zone (DMZ), main deformation zone (MDZ), shear intensive zone (SIZ) and die exit area.

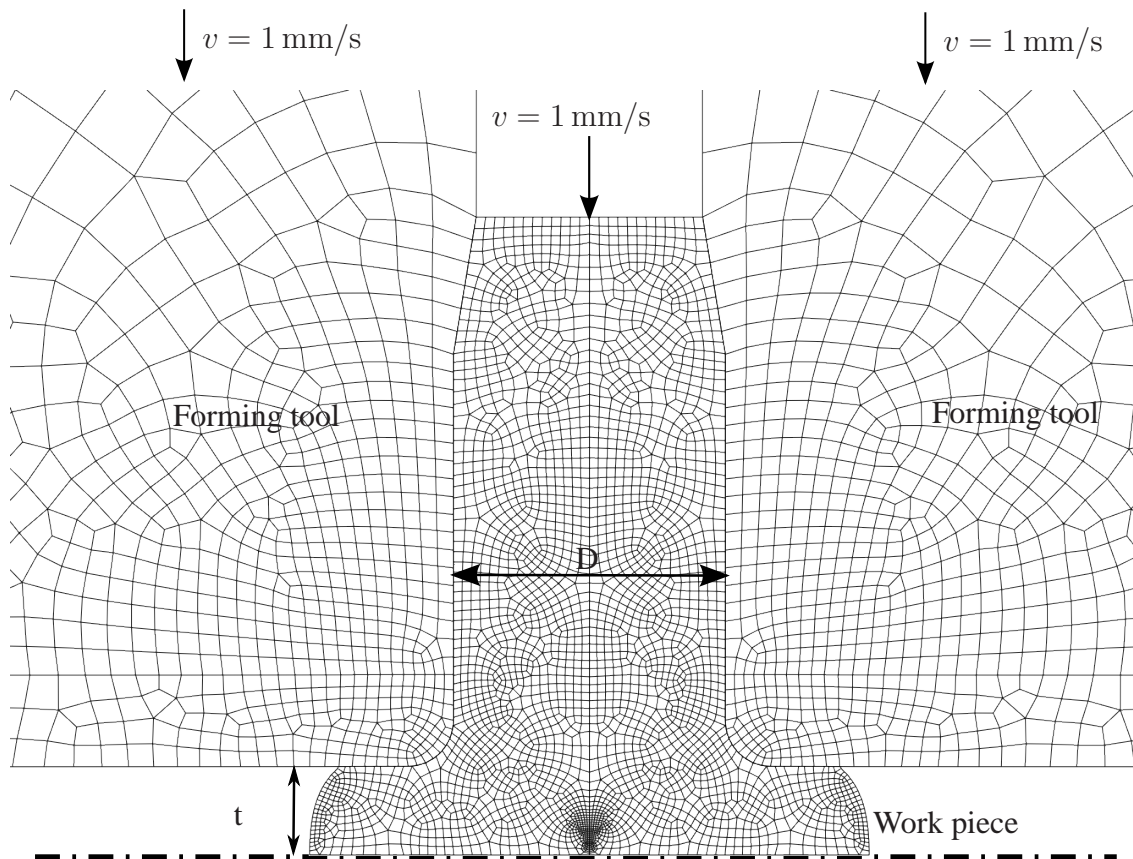


Figure 3.13: Geometry and configuration for simulation of forging process

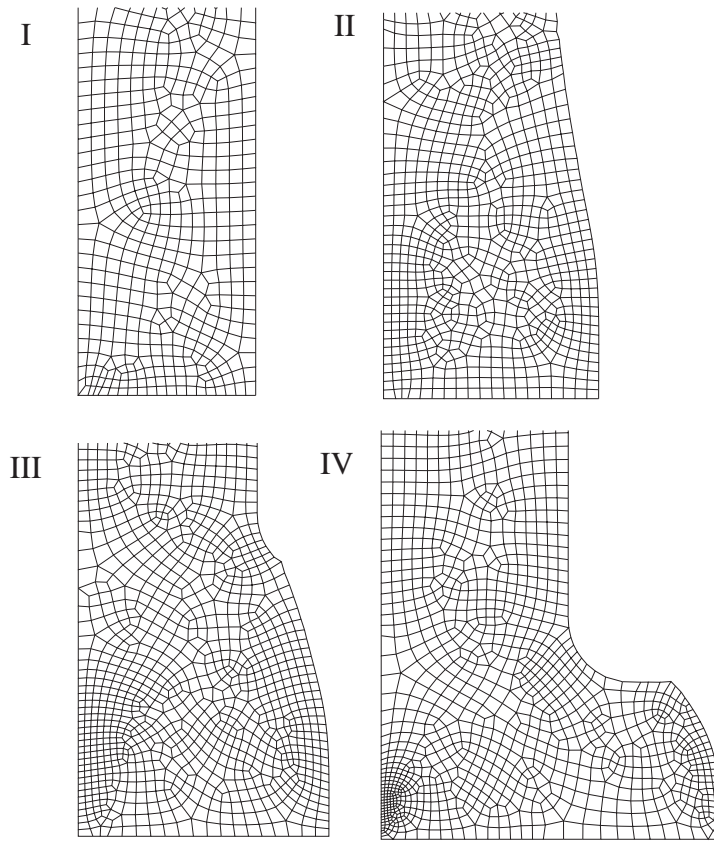


Figure 3.14: Development of mesh topology during simulation of forging process based on remeshing of deformed geometry in each step.

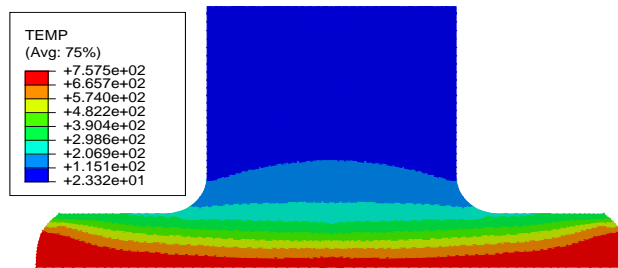


Figure 3.15: Distribution of temperature in simulation of forging process.

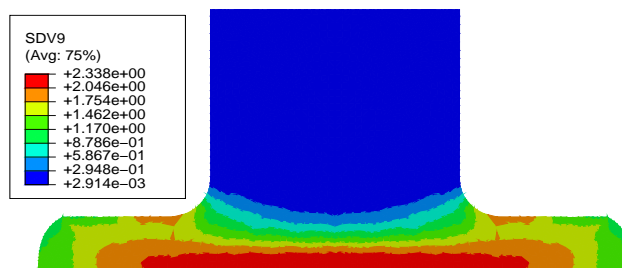


Figure 3.16: Distribution of equivalent plastic strain in simulation of forging process.

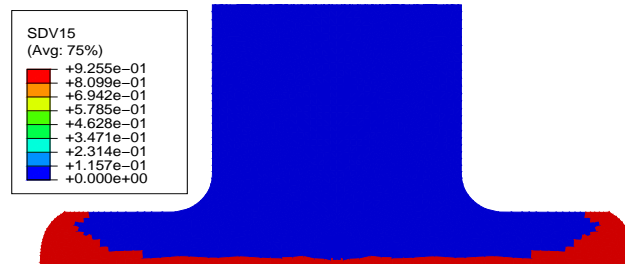


Figure 3.17: Distribution of volume fraction of martensite in simulation of forging process.

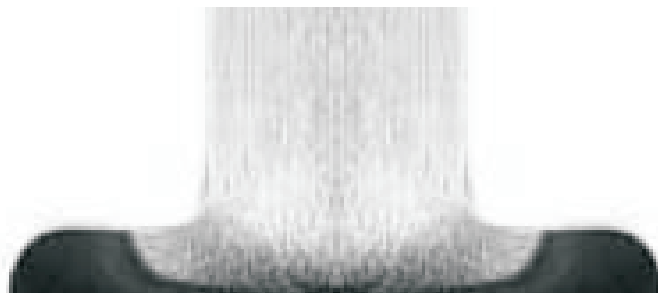


Figure 3.18: Grinding surface pattern of real structure obtained from experimental results of forging process.



## Chapter 4

# Modeling of dynamic microstructure evolution of EN AW–6082 alloy during hot forward extrusion\*

**abstract** The aim of this work is to briefly present a model for predicting and simulating the evolution of microstructure, in particular the evolution of grains during hot forming processes of aluminum alloy EN AW–6082 and to give a comparison with the experimental results. The model is a physically motivated phenomenological one based on internal state dependent variables. The microstructure evolution is a temperature dependent process and is simulated in a fully-coupled thermomechanical process with the help of the Finite Element software Abaqus. The results are compared and verified with experimental results obtained by the EBSD measurement of a small-scale extrusion process established for scientific purposes. The simulation results are in reasonable agreement with the experimental results.

### 4.1 Introduction

Material properties of metal forming products are of industrial interest for product optimization or as the initial state for further processing purposes such as annealing. Finite Element (FE) simulation of forming processes is now well-established at the macro level (Kobayashi et al., 1989) for optimization and prediction of process parameters for example, but does not provide sufficient information about the material properties of the final product. To obtain the material behavior of the final product, it is necessary to study the microstructure development of the material during forming processes. There are generally two approaches for simulation of microstructure evolution during forming processes: phenomenological models and physically-based models (Grong and Shercliff, 2002). In phenomenological models the final state of the recrystallized structure is modeled in a post-processing process without considering any evolution law for the microstructure. The empirical Johnson–Mehl–Avrami–Kolmogorov (JMAK) relation is widely used to determine the recrystallized grain size (Bontcheva et al., 2006; Grass et al., 2003). The JMAK relation for nucleation and growth transformations works very well for most solid state transformations but regularly fails when applied to the recrystallization of plastically deformed metals (Rollett et al., 1989). In contrast to the phenomenological models, physically-based models give more insight into the material behavior at the micro-scale. In physically-based models the internal state dependent variables are used to describe the state of the microstructure parameters during the process (Shercliff and Lovatt, 1999). The internal

---

\*Results partly published in Parvizian et al. (2011)

state variables are well suited for describing the microstructure properties in forming processes. The evolution law of internal state variables

$$\frac{dS_i}{dt} = f_i(S_{1,\dots,n}, \dot{\alpha}_p(t), T(\dot{\alpha}_p), \dots) \quad (4.1)$$

in metal forming applications is usually given as a function of internal state dependent variables  $S_i$  ( $i = 1, \dots, n$ ), the rate of equivalent plastic strain  $\dot{\alpha}_p$  and the temperature  $T$ . In thermomechanically-coupled processes the temperature increases significantly during the process. In fully-coupled models of more complex processes, in which microstructure evolution leads to heat generation e.g. solidification, the evolution of temperature is given as a function of the internal state dependent variables  $S_i$  as well as time  $t$ . In a fully-coupled approach the constitutive relation for material behavior

$$\sigma_f = g(S_{1,\dots,n}, \alpha, \dot{\alpha}_p, T) \quad (4.2)$$

is microstructurally-based and coupled directly with the state dependent variables  $S_i$  ( $i = 1, \dots, n$ ). An appropriate coupled approach is given by describing the flow stress of work hardened microstructure as a function of two internal state variables, the dislocation density  $\rho$  and the subgrain size  $\delta$ , and the size of the Burgers vector  $\mathbf{b}$  (Furu et al., 1996; Nes and Furu, 1995). In the current work a thermo-elastic visco-plastic empirical model is used to describe the macroscopic behavior of the material and a physically-based model is applied to model the evolution of microstructure properties as internal state variables. In the following sections this model is presented and verified by the EBSD measurements of a small scaled extrusion process.

## 4.2 Microstructure characterization

The microstructure evolution during an extrusion process is affected by local changes in strain, temperature and strain rate. Especially for aluminum alloys, differences in grain size, grain shape, texture and precipitation behavior have to be considered, since these are the controlling factors determining the local strength, the fatigue properties and the corrosion behavior of the final work piece. For high strength applications of aluminum alloys, generally small grain sizes are desired (Humphreys and Hatherly, 2004) which can be achieved via recovery or recrystallization. Due to the high stacking fault energy of aluminum alloys, dislocations formed during plastic deformation have a high tendency to annihilate in a way that the recovery process is favored instead of the classical recrystallization mechanism which requires a substantial increase in dislocation density. In addition to the local evolution of grain structure, data on the strength of the alloy at the deformation temperature is also required for accurate modeling of the local resulting properties following the extrusion process. Therefore it is necessary to determine the tensile strengths of the material at higher temperatures as well as the grain morphology depending on the position in the extrusion billet.

Slow cooling rates after the hot deformation of aluminum alloys leave enough time for static recrystallization and have to be avoided for a clear investigation of the kinetics of dynamic microstructure evolution. In order to overcome this problem by quenching the workpiece directly after extrusion, a small-scale forward axisymmetric extrusion setup was designed and is presented in Figure 4.1.



The setup consists of an externally heated container with an inserted die, a radiatively heated ram (693 K) and a base frame. The container also acted as the die holder. Ram and punch were mounted horizontally in a universal testing machine, the Zwick 250. The die and the billet, both coated with boron nitride for easy release, were placed into the container and heated up in an air circulating oven to the homogenization temperature of 823 K. Using a gripper, this unit was placed on the base frame, thermocouples were inserted into the container and the extrusion process was initiated. The extrusion process was controlled by the control system of the universal testing machine. By this, speed control of the ram (5 mm/s) was possible and a stroke of 10 mm was defined. The extrudate ran out downwards into a water bath for quenching. As soon as the extrusion stopped, the extrudate was cut off at a distance of approximately 30 mm from the die exit by using a bolt cutter. The unit composed of the container, the die and the butt was then removed from the machine and quenched together in a water bath. The billet was extruded in 2 seconds. The handling of the tool-workpiece system was carried out in 3 seconds after extrusion. Measurements of the thermocouples inserted in the tool-workpiece system showed that the extrusion butt was cooled down to the critical temperature (573 K for EN AW-6082 (Grong and Shercliff, 2002)) in 3 seconds (Güzel et al., 2011). This small-scale setup reduces all undesired geometrical and thermal effects. A block of aluminum alloy EN AW-6082 was partly extruded and the unit of container, die and butt was removed from the machine and quenched together in a water bath. As the extrusion butt was quenched immediately after extrusion, static recrystallization and grain growth were avoided and the evolution of grain structure during deformation was preserved.

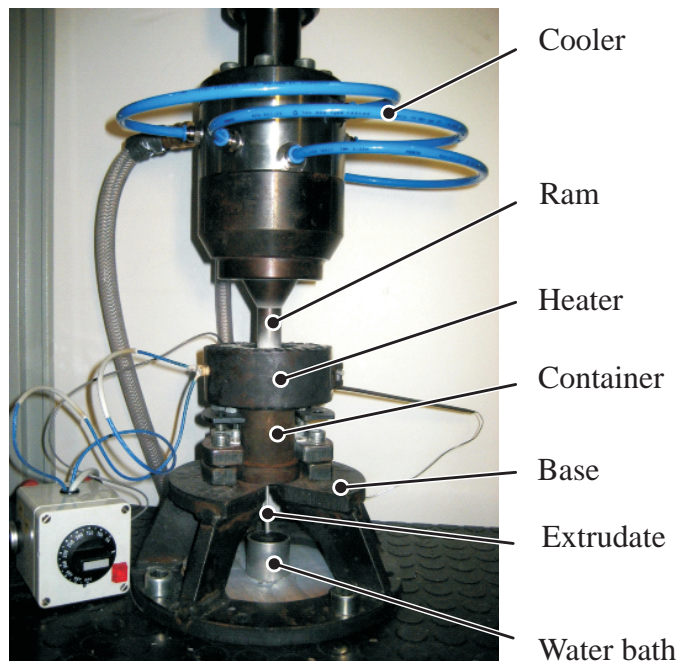


Figure 4.1: Small-scale forward extrusion setup (Güzel et al., 2011).

The tensile strength of the aluminum alloy EN AW-6082 at elevated temperatures were determined using a servo hydraulic load frame which allowed for heating the specimens up to

temperatures as high as 823 K via induction heating. The temperature within the gauge length was controlled with thermocouples micro-spot-welded directly onto the specimen. At each temperature (623, 673 and 723 K) the tensile strength was determined for different displacement rates (0.1, 1 and 10 mm/s). In Figure 4.2 the true stress–true strain response for the EN AW–6082 alloy at 723 K is shown for different displacement rates. As expected, the ultimate tensile stress and the 0.2% offset yield stress increase with increasing rate of deformation. This behavior was observed for all investigated temperatures (623, 673 and 723 K) in the EN AW–6082 alloy system. Figure 4.3 presents the true stress–true strain response of EN AW–6082 for different temperatures (623, 673 and 723 K) and a displacement rate of 1.0 mm/s. At a temperature of 623 K, the material softens with increasing strain, whereas at higher temperatures the material behavior is influenced mainly by temperature and rate of deformation and the softening effect is reduced by increasing the temperature. Due to the induction heating system used, the temperature within the gauge length was homogeneous only up to 20% true strain. Thus, the true stress–true strain response is only shown up to this value. The softening of the material after reaching the flow stress is mainly due to the rise in temperature. The energy of plastic work which converts to heat increases the temperature of the material and consequently causes the material to soften.

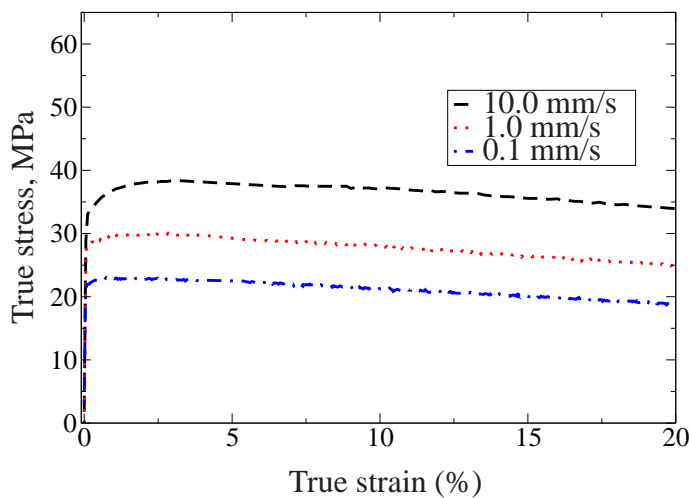


Figure 4.2: True stress-true strain response of EN AW–6082 at 723 K for different cross head displacement rates.

Next, EBSD measurements at points characteristic for different deformation zones in the extrusion billet out of EN AW–6082 were performed in order to determine the grain and subgrain structure. After sectioning the billet, the pieces were mechanically polished down to a grid size of 5  $\mu\text{m}$  and then electro-polished using a 5% perchloric acid solution under an applied potential of 30 V at 648 K. In previous experiments reported in Schikorra et al. (2007c, 2008) the time to remove the extrusion remainder from the container was not short enough to avoid static recrystallization (SRX).

Due to the highest strains and temperatures in the shear intensive zone (SIZ), the focus in this study lies on the evolution of microstructure at different positions, mainly in the SIZ and the subsequent exit profile zone (EPZ). The positions of selected points are obtained by point tracking so that they are on the same material flow path, and the evolution history of the grains

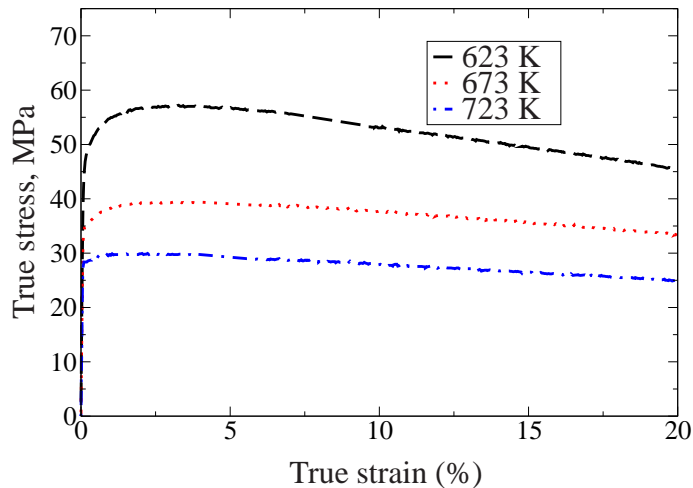


Figure 4.3: True stress-true strain response of EN AW-6082 at cross head displacement rate of 1.0 mm/s for different temperatures.

and subgrains can be followed from the beginning to the end of the process. The schematic representation of the extrusion model and the positions of the investigated points are shown in Figure 4.4. As presented in Figure 4.4, two different paths are selected for investigation: black path and red path. The results of the black path are used for parameter identification of the model and the red path for validation of the simulation results. These paths will be discussed in detail in the next sections. Because of axisymmetric geometry of the model, only half of the model is illustrated in Figure 4.4. To compare the state of the microstructure of the material before and after deformation, the microstructure of the undeformed material is also obtained by the EBSD measurement (Figure 4.5). Comparing the high-angle ( $15^\circ$ ) and low-angle ( $5^\circ$ ) boundaries in Figure 4.5 shows that the undeformed material (O) contains only few low-angle boundary grains and the microstructure mostly consists of high-angle grains.

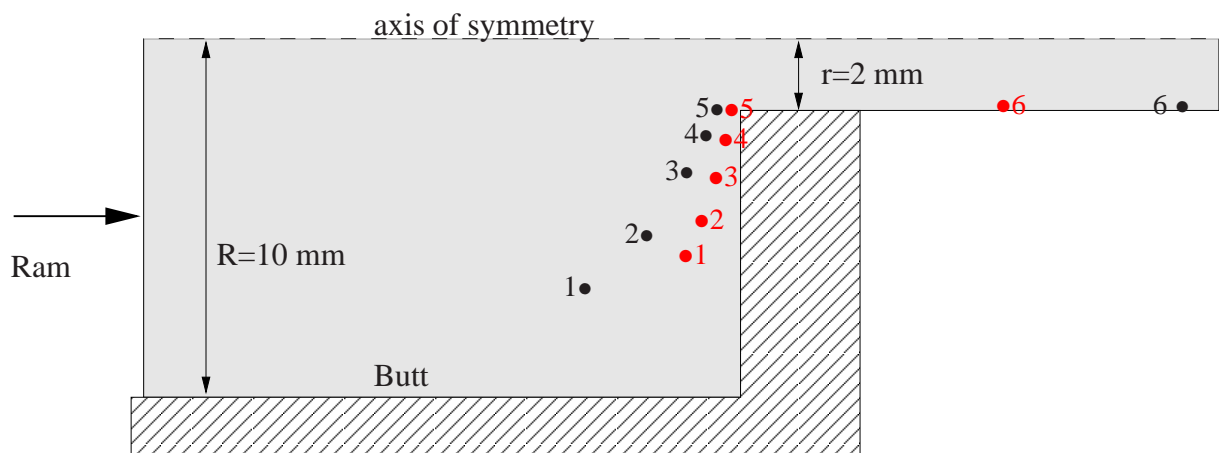


Figure 4.4: Schematic representation of the small-scale extrusion with position of two measured paths (black path and red path).

The visual representation of EBSD measurements at the investigated points of the black path is shown in Figure 4.6. In this representation the grains are distinguished by misorientations

higher than  $15^\circ$ . As depicted in Figure 4.6 all measured areas show long elongated grains having a preferred orientation with respect to the flow direction of the material. The investigated points of the red path also show the same tendency (Figure 4.7). This behavior is typical for the SIZ and is also detectable with a light optical microscope (Schikorra et al., 2007c). The investigated points of the red path are closer to the walls of the container and the dead material zone. Therefore as it is presented in Figure 4.7, the evolution of the microstructure is slower compared to the black path. For the detection of low-angle grain boundaries and the accompanied formation of subgrains the EBSD system is indispensable, since it also allows for determining small angle grain boundaries (misorientation angles lower than  $15^\circ$ ) in addition to high-angle grain boundaries (misorientation angles higher than  $15^\circ$ ). In Figure 4.8 the boundaries of low-angle ( $<5^\circ$ ) grains of the black path are represented. With an increasing deformation degree along the SIZ, the development of the low-angle grain boundaries in elongated grains can be observed. At each position in the SIZ the formation of subgrains within the long elongated grains becomes apparent. Since even at the surface of the EPZ subgrain formation is visible (Figure 4.8, position 5), the designed setup is suitable to completely avoid SRX. Figure 4.9 shows the evolution of low-angle grains along the red path obtained by the EBSD method. The starting point ( $R_1$ ), which is very close to the DMZ area, contains only a few low-angle grains. The formation of new low-angle grains is also observed in the investigated points of the red path. The current findings therefore constitute a first data base for a realistic modeling effort of the dynamic microstructure evolution during hot forward extrusion.

The statistical evaluation of the EBSD results for the median grain size of the undeformed aluminum billet and the measured points of the black path are presented in Figure 4.10. The median grain size for all of the six measured points in SIZ is smaller than the original grain size.

The EBSD data was evaluated and visualized by the MTEX toolbox, an open source quantitative texture analysis toolbox in MATLAB.

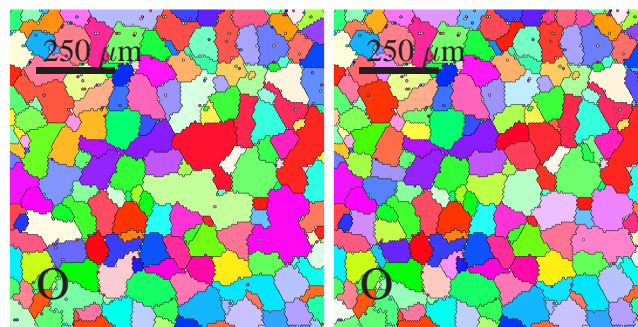


Figure 4.5: High-angle ( $>15^\circ$ ) (left) and low-angle ( $<5^\circ$ ) (right) grains of undeformed material (O) obtained by the EBSD measurement.

In Figure 4.11 the mean low-angle boundary misorientation of the undeformed material and other measured points of the black path are presented. The mean misorientation between low-angle boundary grains decreases in direction of the material flow until point 4 and increases from that point on. The grains are oriented in the direction of material flow and therefore the misorientation between the neighboring grains decreases. After reaching a minimum value at point 4 in Figure 4.11, the low boundary grains start to separate and form new boundaries which

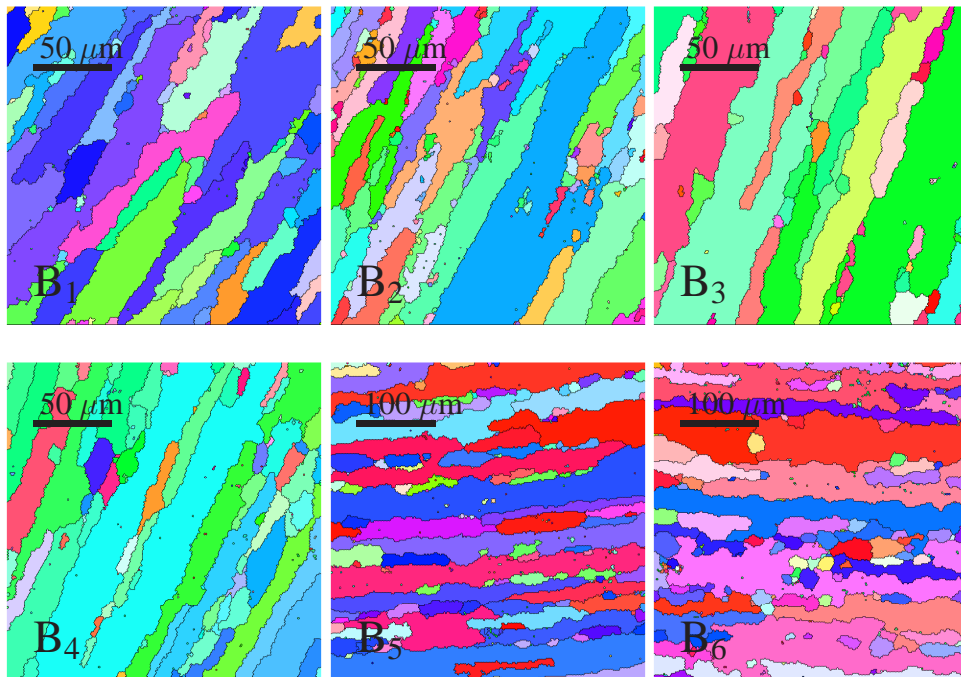


Figure 4.6: High-angle ( $>15^\circ$ ) grains of investigated points (black path) of the extrusion butt obtained by the EBSD measurement.

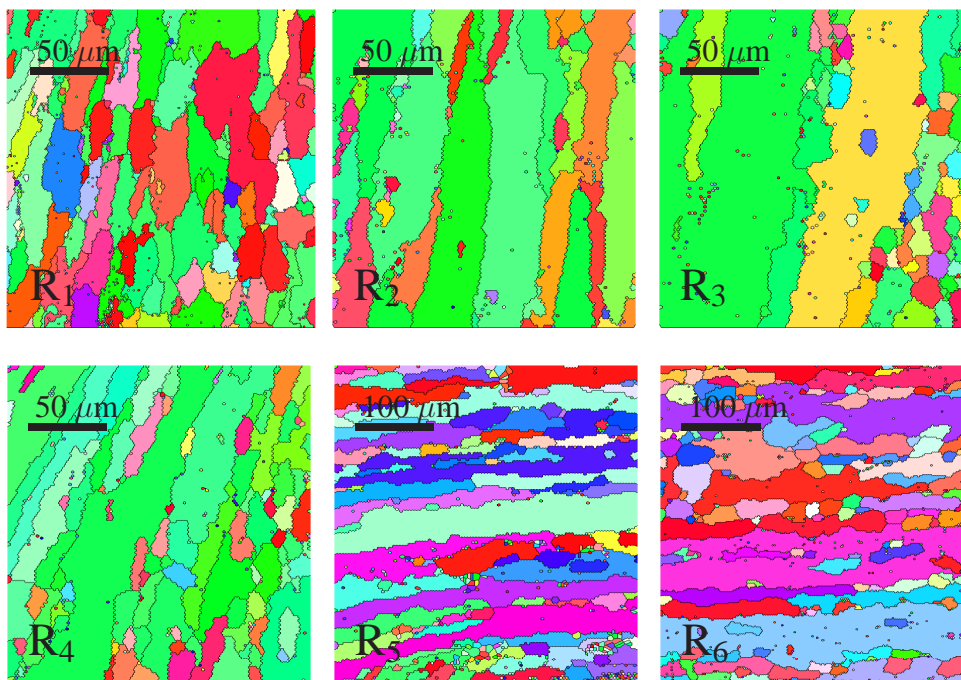


Figure 4.7: High-angle ( $>15^\circ$ ) grains of investigated points (red path) of the extrusion butt obtained by the EBSD measurement.

lead to increasing misorientation between adjacent grains. This behavior coupled with the decreasing median grain size (Figure 4.10) is evidence of the geometric dynamic recrystallization (GDRX) phenomenon occurring during the process. In the GDRX process, grain boundaries

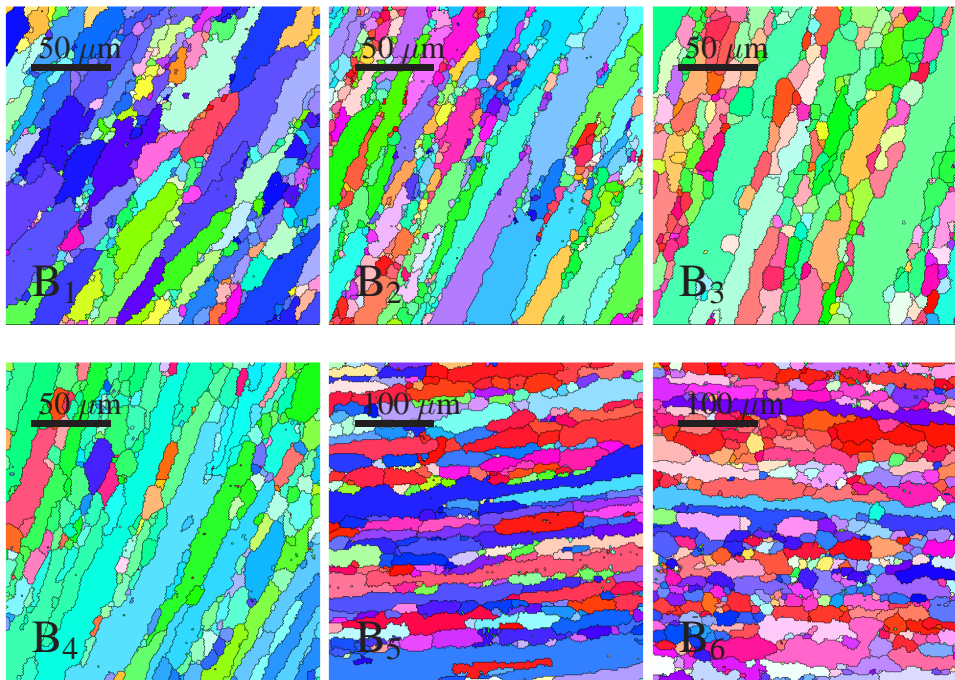


Figure 4.8: Low-angle ( $<5^\circ$ ) grains of investigated points (black path) of the extrusion butt obtained by the EBSD measurement.

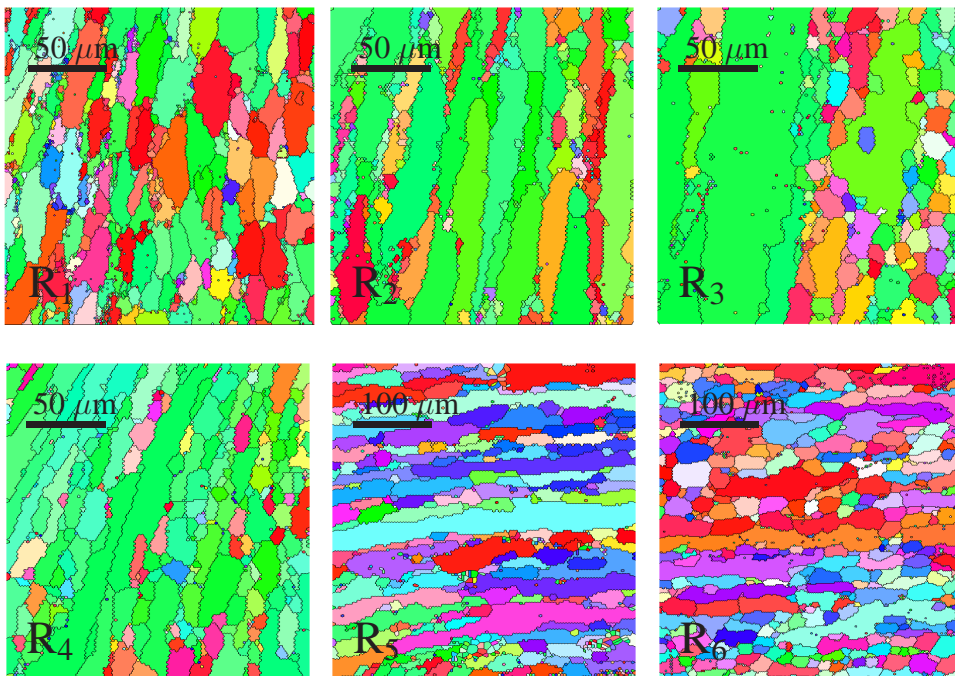


Figure 4.9: Low-angle ( $<5^\circ$ ) grains of investigated points (red path) of the extrusion butt obtained by the EBSD measurement.

which have become serrated during formation of subgrains in the course of hot deformation recombine as new refined grains (Blum et al., 1996). The mean low-angle boundary misorien-

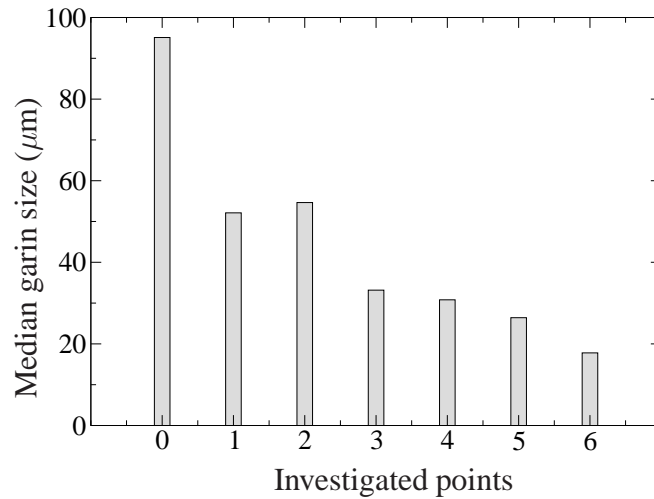


Figure 4.10: The median grain size of undeformed material and six measured points of the black path in the billet obtained by the EBSD measurements.

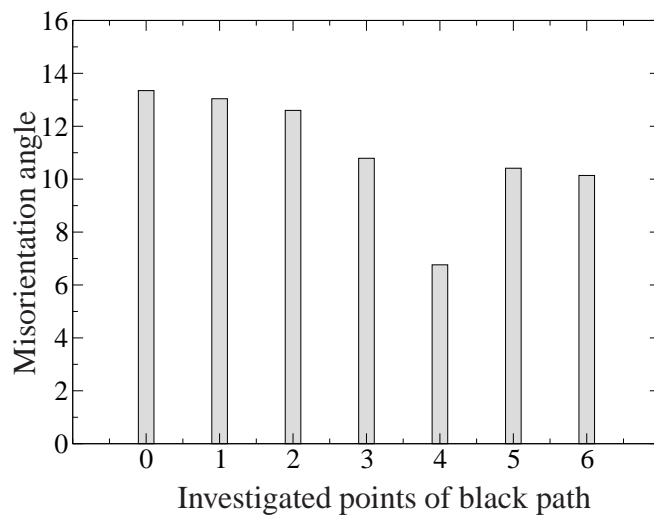


Figure 4.11: The mean low-angle boundary misorientation ( $<15^\circ$ ) of undeformed material and measured points of the black path in the billet obtained by the EBSD measurements.

tation of the red path presented in Figure 4.12 is similar to the black path. The misorientation decreases down to point  $R_4$  and increases from there on.

The low-angle and high-angle boundary size of the red path are shown in Figure 4.13. The high-angle grains develop from the original grain size to a saturated value which is close to size of the low-angle grains, whereas the size of low-angle grains changes slightly from their original size. In a steady-state condition the low-angle boundary grains remain almost constant in size and equiaxed. The low-angle grain boundaries are not permanent, but migrate, reform and decompose (McQueen and Poschmann, 1997).

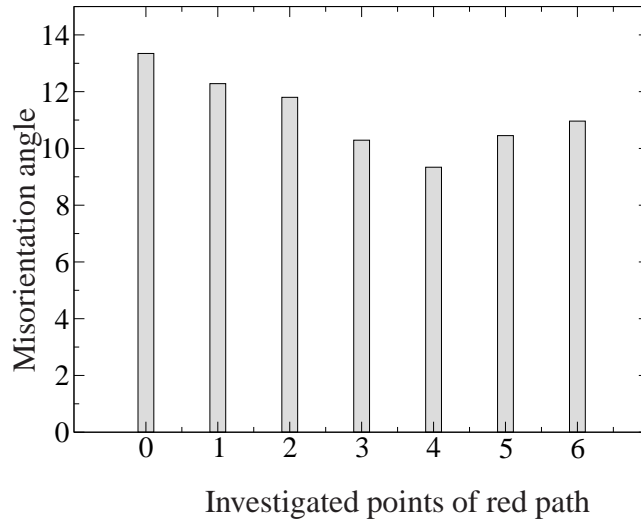


Figure 4.12: The mean low-angle boundary misorientation ( $<15^\circ$ ) of undeformed material and measured points of the red path in the billet obtained by the EBSD measurements.

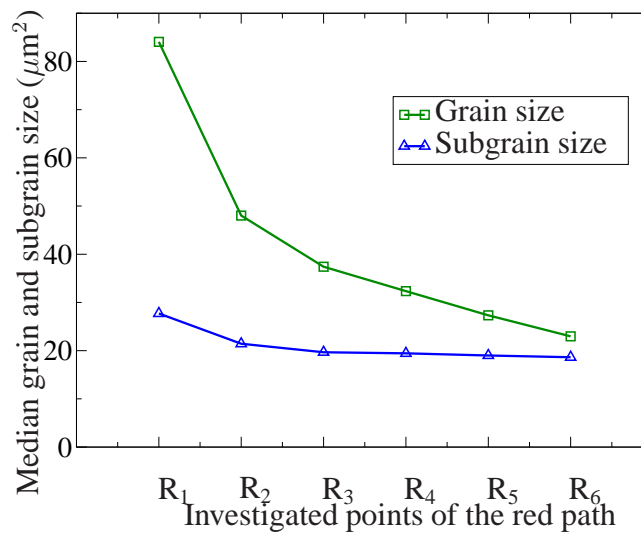


Figure 4.13: The median grain size measured points of the red path in the billet obtained by the EBSD measurements.

### 4.3 Material Model

Prediction of material behavior of metals during and after hot metal working processes requires the knowledge of microstructure parameters. The measurable microstructure parameters such as grain size, dislocation density and grain misorientation represent the state of the material behavior in micro scale. Energy gained from plastic deformation is mostly given off in form of heat energy and a small part of it is stored in the material by increasing the density of dislocations and consequently, the total length of grain boundaries (Humphreys and Hatherly, 2004). Evolution of microstructure properties during hot deformation of aluminum alloys generally occurs in two stages: dynamic evolution during the forming process and static evolution during cooling process after the deformation. Grain growth occurs by migration of grain boundaries in



order to minimize the stored energy of boundaries. During this process the total length of the boundary size decreases and the average grain size increases. Physically-based approaches for modeling of static microstructure evolution are commonly based on minimization of the stored energy of plastic deformation by increasing the size of the grains. In works of Chen (Chen, 2002; Fan and Chen, 1997) phase field modeling is used to model the grain growth process. In aluminum alloy EN AW-6082 no dynamic recrystallization occurs during the extrusion process due to low hot worked dislocation densities (Doherty et al., 1997), and the increasing energy of plastic deformation causes the refinement of grains during the forming process. The models based on grain growth are not generally suitable to predict this grain refinement. Sellars and Zhu (2000) have presented a physically-based model which relates the microstructure evolution during the hot deformation to the state variables such as temperature and plastic deformation. The model presented in the current work is based on the saturation of microstructure parameters after reaching steady-state forming condition. Microstructure parameters are modeled as internal state variables, depending on the rate of plastic deformation and temperature. The following sections present this model and its application for simulation of microstructure development during the extrusion process.

From a phenomenological viewpoint, the behavior of polycrystalline aluminum alloys during technological processes like extrusion is fundamentally thermoelastic and viscoplastic in nature. For simplicity, we begin by assuming that the material behavior is isotropic. More generally, the distribution of grain orientation, grain size and grain shape will result in anisotropic behavior. For the time being, we assume that the high homologous temperatures involved result in a reduction of the strength of anisotropy due to these factors. In this case, the stress state in the material can be modeled via the thermoelastic Hooke form

$$\mathbf{K} = \kappa_0 \{ \text{tr}(\ln \mathbf{V}_E) + 3 \alpha_0 (\theta_0 - \theta) \} \mathbf{I} + 2 \mu_0 \text{dev}(\ln \mathbf{V}_E) \quad (4.3)$$

for the Kirchhoff stress  $\mathbf{K}$  in terms of the elastic left logarithmic stretch  $\ln \mathbf{V}_E$ . Here,  $\kappa_0$  represents the elastic bulk modulus,  $\mu_0$  the elastic shear moduli and  $\alpha_0$  the thermal expansion, all at the reference temperature  $\theta_0$ . In addition,  $\theta$  is the absolute temperature. Further,  $\text{dev}(\mathbf{A}) := \mathbf{A} - \frac{1}{3} \text{tr}(\mathbf{A}) \mathbf{I}$  is the deviatoric part of  $\mathbf{A}$ . Neglecting any deformation-dependent damage and assuming inelastically incompressible von Mises flow, the evolution of  $\ln \mathbf{V}_E$  is given by the (objective) associated flow rule

$$- \dot{\ln \mathbf{V}_E} := \frac{1}{2} \ln(\mathbf{F} \overline{\mathbf{C}_P^{-1}} \mathbf{F}^T) = \dot{\alpha}_P \partial_{\mathbf{K}} \sigma_{vM} \quad (4.4)$$

in terms of the inelastic right Cauchy-Green deformation  $\mathbf{C}_P$  and accumulated equivalent inelastic deformation  $\alpha_P$ . Here,  $\sigma_{vM} = \sqrt{3} |\text{dev}(\mathbf{K})| / \sqrt{2}$  is the von Mises effective stress measure determined by the Kirchhoff stress. In the current thermodynamic approach, this determines the evolution of  $\alpha_P$  via the Zener-Hollomon form

$$\sigma_{vM} = \sigma_0 \sinh^{-1} \left( z^{1/n_0} / z_0^{1/n_0} \right) \quad (4.5)$$

(Sellars and Zhu, 2000) in terms of the Zener-Hollomon parameter  $z := \dot{\alpha}_P \exp(g_0/k\theta)$ . The evolution of  $\alpha_P$  drives in turn that of the (non-dimensional) dislocation density  $\nu := \sqrt{\rho} / \sqrt{\rho_{\text{sat}}}$  via the experimentally-established Voce form  $\dot{\nu} = c_\nu (1 - \nu) \dot{\alpha}_P$ , where  $\rho_{\text{sat}}$  represents the

saturation value of  $\rho$ . In this case,  $\nu$  varies between 0 and 1 at a rate determined by  $c_\nu \dot{\alpha}_P$ . Likewise, the development of the (non-dimensional) subgrain size  $\delta := d/d_{\text{sat}}$  is given by the experimentally-established (Sellars and Zhu, 2000) Holt relation

$$\dot{\delta} = c_\delta \delta (1 - \delta) \dot{\alpha}_P, \quad (4.6)$$

where  $d_{\text{sat}}$  is the saturation value. On this basis,  $\delta$  decreases from its initial value  $\delta(0) > 1$  to 1 at a rate determined by  $c_\delta \dot{\alpha}_P$ . A more detailed explanation of this material model can be found in previous chapter.

#### 4.4 Simulation of microstructure evolution

For simulation of microstructure evolution during the extrusion process the commercial Finite Element software Abaqus is applied. Because of the axisymmetric geometry of the billet, the extrusion process is idealized as axisymmetric in the simulation. The die and tool are modeled as deformable bodies with thermoelastic behavior and are meshed with quadrilateral elements. During the extrusion process several thermomechanical phenomena are involved: the energy of plastic deformation is mainly converted to the heat, friction between the material and container's wall generates heat which increases the temperature of both the billet and the container, and the heat transfers inside the billet and between the billet and the container's wall. A fully coupled temperature-deformation process is required to cover all of these thermomechanical aspects of the extrusion process which influence the material behavior and microstructure evolution. The element type CAX4RT which includes temperature as one degree of freedom is applied for the simulation. Element distortion and contact during the simulation of large deformation processes are controlled by means of a custom adaptive remeshing system based on Python scripting and utilized in the FE software Abaqus. Only the billet which undergoes large deformation needs to be remeshed. Abaqus enables us to use the user defined subroutines for material and microstructure modeling and is therefore more flexible for the simulation of microstructure compared to high-end FE software. The developed remeshing scheme has been optimized for large deformation processes so that the number of remeshing steps is decreased by checking the mesh quality after each increment. The remeshing is applied only when the mesh quality reaches a critical value and therefore loss of the information due to the mapping is minimized.

The contact simulation in this work is based on surface-to-surface contact which represents a more physical contact condition compared to the node-to-surface contact algorithm. For simulation of friction an isotropic Coulomb–Orowan (Wriggers, 2006) friction model is used. The classical Coulomb friction model assumes that no relative motion between the contact surfaces occurs if the frictional stress  $\tau_f$  is less than the critical stress  $\tau_c$  which is related to the normal pressure. In some hot metal forming processes such as extrusion, the material sticks to the container walls and the classical Coulomb model overestimates the frictional stresses in this case. To model this frictional condition, the friction stress is limited to the maximum shear stress  $\tau_{\text{max}}$  which material can undergo before sliding. The heat generated by friction is divided equally to the interacting surfaces. The thermal contact between all interacting surfaces is taken into account.

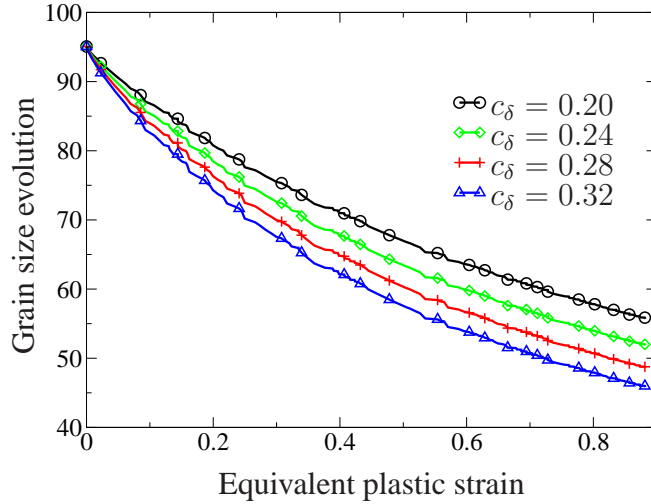


Figure 4.14: Evolution of grain size at point 2 for different values of  $c_\delta$ .

The material model explained in section 4.3 is implemented in Abaqus as a user defined material (UMAT). Parameter values used for simulation of EN AW-6082 in the current work are listed in Table 4.1.

$\kappa_0$	$\mu_0$	$\alpha_0$	$\theta_0$	$\sigma_0$	$g_0/k$
70 GPa	20.5 GPa	$2.3 \times 10^{-5} / \text{K}$	673 K	25 MPa	$1.8 \times 10^4 \text{ K}$
$n_0$	$z_0$	$\beta_0$	$\delta(0)$	$c_\delta$	
4.27	$3.3 \times 10^8 / \text{s}$	0.9	5.3426	0.2504	

Table 4.1: Material parameters of the aluminum alloy EN AW-6082 used for simulation of extrusion process.

In addition, for the temperature equation, we require the value of the coefficient of thermal conductivity  $k_0 = 210 \text{ J / m K}$  for the Fourier model, as well as that  $c_0 = 2.376 \text{ J / m}^3 \text{ K s}$  of the heat capacity. In addition, the rate of heating is given by  $\omega = \beta_0 \sigma_{\text{vM}} \dot{\alpha}_{\text{P}} - 3 \kappa_0 \alpha_0 \theta \text{tr}(\mathbf{D})$  in terms of the continuum rate of deformation  $\mathbf{D}$  via the Taylor-Quinney approximation and Taylor-Quinney coefficient  $\beta_0$ . In the current work,  $\beta_0 = 0.9$  is assumed. It has been shown in Rosakis et al. (2000) that  $\beta_0$  is in fact not a constant but rather depends on strain and strain-rate to varying degrees. In the following, this coefficient will be treated as constant as there is no experimental data relevant to the determination of  $\beta_0$  for the materials of interest here. The parameters for evolution of microstructure are determined by tuning. Figure 4.14 depicts the evolution of grain size at point 2 for different values of  $c_\delta$ . The values of equivalent plastic strain in Figure 4.14 are obtained from simulation results at point 2 (P<sub>2</sub> in Figure 4.4). With increasing  $c_\delta$ , the rate of evolution of grain size increases.

Figure 4.15 depicts the distribution of equivalent plastic deformation during simulation of the extrusion process. It can be seen that the material undergoes larger plastic deformations in the main deformation zone and die exit area compared to the dead material zone (DMZ). The highest value of plastic deformation occurs at the surface of the extruded profile where

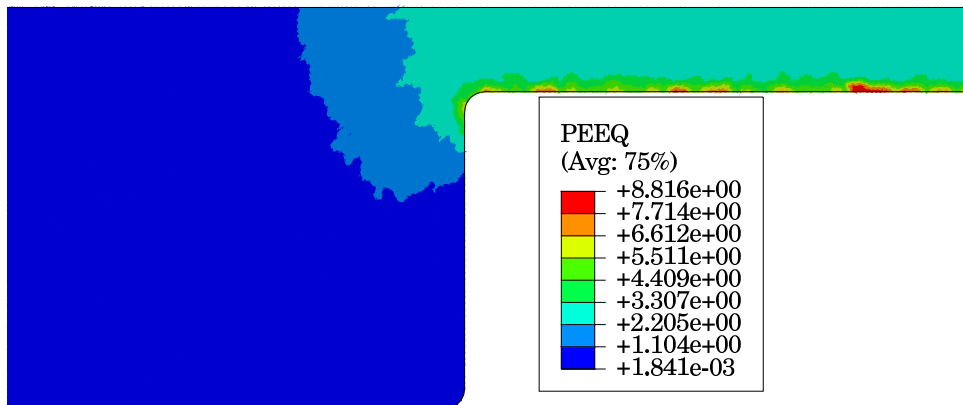


Figure 4.15: Simulated distribution of equivalent plastic strain in the billet at the end of the extrusion process.

material should overcome the frictional resistance of the die's surface. Figure 4.16 illustrates the simulated distribution of the temperature during the extrusion process. In the DMZ and die exit area an increase in temperature caused by the heat generated by large plastic deformation and frictional interaction becomes evident. The temperature decreases in areas close to the container due to heat transfer from the billet to the walls with lower temperature. Temperature at the die exit increases significantly compared to the initial temperature. In some experiments the die exit temperature was almost 100 K above the billet insert temperature (McQueen and Celliers, 1996, 1997).

Figure 4.17 shows the simulated distribution of the grain size in the material block at the end of the process. In the DMZ the grain size is the same as the original grain size which is in agreement with experimental observations. The grain size decreases in the shear zone along the direction of extrusion. The finest grains are at the surface of the extruded profile. In this area the grain boundary length and the dislocation density are higher than elsewhere. The high amount of dislocation density and stored energy of plastic deformation in this area provide the required energy for static recrystallization and grain growth in the cooling process. Experimental results show that the static recrystallization mainly occurs at the die corner and outer surface (Duan and Sheppard, 2004) and results in a bigger grain size in this area.

Table 4.2 represents the comparison between experimental and simulated values of grain size in the six investigated points of the black path. The red path is used for identification of microstructure parameters in the described model. The results of all points are in good agreement with the experiment. The major deviation is at point 6 which is mainly due to the modified form of the corner of the die in the simulation. The sharp corner of the die was slightly rounded in the simulation in order to reduce the numerical costs and efforts. The material faces

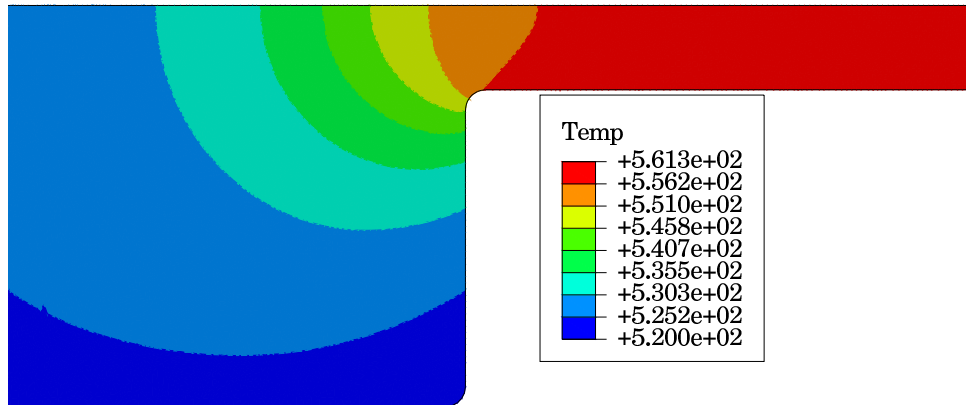


Figure 4.16: Simulated distribution of temperature ( $^{\circ}\text{C}$ ) in the billet during extrusion process.

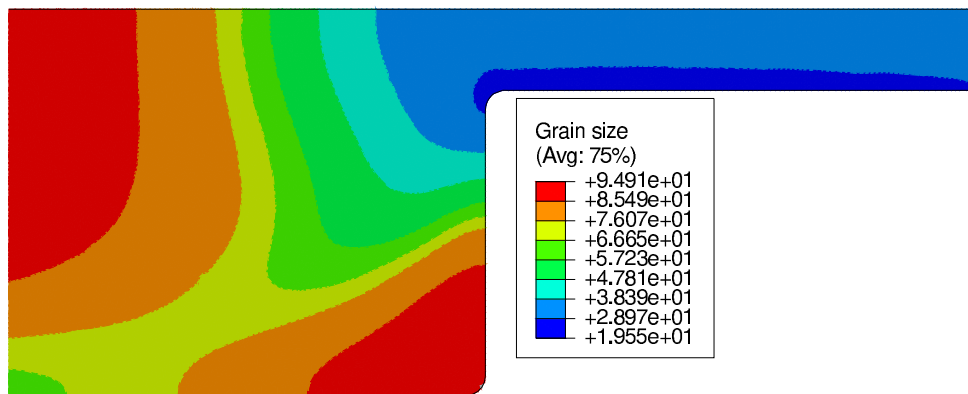


Figure 4.17: Simulated distribution of grain size ( $\mu\text{m}$ ) in the aluminum billet at the end of the extrusion process.

less resistance and deformation in this area compared to the sharp corner of the die in the experiment, and therefore the simulated grain size for point 6 is larger than the experimental observation.

To verify the model, the obtained parameters for the black path are used to predict the evolution of grain size of the points along the red path. The comparison of the simulated results

for the investigated points of the red path and experimental results is given in Table 4.3. The comparison shows that the predicted grain sizes of the points along the red path are close to the experimental one.

Table 4.2: Comparison between experimental and simulated results for grain size ( $\mu\text{m}$ ) at six investigated points of the black path.

Points	1	2	3	4	5	6
Experiment	52.1	54.6	33.2	30.8	26.4	17.8
Simulation	56.3	53.2	35.1	28.7	27.3	19.7
Difference	8%	3%	6%	7%	3%	10%

Table 4.3: Comparison between experimental and simulated results for grain size ( $\mu\text{m}$ ) at six investigated points of the red path.

Points	1	2	3	4	5	6
Experiment	84.1	48.1	36.4	34.3	29.3	21.9
Simulation	79.4	49.5	39.7	30.7	27.2	23.7
Difference	6%	3%	9%	10%	7%	8%

## 4.5 Results and discussion

In this chapter a model for the dynamic evolution of microstructure during hot forming processes of aluminum alloy EN AW-6082 is presented. To verify the model and simulation results, a small-scale extrusion process for scientific purposes was established. In this setup the material block and container were cooled down immediately after the extrusion in a water bath to prevent the statistic microstructure evolution. The EBSD results show that the microstructure map of the deformed material during the extrusion process was preserved by immediate cooling.

The physically-based model for modeling the microstructure as internal state dependent variables presented in this work assumes the saturation of the microstructure parameters such as grain size and dislocation density after reaching the steady-state condition. The model was implemented in combination with a thermo-elastic visco-plastic material model for a thermomechanically coupled simulation of the forming process. The size of the grains generally decreases in direction of the material flow line. The misorientation between low-angle boundary grains ( $5^\circ$ ) first decreases along the deformation line and then increases. This can be explained by the GDRX phenomena. The subgrains in serrated grains start to form new grains and therefore the misorientation between low-angle boundary grains increases. During this process the size of the low-angle boundary grains does not change significantly and the decreasing tendency of grain size along material flow line is not affected. The simulation results for evolution of grain size are in good agreement with experimental results and the model presented here can be used for further development and investigation of microstructure evolution during the hot forming processes of aluminum alloy EN AW-6082.

## Chapter 5

# Comparison of two models for material behavior of Al-alloys during thermo-mechanical processing

**abstract** In the current work, two models are formulated for the thermoelastic, viscoplastic behavior of aluminum alloys and applied to the case of extrusion. The first model is based on a common semi-empirical form of the (scalar) flow rule in the extrusion community and neglects all effects of the microstructure on the hardening behavior. This results in an ideal viscoplastic model. The second model formulates a scalar flow rule as based on the Taylor assumption and the effect of the subgrain structure development on the inelastic free energy and the flow stress is taken into account. The predictions of both of these models for simple benchmark problems involving material testing and extrusion are compared.

### 5.1 Introduction

During industrial thermo-mechanical processing such as hot forging, rolling or extrusion, processing conditions drive an evolution of the dislocation and grain microstructures in the metallic materials of interest, resulting in a change of shape of the work piece. In the case of high stacking-fault energy materials such as aluminum alloys, for example, mobile dislocations glide, cross-slip, and at higher temperatures, climb. Depending on the nature of the energetic and dissipative-kinetic mechanisms involved, dislocation motion results in the development of dislocation microstructures within existing grains consisting of dislocation-rich wall-like regions separating dislocation-poor cell-like regions, leading to subgrain formation.

Dislocations interacting with obstacles such as other dislocations, solutes, or precipitates, subgrain- or grain boundaries, result in various forms of hardening behavior. Face-center cubic (fcc) materials such as aluminum and its alloys are generally characterized by four stages of work hardening. Stage I (easy glide) represents the glide of dislocations over “long” distances, little interaction with other dislocations and little hardening. Stage II is characterized by a linear hardening rate and slight temperature-dependence. Stage III begins when cross slip of screw dislocations is activated. Especially at low temperatures, where climb is too slow, cross-slip is the major recovery mechanism. In general, both mechanisms will be important.

The interpretation of polycrystal hardening on the basis of single crystal behavior also involves the average grain size and the distribution of grain orientations, i.e. the texture. At least for pure fcc materials and for grain sizes much smaller than the specimen size, texture rather than grain size is important here in the sense that the distribution of grain orientations influences the distribution of active glide systems.

In the simplest case, one can view the microstructure of a polycrystal as consisting of (i) (high-angle) grain boundaries separating grains, (ii) (low-angle) subgrain boundaries separating subgrains within grains, (iii) dislocation walls separating cells within subgrains, (iv) individual dislocations, (v) solutes and (vi) precipitates.

From a phenomenological viewpoint, the behavior of polycrystalline aluminum alloys during technological processes like extrusion is fundamentally thermoelastic and viscoplastic (i.e. rate-dependent) in nature.

## 5.2 Material model framework

The purpose of this section is to establish the continuum thermodynamic framework for the formulation of material models for single- or multiphase thermoelastic, viscoplastic behavior. For simplicity, we assume that the material behavior of each phase is isotropic. More generally, non-trivial distributions of grain orientation (i.e. texture), grain size, and grain shape, will result in anisotropic behavior. In the current work, however, this is neglected. In addition, for simplicity, attention is restricted here to the case of two (metallic) solid phases, for example, in the case of steels, these could be austenite and martensite. Or in the case of aluminum alloys, these could be (aluminum) matrix and precipitate.

In the current thermoelastic, viscoplastic context the deformation behavior of the material is modeled by the constitutive forms of the referential free energy density  $\psi$ , the flow potential  $\phi$  and the dissipation potential  $\chi$ . Rather than  $\chi$ , one can alternatively work its thermodynamic conjugate  $\varphi$ , i.e. the stress potential. Here,  $\chi$  represents the deformation field, and  $\nabla$  is the gradient operator with respect to the reference configuration of the material. The inelastic state of the material is characterized by an inelastic local deformation  $\mathbf{F}_P$ , an equivalent inelastic deformation  $\epsilon_P$  and a set  $\alpha_P$  of deformation-related internal variables (e.g. immobile dislocation density) assumed to contribute to energy storage and processes like hardening in the material. On this basis, modeling  $\mathbf{F}_P$  as a change of local reference configuration (Svendsen, 2001), the referential free energy density is modeled by the additive split

$$\psi(\theta, \mathbf{F}, \mathbf{F}_P, \alpha_P) = \psi_E(\theta, \ln \mathbf{V}_E) + \psi_P(\theta, \alpha_P) \quad (5.1)$$

into elastic  $\psi_E$  and inelastic

$$\psi_P(\theta, \alpha_P) = \epsilon_P(\alpha_P) - \theta \eta_P(\alpha_P) \quad (5.2)$$

parts, again in the case of isotropic behavior. Here,  $\ln \mathbf{V}_E := \frac{1}{2} \ln(\mathbf{B}_E)$  is the elastic left logarithmic stretch tensor,  $\mathbf{B}_E = \mathbf{F}_E \mathbf{F}_E^T = \mathbf{F} \mathbf{C}_P^{-1} \mathbf{F}^T$  represents the elastic left Cauchy-Green deformation,  $\mathbf{F}_E := \mathbf{F} \mathbf{F}_P^{-1}$  is the elastic part of  $\mathbf{F}$  and  $\mathbf{C}_P = \mathbf{F}_P^T \mathbf{F}_P$  represents the inelastic right Cauchy-Green deformation. In particular, (5.1) determines as usual the thermoelastic forms

$$\begin{aligned} \mathbf{K} &= \partial_{\mathbf{F}} \psi \mathbf{F}^T, \\ -\eta &= \partial_{\theta} \psi, \end{aligned} \quad (5.3)$$

for the Kirchhoff stress  $\mathbf{K}$  and the referential entropy density  $\eta$ .



In the current isotropic case,  $\psi_{\mathbf{E}}(\theta, \ln \mathbf{V}_{\mathbf{E}})$  is an isotropic function of  $\ln \mathbf{V}_{\mathbf{E}}$ . In addition to isotropy, we exploit the fact that the magnitude  $\text{mag}(\ln \mathbf{V}_{\mathbf{E}}) := \sqrt{\ln \mathbf{V}_{\mathbf{E}} \cdot \ln \mathbf{V}_{\mathbf{E}}}$  of  $\ln \mathbf{V}_{\mathbf{E}}$  remains small in the case of metals. This results in the form

$$\begin{aligned} \psi_{\mathbf{E}}(\theta, \ln \mathbf{V}_{\mathbf{E}}) &= \psi_{\mathbf{E}}(\theta, \mathbf{0}) + \zeta_{\mathbf{E}}(\theta) \text{tr}(\ln \mathbf{V}_{\mathbf{E}}) \\ &+ \frac{1}{2} \kappa_{\mathbf{E}}(\theta) \text{tr}(\ln \mathbf{V}_{\mathbf{E}})^2 + \mu_{\mathbf{E}}(\theta) \text{mag}(\text{dev}(\ln \mathbf{V}_{\mathbf{E}}))^2 \end{aligned} \quad (5.4)$$

to second-order in terms of the thermal expansion modulus  $\zeta_{\mathbf{E}}(\theta)$ , the bulk modulus  $\kappa_{\mathbf{E}}(\theta)$ , and the shear modulus  $\mu_{\mathbf{E}}(\theta)$ . Here,  $\text{tr}(\ln \mathbf{V}_{\mathbf{E}}) := \mathbf{I} \cdot \ln \mathbf{V}_{\mathbf{E}}$  represents the trace, and  $\text{dev}(\ln \mathbf{V}_{\mathbf{E}}) := \ln \mathbf{V}_{\mathbf{E}} - \frac{1}{3} \text{tr}(\ln \mathbf{V}_{\mathbf{E}}) \mathbf{I}$  the deviatoric part, of  $\ln \mathbf{V}_{\mathbf{E}}$ . In particular, (5.4) implies the form

$$\begin{aligned} \mathbf{K} &= \partial_{\ln \mathbf{V}_{\mathbf{E}}} \psi_{\mathbf{E}} \\ &= \{\zeta_{\mathbf{E}} + \kappa_{\mathbf{E}} \text{tr}(\ln \mathbf{V}_{\mathbf{E}})\} \mathbf{I} + 2 \mu_{\mathbf{E}} \text{dev}(\ln \mathbf{V}_{\mathbf{E}}) \end{aligned} \quad (5.5)$$

for the Kirchhoff stress. Assume that there exists a reference temperature  $\theta = \theta_0$  at which the material is stress-free, i.e.  $\mathbf{K}(\theta_0, \mathbf{0}) = \mathbf{0}$ . In this case,  $\zeta_{\mathbf{E}}(\theta_0) = 0$  must hold. This results in the form  $\zeta_{\mathbf{E}}(\theta) = 3 \kappa_{\mathbf{E}}(\theta) \alpha_0 (\theta - \theta_0)$  of  $\zeta_{\mathbf{E}}(\theta)$  for  $\zeta_{\mathbf{E}}(\theta)$  in terms of the coefficient of thermal expansion  $\alpha_0$  at  $\theta_0$ . Assuming that  $\kappa_{\mathbf{E}}(\theta) = \kappa_0 + \kappa_1 (\theta - \theta_0)$  and  $\mu_{\mathbf{E}}(\theta) = \mu_0 + \mu_1 (\theta - \theta_0)$  are linear functions of temperature, the heat capacity

$$\begin{aligned} c_{\mathbf{E}}(\theta, \ln \mathbf{V}_{\mathbf{E}}) &= -\theta \partial_{\theta} \partial_{\theta} \psi_{\mathbf{E}}(\theta, \ln \mathbf{V}_{\mathbf{E}}) \\ &= c_0 + 6 \kappa_1 \alpha_0 \theta \text{tr}(\ln \mathbf{V}_{\mathbf{E}}) \end{aligned} \quad (5.6)$$

is independent of  $\mu_{\mathbf{E}}(\theta)$ . Here,  $c_0 = c_{\mathbf{E}}(\theta, \mathbf{0})$ . Since  $\text{mag}(\ln \mathbf{V}_{\mathbf{E}}) \ll 1$ , the second term in (5.6) is small. This is also reasonable from the point of view that we assume temperature variations about  $\theta_0$  to be “small”. In any case, (5.6) implies

$$\psi_{\mathbf{E}}(\theta, \mathbf{0}) = c_0 \{\theta - \theta_0 - \theta \ln(\theta/\theta_0)\} \quad (5.7)$$

and so

$$\begin{aligned} \psi_{\mathbf{E}}(\theta, l_{\mathbf{H}}, l_{\mathbf{D}}) &= \frac{1}{2} \kappa_{\mathbf{E}}(\theta) l_{\mathbf{H}}^2 + \mu_{\mathbf{E}}(\theta) l_{\mathbf{D}}^2 \\ &+ 3 \kappa_{\mathbf{E}}(\theta) \alpha_0 (\theta_0 - \theta) l_{\mathbf{H}} \\ &+ c_0 \{\theta - \theta_0 - \theta \ln(\theta/\theta_0)\} \end{aligned} \quad (5.8)$$

follows from (5.4) in terms of the scalar elastic strain measures

$$\begin{aligned} l_{\mathbf{H}} &:= \text{tr}(\ln \mathbf{V}_{\mathbf{E}}), \\ l_{\mathbf{D}} &:= \text{mag}(\text{dev}(\ln \mathbf{V}_{\mathbf{E}})), \end{aligned} \quad (5.9)$$

derived from  $\ln \mathbf{V}_{\mathbf{E}}$ , such that  $\ln \mathbf{V}_{\mathbf{E}} = \frac{1}{3} l_{\mathbf{H}} \mathbf{I} + l_{\mathbf{D}} \text{dir}(\text{dev}(\ln \mathbf{V}_{\mathbf{E}}))$  holds. Here,  $\text{dir}(\mathbf{A}) := \mathbf{A}/\text{mag}(\mathbf{A})$  is the direction of any non-zero tensor  $\mathbf{A}$ . From (5.8), we obtain the forms

$$\begin{aligned} -\eta_{\mathbf{E}}(\theta, l_{\mathbf{H}}, l_{\mathbf{D}}) &= \partial_{\theta} \psi_{\mathbf{E}}(\theta, l_{\mathbf{H}}, l_{\mathbf{D}}) \\ &= \frac{1}{2} \kappa_1 l_{\mathbf{H}}^2 + \mu_1 l_{\mathbf{D}}^2 \\ &- 3(\kappa_{\mathbf{E}}(\theta) + \kappa_1 (\theta - \theta_0)) \alpha_0 l_{\mathbf{H}} - c_0 \ln(\theta/\theta_0), \\ \varepsilon_{\mathbf{E}}(\theta, l_{\mathbf{H}}, l_{\mathbf{D}}) &= \psi_{\mathbf{E}}(\theta, l_{\mathbf{H}}, l_{\mathbf{D}}) + \theta \eta_{\mathbf{E}}(\theta, l_{\mathbf{H}}, l_{\mathbf{D}}) \\ &= \frac{1}{2} (\kappa_0 - \kappa_1 \theta_0) l_{\mathbf{H}}^2 + (\mu_0 - \mu_1 \theta_0) l_{\mathbf{D}}^2 \\ &+ c_0 (\theta - \theta_0) + 3(\kappa_{\mathbf{E}}(\theta) + \kappa_1 (\theta - \theta_0)) \alpha_0 l_{\mathbf{H}}, \end{aligned} \quad (5.10)$$

for the corresponding entropy and internal energy densities, respectively, via (5.3)<sub>2</sub>. Combining (5.8) with (5.1), we then have

$$\psi(\theta, \mathbf{F}, \mathbf{F}_{\mathbf{P}}, \boldsymbol{\alpha}_{\mathbf{P}}) = \psi_{\mathbf{E}}(\theta, l_{\mathbf{H}}, l_{\mathbf{D}}) + \psi_{\mathbf{P}}(\theta, \boldsymbol{\alpha}_{\mathbf{P}}) \quad (5.11)$$

for the free energy density. In turn, this form for the free energy density implies that

$$\mathbf{K} = \partial_{\ln \mathbf{V}_E} \psi = k_H \mathbf{I} + k_D \operatorname{dir}(\operatorname{dev}(\ln \mathbf{V}_E)) \quad (5.12)$$

for the Kirchhoff stress  $\mathbf{K}$ , with

$$\begin{aligned} k_H &:= \frac{1}{3} \operatorname{tr}(\mathbf{K}) &= \partial_{l_H} \psi &= \kappa_E \{l_H + 3\alpha_0(\theta_0 - \theta)\}, \\ k_D &:= \operatorname{mag}(\operatorname{dev}(\mathbf{K})) &= \partial_{l_D} \psi &= 2\mu_E l_D, \end{aligned} \quad (5.13)$$

its scalar hydrostatic and deviatoric parts, respectively. In the current model class, then,  $(k_H, l_H)$  and  $(k_D, l_D)$  are thermodynamic conjugates.

Consider next the inelastic constitutive relations. Following standard metal plasticity, assume that dislocation glide is driven by deviatoric stress  $k_D$  alone. Again, damage or any related inelastic processes resulting in inelastic volume changes are neglected here. In this context, we work with the constitutive relations

$$\begin{aligned} \dot{\mathbf{F}}_P &= \dot{\epsilon}_P \mathbf{N}_{Pi} \mathbf{F}_P, \\ \dot{\alpha}_i &= c_i |\dot{\epsilon}_P| - r_i, \end{aligned} \quad (5.14)$$

for the tensorial flow rule and for each  $\alpha_i \in \boldsymbol{\alpha}_P$ , respectively. In particular, the latter takes the generalized Voce form, with the first term representing inelastic-deformation-driven growth and recovery and the second term representing non-deformation-related recovery processes. On the basis of these and (5.3), one obtains the result

$$\delta_I = |\sigma_P| |\dot{\epsilon}_P| + \sum_i \partial_{\alpha_i} \psi_P r_i \quad (5.15)$$

for the internal part  $\delta_I$  of the referential dissipation-rate density in terms of the conjugate stress

$$\sigma_P := \left\{ |\mathbf{K} \cdot \mathbf{N}_{Pc}| - \sum_i \partial_{\alpha_i} \psi_P c_i \right\} \operatorname{sgn}(\mathbf{K} \cdot \mathbf{N}_{Pc}) \quad (5.16)$$

to  $\epsilon_P$  via the constitutive assumption

$$\operatorname{sgn}(\dot{\epsilon}_P) \equiv \operatorname{sgn}(\mathbf{K} \cdot \mathbf{N}_{Pc}) \quad (5.17)$$

on the sign of  $\dot{\epsilon}_P$ . Here,  $\mathbf{N}_{Pc} := \mathbf{F}_E \mathbf{N}_{Pi} \mathbf{F}_E^{-1}$ . In particular, assuming the von Mises flow, we have

$$\phi_P(\dots, k_D) := k_M = \sqrt{\frac{3}{2}} k_D = \sqrt{6} \mu_E l_D \quad (5.18)$$

for the inelastic flow potential, and so

$$\mathbf{N}_{Pc} = \partial_{\mathbf{K}} \phi_P = \sqrt{\frac{3}{2}} \operatorname{dir}(\operatorname{dev}(\mathbf{K})) \quad (5.19)$$

for the corresponding flow direction. Then  $\mathbf{K} \cdot \mathbf{N}_{Pc} = k_M \geq 0$  is always non-negative, in which case  $\operatorname{sgn}(\dot{\epsilon}_P) = 1$  is always positive for non-zero  $\dot{\epsilon}_P$ . As such,  $\sigma_P = |\sigma_P|$  and  $\dot{\epsilon}_P = |\dot{\epsilon}_P|$  are always positive as well. Substituting these into (5.15) then yields

$$\delta_I = \sigma_P \dot{\epsilon}_P + \sum_i \partial_{\alpha_i} \psi_P r_i, \quad (5.20)$$

with now

$$\sigma_P = k_M - \sum_i \partial_{\alpha_i} \psi_P c_i. \quad (5.21)$$

In terms of the conjugate constitutive relations

$$\begin{aligned}\sigma_{\text{P}} &= \partial_{\dot{\epsilon}_{\text{P}}} \chi_{\text{P}}, \\ \dot{\epsilon}_{\text{P}} &= \partial_{\sigma_{\text{P}}} \varphi_{\text{P}},\end{aligned}\tag{5.22}$$

we have

$$\begin{aligned}\delta_{\text{I}} &= \partial_{\dot{\epsilon}_{\text{P}}} \chi_{\text{P}} \dot{\epsilon}_{\text{P}} + \sum_i \partial_{\alpha_i} \psi_{\text{P}} r_i \\ &= \sigma_{\text{P}} \partial_{\sigma_{\text{P}}} \varphi_{\text{P}} + \sum_i \partial_{\alpha_i} \psi_{\text{P}} r_i\end{aligned}\tag{5.23}$$

for  $\delta_{\text{I}}$ , in terms of the inelastic contribution  $\chi_{\text{P}}(\dots, \dot{\epsilon}_{\text{P}})$  to the dissipation potential, with  $\varphi_{\text{P}}(\dots, \sigma_{\text{P}})$  the conjugate driving stress potential.

Assuming quasi-static conditions, the deformation field  $\chi$  is determined as usual via the corresponding form

$$\text{div}(\mathbf{K} \mathbf{F}^{-\text{T}}) = \mathbf{0}\tag{5.24}$$

of momentum balance. Analogously, in the current Clausius-Duhem context, the field relation

$$c_{\text{E}} \dot{\theta} = \omega_{\text{E}} + \omega_{\text{P}} + \text{div}(\theta \partial_{\nabla \theta} \chi_{\text{C}})\tag{5.25}$$

for the temperature  $\theta$  is obtained. Here,

$$\begin{aligned}\omega_{\text{E}} &:= \mathbf{K}_{\eta} \cdot \mathbf{D}, \\ \omega_{\text{P}} &:= \sigma_{\text{P}\varepsilon} \dot{\epsilon}_{\text{P}} + \sum_i \partial_{\alpha_i} \varepsilon_{\text{P}} r_i,\end{aligned}\tag{5.26}$$

represent the elastic and inelastic rates of heating, respectively. In these relations,

$$\mathbf{K}_{\eta} = -\theta \partial_{\ln \mathbf{V}_{\text{E}}} \eta_{\text{E}}\tag{5.27}$$

represents the entropic part of  $\mathbf{K}$ , and

$$\sigma_{\text{P}\varepsilon} := \mathbf{K}_{\varepsilon} \cdot \mathbf{N}_{\text{Pc}} - \sum_i \partial_{\alpha_i} \varepsilon_{\text{P}} c_i\tag{5.28}$$

is the energetic part of  $\sigma_{\text{P}}$  as determined by that

$$\mathbf{K}_{\varepsilon} = \partial_{\ln \mathbf{V}_{\text{E}}} \varepsilon_{\text{E}}\tag{5.29}$$

of  $\mathbf{K}$ . Lastly, heat conduction is determined by the corresponding part

$$\chi_{\text{C}}(\theta, \mathbf{F}, \nabla \theta) = \frac{1}{2} \theta^{-1} k_0 \mathbf{F}^{-\text{T}} \nabla \theta \cdot \det(\mathbf{F}) \mathbf{F}^{-\text{T}} \nabla \theta\tag{5.30}$$

of the total dissipation potential  $\chi$ . The form of  $\chi_{\text{C}}$  is based on Fourier heat conduction, with  $k_0$  being the coefficient of thermal conductivity.

In summary, particular forms of the material model are obtained via specification of (i) the temperature-dependence of  $\kappa_{\text{E}}(\theta)$  and  $\mu_{\text{E}}(\theta)$  in (5.8), (ii) the forms  $\varepsilon_{\text{P}}(\alpha_{\text{P}})$  and  $\eta_{\text{P}}(\alpha_{\text{P}})$  in (5.2), and (iii) the form of either  $\chi_{\text{P}}$  or  $\varphi_{\text{P}}$ . On this basis, we now apply this approach to the high-temperature extrusion of aluminum alloys.

### 5.3 First simple model

If the material (e.g. aluminum alloy) under consideration is in a strain- and stress-free state at room temperature, it will not be so after placing it in the extrusion device and heating it up to approximately 673~773 K. Indeed, the resulting thermal expansion of the material and a reduction in the elastic properties will affect the stress state in general. On the other hand, if given enough time before loading begins, local inelastic processes in the material will relax any significant local stress build-up. On this basis, we assume  $\mathbf{K}(\theta = \theta_0, \mathbf{0}) = \mathbf{0}$ , with  $\theta_0$  chosen to be the initial temperature of the extrusion process. During this process, the temperature varies due to for example mechanical dissipation, friction of the block with the walls of the extrusion device and heat conduction. Generally speaking, the former two result in a temperature increase and the latter in a temperature decrease, near  $\theta_0$ . Assuming this temperature variation is not large,  $\kappa_E(\theta) \approx \kappa_0$  and  $\mu_E(\theta) \approx \mu_0$  in (5.8) can be assumed to be approximately constant.

The high stacking-fault energy of materials like aluminum alloys implies that, at high homologous temperatures, dislocation-based dynamic recovery leading to subgrain development and “geometric” continuous dynamic recrystallization are energetically favored. As such, inelastic deformation in such materials is modeled as a transition-state process via corresponding activation-based constitutive forms like

$$\dot{\epsilon}_P = \partial_{\sigma_P} \varphi_P = \dot{\epsilon}_{P0} e^{g_0/k\theta_0} \sinh^{n_0}(\langle \sigma_P - \sigma_A \rangle / \sigma_D) e^{-g_0/k\theta} \quad (5.31)$$

for the flow rule (5.22)<sub>2</sub> (c.f., Sellars and Zhu, 2000; Sheppard, 2006). Here,  $\sigma_A$  represents the initial activation stress for dislocation motion (i.e. initial yield stress),  $\sigma_D$  is the drag or Peierls stress on moving dislocations,  $\langle f \rangle := (f + |f|)/2$  is the ramp function and  $n_0$  is the rate exponent. Note that (5.31) can be inverted to obtain

$$\sigma_P = \partial_{\dot{\epsilon}_P} \chi_P = \sigma_A + \sigma_D \sinh^{-1}(z_P^{1/n_0} / z_{P0}^{1/n_0}) \quad (5.32)$$

for the implicit form of the flow rule in terms of the so-called Zener-Hollomon “parameter”

$$z_P := \dot{\epsilon}_P \exp(g_0/k\theta), \quad (5.33)$$

with  $z_{P0} := \dot{\epsilon}_{P0} \exp(g_0/k\theta_0)$ . Formally, (5.31) and (5.32) can be integrated to yield the corresponding potential; for example, the latter yields

$$\chi_P = \sigma_A \dot{\epsilon}_P + \sigma_D \dot{\epsilon}_P f_P(z_P/z_{P0}), \quad (5.34)$$

with

$$\begin{aligned} f_P(\xi) &:= \sinh^{-1}(\xi^{1/n_0}) \\ &- \frac{1}{1+n_0} \xi^{1/n_0} {}_2F_1(1/2, (1+n_0)/2; (3+n_0)/2; -\xi^{2/n_0}), \end{aligned} \quad (5.35)$$

in terms of the hypergeometric function  ${}_2F_1(a, b; c; z)$  of the second kind. For simplicity, we begin by treating  $\sigma_A$  and  $\sigma_D$  as constant. In other words, any dissipative hardening is neglected. In addition, we neglect any energetic hardening. In this case,  $\varepsilon_P$ ,  $\eta_P$ , and so  $\psi_P$ , from (5.2) all vanish. In this case,  $\sigma_P$  from (5.21) reduces to  $\sigma_P = k_M$ . Likewise, one obtains the reduced form

$\omega_P = \sigma_{P\epsilon} \dot{\epsilon}_P$  for the inelastic rate of heating from (5.26)<sub>2</sub> depending on that  $\sigma_{P\epsilon} = \mathbf{K}_\epsilon \cdot \mathbf{N}_{P\epsilon}$  for  $\sigma_{P\epsilon}$  from (5.28).

Although we are neglecting their effect on the hardening behavior here, it is nevertheless instructive to examine the evolution of selected microstructural characteristics whose development is driven by that of  $\epsilon_P$ . For example, the mean (sub)grain size  $d$ . In particular, on the basis of dynamic recovery alone,  $d$  is observed to decrease with increasing  $\epsilon_P$ . This observation motivates the constitutive Holt-Voce form

$$\dot{d} = r_d d (s_d - d) \dot{\epsilon}_P \quad (5.36)$$

(e.g. Sellars and Zhu, 2000; Sheppard, 2006) for  $\dot{d}$ . Here,  $s_d := c_d/r_d$  represents the saturation value of  $d$ . For the simulation of the extrusion behavior of the aluminum alloy EN AW-6082, the values  $\theta_0 = 773$  K,  $\kappa_0 = 70$  GPa,  $\mu_0 = 20.5$  GPa,  $\alpha_0 = 2.3 \times 10^{-5}$  / K,  $c_0 = 2.376$  J / m<sup>3</sup> K s and  $k_0 = 237$  J / m K for the thermoelastic parameters have been assumed. For the flow rule,  $g_0/k\theta_0 = 23.2$ ,  $n_0 = 4.27$ ,  $\dot{\epsilon}_{P0} = 9 \times 10^{-4}$  / s,  $\sigma_A = 0$  MPa, and  $\sigma_D = 25.0$  MPa have been chosen. Lastly, for the evolution of  $d$ ,  $d(\epsilon_P = 0) = 5.3$   $\mu\text{m}$ ,  $r_d = 0.2$  /  $\mu\text{m}$ , and  $s_d = 1$   $\mu\text{m}$ , are used. These latter values have been estimated with the help of the statistical characterization of the grain microstructural development based on EBSD data (Parvizian et al., 2011).

The behavior predicted by this thermoelastic, ideal viscoplastic model is compared below with that of the second model considered in this work, to which we now turn.

## 5.4 Simple subgrain-based hardening model

The model examined in the previous section completely neglected the influence of the developing grain and dislocation microstructures on the behavior of the material during extrusion, and in particular on the hardening behavior. The purpose of this section is to formulate a first simple model in this direction for the case of aluminum alloys.

The simplest effective representation of the influence of the grain microstructure on the material behavior of a polycrystal is that due to Taylor. This is based on the Taylor factor  $m_T$  relating the equivalent inelastic deformation  $\gamma_p$  in each grain to the corresponding polycrystal quantity  $\epsilon_P$ , i.e.  $\gamma_p = m_T \epsilon_P$ .

For simplicity, we treat  $m_T$  as constant here; in reality, however, the grain microstructure, i.e. texture, and hence this factor, could change considerably during deformation. Since the magnitude or degree of anisotropy of aluminum alloys is quite low (in contrast to the case of copper for example), assuming  $m_T$  to be constant would therefore seem not unreasonable.

In fcc systems at low homologous temperatures, recovery is primarily due to cross-slip of screw dislocations. As the temperature increases, dislocation climb also contributes to recovery. For simplicity, no distinction is made between edge and screw dislocations here. The frequency of cross slip is affected among other things by the stacking fault energy. This energy is related to the atomic bonding in the material and determines the extent to which unit dislocations dissociate into partials. In particular, the higher this energy, the smaller the stacking fault and the less likely the dissociation becomes. Indeed, the smaller the stacking fault, the easier the climb and cross slip. In our model the dependency of the frequency of cross slip on the stacking fault en-

ergy is not explicitly treated. The model could clearly be improved by including a dependence on the stacking fault energy.

The model for each grain is based in particular on the Orowan relation

$$\dot{\gamma}_p = \varrho_m v_d / b \quad (5.37)$$

for each grain determining its equivalent inelastic deformation rate  $\dot{\gamma}_p$  in terms of the Burgers vector magnitude  $b$ , the non-dimensional mobile dislocation density  $\varrho_m := b^2 \rho_m$  and the mean dislocation velocity  $v_d$ . Under quasi-static loading conditions, the time  $t_i$  dislocations spend in the immobile state is generally much longer than the time  $t_m$  spent moving, i.e.  $t_i \gg t_m$ . In this case,

$$v_d = \lambda_o / (t_i + t_m) \approx \lambda_o / t_i \quad (5.38)$$

follows for  $v_d$  in terms of the mean obstacle spacing  $\lambda_o$  and  $t_i \gg t_m$ . Since mobilization is an activation process,  $t_i$  is modeled via the activation relation

$$\frac{1}{t_i} = \omega_0 \exp\left(\frac{g_0}{k\theta_0} - \frac{g_0}{k\theta}\right) \left\{ \exp\left(\frac{v_0}{k\theta} \langle \tau_t - \tau_0 \rangle\right) - 1 \right\} \quad (5.39)$$

with respect to the reference temperature  $\theta_0$  depending on the ‘‘mobilization’’ frequency  $\omega_0$ , the activation energy  $g_0$  for mobilization, the free volume  $v_0$ , Boltzmann’s constant  $k$ , and the (activation) Peierls stress  $\tau_0$  (i.e. resistance of the lattice to activation of dislocation motion) with respect to  $\theta_0$ . In pure metals,  $\tau_t$  is related to short-range interactions associated with cutting of ‘‘trees’’ and dragging of jogs. In alloys with a significant amount of atoms in solid solution (e.g. Al-Mg alloys), thermal activation of solute atom diffusion away from climbing jogs on screw dislocations influences this stress as well. In addition, cell and grain sizes, as well as any interactions with non-deformable particles such as precipitates, are influential as well.

Combination of (5.38) with (5.39) and substitution of the result into (5.37) yields the constitutive form

$$\tau_t = \tau_0 + \tau_d \ln\left(1 + \frac{z_p}{z_{p0}}\right) \quad (5.40)$$

for  $\tau_t$  as well as corresponding hardening rate

$$\partial_{\ln \dot{\gamma}_p} \tau_t = \tau_d \frac{z_p}{z_{p0} + z_p} \quad (5.41)$$

at the grain level. Here,

$$\tau_d := k\theta / v_0 = (k\theta_0 / v_0) \theta / \theta_0 = \tau_{d0} \theta / \theta_0 \quad (5.42)$$

represents the drag stress,

$$z_{p0} = \dot{\gamma}_{p0} e^{g_0 / k\theta_0} \quad (5.43)$$

is a reference Zener-Hollomon parameter, and

$$\dot{\gamma}_{p0} := \omega_0 (\lambda_o / b) \varrho_m \quad (5.44)$$

a reference deformation rate. In the current thermodynamic context, then, (5.40) is expressed in the potential form

$$\tau_t = \partial_{\dot{\gamma}_p} \chi_p \quad (5.45)$$

relative to the inelastic part

$$\chi_p = \tau_0 e^{-g_0/k\theta} z_p + \tau_d e^{-g_0/k\theta} z_{p0} \left\{ \left(1 + \frac{z_p}{z_{p0}}\right) \ln \left(1 + \frac{z_p}{z_{p0}}\right) - \frac{z_p}{z_{p0}} \right\} \quad (5.46)$$

of the dissipation potential at the grain level.

Consider next the driving stress

$$\tau_p = \tau_a + \tau_t = \tau_a + \partial_{\dot{\gamma}_p} \chi_p \quad (5.47)$$

for dislocation motion in each grain. As indicated, this splits into thermal  $\tau_t$  and athermal  $\tau_a$  parts. In particular, the latter is due to energetic and basically temperature-independent interactions with long-range barriers, while the dynamic or thermal stress component  $\tau_t$  characterizes the rate- and temperature-dependent interactions with short-range obstacles. For simplicity, we assume that the athermal stress  $\tau_a$  is dominated by the development of the subgrain structure as represented and idealized by the mean (sub)grain size  $d$ . As such, we have  $\alpha_p = \{\delta\}$  in the context of the thermodynamic material model framework discussed in section 5.2, with  $\delta := d/s_d$  the dimensionless subgrain size. As in the last section, the evolution-constitutive relation (5.36) for  $d$  holds here as well. This results in the form

$$\begin{aligned} \tau_t &:= -\partial_{\dot{\gamma}_p} \zeta_p \\ &= \tau_p - \tau_a \\ &= \tau_p - \partial_{\delta} \psi_p r_d s_d \delta (1 - \delta) \\ &= \tau_p - h_{\delta} \delta^{-1} \end{aligned} \quad (5.48)$$

for the flow rule at the grain level via the form

$$\psi_p(\delta) = \frac{h_{\delta}}{r_d s_d} \left\{ \ln \left( \frac{1 - 1/\delta_0}{1 - 1/\delta} \right) + \frac{1}{\delta_0} - \frac{1}{\delta} \right\} \quad (5.49)$$

for the inelastic stored energy associated with subgrain formation.

For the simulations to follow, the same thermoelastic parameter values are used for the aluminum alloy EN AW-6082 as given at the end of the last section. This holds as well for the parameter values for the evolution of the subgrain size  $d$ . For the current inelastic flow model, we choose  $g_0/k\theta_0 = 23.2$ ,  $\dot{\gamma}_{p0} = 9 \times 10^{-6} / \text{s}$ ,  $\tau_0 = 0$  MPa and  $\tau_{d0} = 3.0$  MPa for comparability with the parameter values from the last section. Likewise, as before, for the evolution of  $d$ , we assume  $d(\epsilon_p = 0) = 5.3 \mu\text{m}$ ,  $r_d = 0.2 / \mu\text{m}$ , and  $s_d = 1 \mu\text{m}$ . The Taylor factor  $m_T = 1$  is assumed to be constant here and the hardening parameter is assumed  $h_{\delta} = 12$  MPa for the extrusion process at the described conditions.

## 5.5 Algorithmic formulation

As usual, we consider an arbitrary time interval  $[t_n, t_{n+1}]$  with time-step size  $t_{n+1,n} := t_{n+1} - t_n$ . As usual, the  $\theta_n$ ,  $\mathbf{F}_n$ ,  $\epsilon_{p,n}$ ,  $\epsilon_{\rho,n}$ ,  $\epsilon_{\varphi,n}$ , and  $\epsilon_{\delta,n}$  at time  $t = t_n$  are known. In addition,  $\theta_{n+1}$  and  $\mathbf{F}_{n+1}$  are given. The current implementation is based on backward-Euler integration. This yields the system

$$\begin{aligned} l_{H_{n+1}} &= l_{H_{n+1}}^{\text{tr}}, \\ \text{dir}(\text{dev}(\ln \mathbf{V}_{E_{n+1}})) &= \text{dir}(\text{dev}(\ln \mathbf{V}_{E_{n+1}}^{\text{tr}})), \\ l_{D_{n+1}} + \sqrt{\frac{3}{2}} \epsilon_{p_{n+1,n}} &= l_{D_{n+1}}^{\text{tr}}. \end{aligned} \quad (5.50)$$

via (5.9). Here,  $\epsilon_{P_{n+1,n}} := \epsilon_{P_{n+1}} - \epsilon_{P_n}$ . Further,  $l_{H_{n+1}}^{\text{tr}}$  and  $l_{D_{n+1}}^{\text{tr}}$ , represent the so-called trial values of  $l_{H_{n+1}}$  and  $l_{D_{n+1}}$  determined by that

$$\ln \mathbf{V}_{E_{n+1}}^{\text{tr}} = \frac{1}{2} \ln(\mathbf{F}_{n+1} \mathbf{C}_{P_n}^{-1} \mathbf{F}_{n+1}^{\text{T}}) = \frac{1}{2} \ln(\mathbf{F}_{n+1,n} \mathbf{B}_{E_n} \mathbf{F}_{n+1,n}^{\text{T}}) \quad (5.51)$$

of the elastic left logarithmic stretch, where  $\mathbf{F}_{n+1,n} := \mathbf{F}_{n+1} \mathbf{F}_n^{-1}$  is the relative deformation gradient. In turn, (5.50) yields the algorithmic relations

$$\begin{aligned} k_{H_{n+1}} &= \kappa_0 \{l_{H_{n+1}}^{\text{tr}} + 3\alpha_0(\theta_0 - \theta_{n+1})\}, \\ k_{D_{n+1}} &= 2\mu_0 l_{D_{n+1}}^{\text{tr}} - \sqrt{6}\mu_0 \epsilon_{P_{n+1,n}}, \end{aligned} \quad (5.52)$$

for  $k_H$  and  $k_D$ , respectively, via (5.13). On the other hand, backward-Euler integration of (5.22)<sub>2</sub> yields the algorithmic relations

$$\begin{aligned} \text{if } \sigma_{P_{n+1}}^{\text{tr}} \leq \sigma_{\text{AP}} \quad \epsilon_{P_{n+1}} &= \epsilon_{P_n} \\ \text{else solve} \quad \sigma_{P_{n+1}} &= \sigma_{\text{AP}} + \sigma_{\text{DP}} \sinh^{-1} \left( \frac{z_{n+1}^{1/n_0}}{z_0^{1/n_0}} \right) \end{aligned} \quad (5.53)$$

in the usual predictor-corrector fashion via (5.32) to solve for  $\epsilon_{P_{n+1}}$ . Here,

$$\sigma_{P_{n+1}}^{\text{tr}} = \sigma_{\text{vM}_{n+1}}^{\text{tr}} - (\partial_{\epsilon_P} \psi)_n = \sqrt{\frac{3}{2}} k_{D_{n+1}}^{\text{tr}} - (\partial_{\epsilon_P} \psi)_n \quad (5.54)$$

represents the trial-predictor value of  $\sigma_{P_{n+1}}$  as usual from (5.52)<sub>2</sub>. In any case, this yields the updated  $\epsilon_{P_{n+1}}$  of the accumulated equivalent inelastic deformation.

In post-processing, the solution for  $\epsilon_{P_{n+1}}$  obtained in this way yields the forward-Euler updates

$$\begin{aligned} \epsilon_{\rho_{n+1}} &= \epsilon_{\rho_n} + c_\rho (1 - \epsilon_{\rho_n}) \epsilon_{P_{n+1,n}}, \\ \epsilon_{\varphi_{n+1}} &= \epsilon_{\varphi_n} + c_\varphi (1 - \epsilon_{\varphi_n}) \epsilon_{P_{n+1,n}}, \\ \epsilon_{\delta_{n+1}} &= \epsilon_{\delta_n} + c_\delta \epsilon_{\delta_n} (1 - \epsilon_{\delta_n}) \epsilon_{P_{n+1,n}} \end{aligned} \quad (5.55)$$

for the non-dimensional dislocation density, misorientation and subgrain size, respectively. In addition,  $k_{D_{n+1}}$  then follows from (5.52)<sub>2</sub>. Since  $\text{dir}(\text{dev}(\ln \mathbf{V}_{E_{n+1}}))$  and  $k_{H_{n+1}}$  are determined by the trial state via (5.50)<sub>2</sub> and (5.52)<sub>1</sub>, respectively,

$$\mathbf{K}_{n+1} = k_{H_{n+1}} \mathbf{I} + k_{D_{n+1}} \text{dir}(\text{dev}(\ln \mathbf{V}_{E_{n+1}})) \quad (5.56)$$

follows from (5.12). Likewise, the forward-Euler form

$$t_{n+1,n} \omega_{n+1} = \beta_P \sigma_{P_n} \epsilon_{P_{n+1,n}} - 3\kappa_0 \alpha_0 \theta_n \mathbf{I} \cdot \text{sym}(\mathbf{F}_{n+1,n} - \mathbf{I}) \quad (5.57)$$

for the rate of heating is obtained.

Similar to section 3.4, on the free surface, radiation is modeled by the normal heat flux boundary condition

$$q_c = \varepsilon_0 \varsigma_0 (\theta^4 - \theta_0^4) \quad (5.58)$$

for the normal component  $q_c$  of the current heat flux, where  $\varepsilon_0$  is the emissivity,  $\varsigma_0$  the Stefan constant and  $\theta_0$  the temperature of the surroundings. On the surface of contact with the tool, we have

$$q_c = h_0 (\theta - \theta_{\text{tool}}) + \frac{e_{\text{billet}}}{e_{\text{billet}} + e_{\text{tool}}} \mu_{f0} p |v|, \quad (5.59)$$

where  $h_0$  is the heat transfer coefficient between the billet and container at temperature  $\theta_{\text{tool}}$ ,  $\mu_{f0}$  represents the friction coefficient,  $e_{\text{billet}}$  and  $e_{\text{tool}}$  the respective effusivities,  $p$  is the contact pressure and  $v$  is the velocity jump across the billet-tool interface.



## 5.6 Results

The results of two explained models in previous sections are compared with the experimental results for the simple tension test published in Parvizian et al. (2011) as well as the experimental results of the extrusion process. The simple tension test is performed at three different temperatures (623, 673 and 723 K) and in each case for three different head velocities (0.1, 1.0 and 10.0 mm/s). Figure 5.1 shows the comparison of the results of the first model (no hardening) with the experimental results of EN AW–6082 at 623 K. The experimental results clearly show that EN AW–6082 hardens during plastic deformation. The extent of hardening depends on the temperature and rate of deformation. The experimental results for different temperatures and head displacement rates presented in Figures 5.1, 5.2 and 5.3 (lines with triangles) show that the hardening effect is more significant at higher rates. The experimental results also show that the hardening effect is more significant at lower temperatures. These results can be explained by considering microstructure evolution during plastic deformation. At higher deformation rates the amount of plastic work stored in the material is higher and therefore more dislocations are generated in the material. These dislocations hinder the plastic deformation and make the material harder. On the other hand, the higher temperature eases the dislocation movement in the microstructure and therefore the material softens and shows less resistance to plastic deformation.

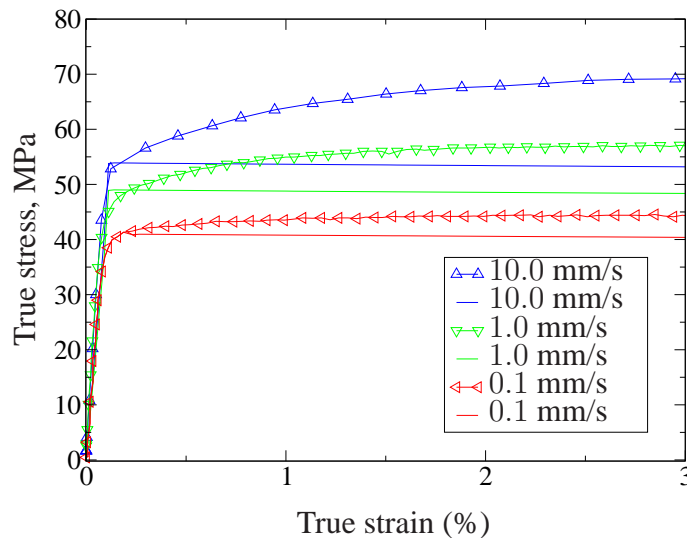


Figure 5.1: Comparison of experimental (lines with triangles) and simulation results of the first model (no hardening) for EN AW–6082 at 623 K for different head displacement rates.

The simulation results of the first model (shown by straight lines in Figures 5.1, 5.2 and 5.3) in contrast to the experimental results show no hardening. The softening effect observed in simulation results is due to the rise in temperature during plastic deformation. In all of the three cases with different temperatures and deformation rates the simulation results predict the elastic part correctly whereas the results are underestimated for the inelastic part .

Figures 5.4, 5.5 and 5.6 present the results of the Orowan based hardening model in comparison to the experimental results of simple tension at different temperatures and deformation rates. In contrast to the first model, here the material hardens after reaching the elastic limit. In

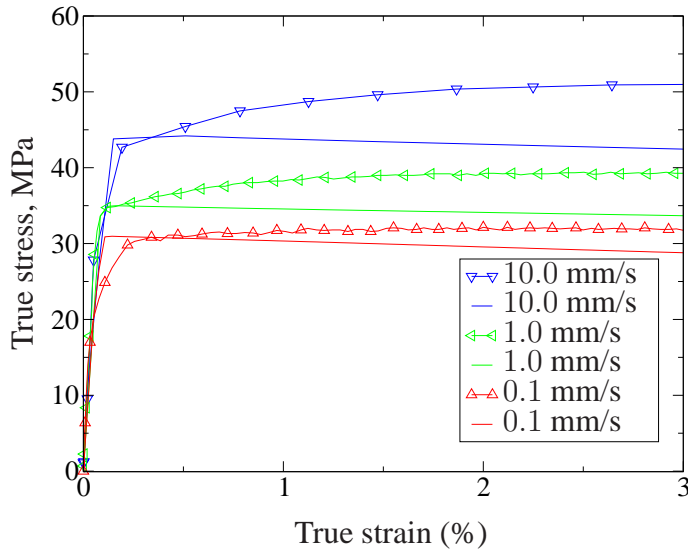


Figure 5.2: Comparison of experimental (lines with triangles) and simulation results of the first model (no hardening) for EN AW-6082 at 673 K for different head displacement rates.

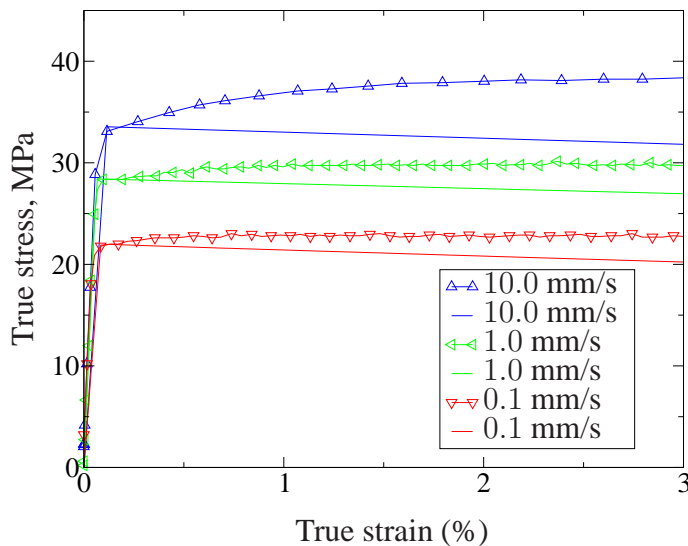


Figure 5.3: Comparison of experimental (lines with triangles) and simulation results of the first model (no hardening) for EN AW-6082 at 723 K for different head displacement rates.

all of the cases the simulated results are in good agreement with experimental ones. At a higher temperature and lower deformation rate the Orowan model predicts the hardening effect more accurately. In each case the saturation value of hardening depends on the temperature and rate of deformation and should be adjusted for each simulation.

To compare the simulated results of the two explained models in the case of the extrusion process, the ram force during extrusion is measured. The experimental process is presented in Figure 4.1. Figure 5.7 shows the experimental results for the ram force during extrusion of EN AW-6082 with ram speed  $v = 5$  mm/s and at 810 K. It is observed from the experiment that the ram force at the beginning of the process (up to 2 mm of ram displacement) increases slightly. This is the time period during which the material fills the gap between the billet and

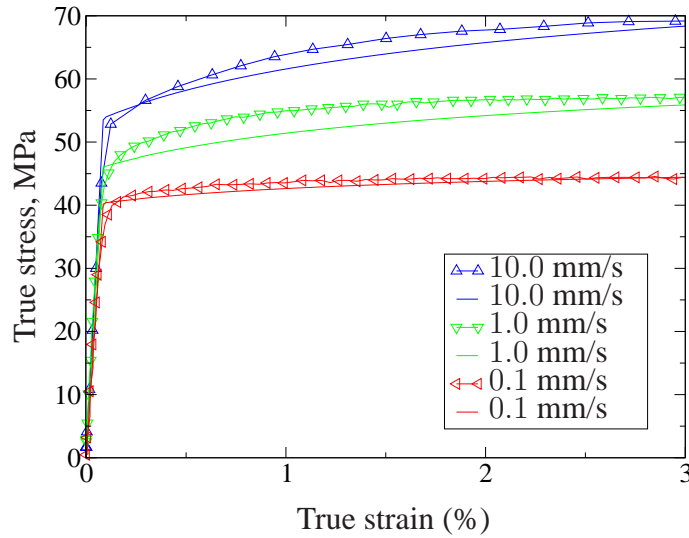


Figure 5.4: Comparison of experimental (lines with triangles) and simulation results of the Orowan based hardening model for EN AW-6082 at 623 K for different head displacement rates.

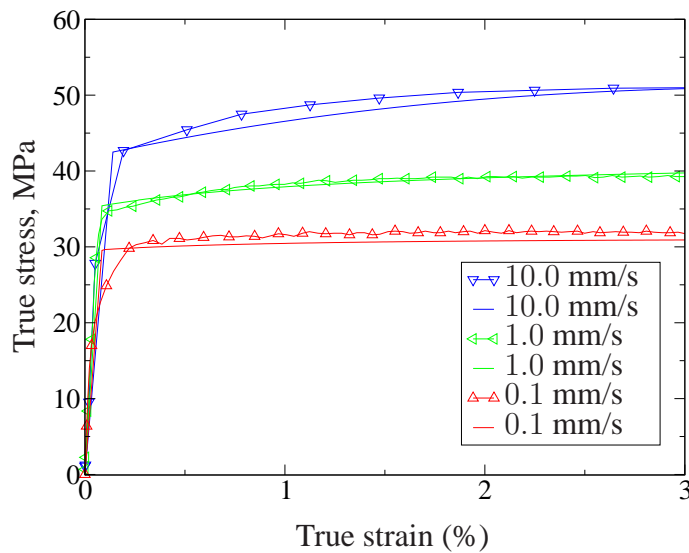


Figure 5.5: Comparison of experimental (lines with triangles) and simulation results of the Orowan based hardening model for EN AW-6082 at 673 K for different head displacement rates.

the container. Thereafter the material starts to flow through the die and the ram force increases linearly. The maximum value of ram force occurs before steady state condition and during the hardening phase of the material. In steady state condition due to the rise in temperature, the material softens, and therefore the final ram force in steady state condition (about 84 kN) is less than the maximum value reached during the hardening phase. The gap between the billet and container is eliminated in simulation, and therefore the simulated ram force starts by linear increasing up to its steady state value. Therefore the simulation results are shifted for comparison with the experimental one. The results of both models show similar behavior in the unsteady part of the process. The first model which does not include the hardening effect

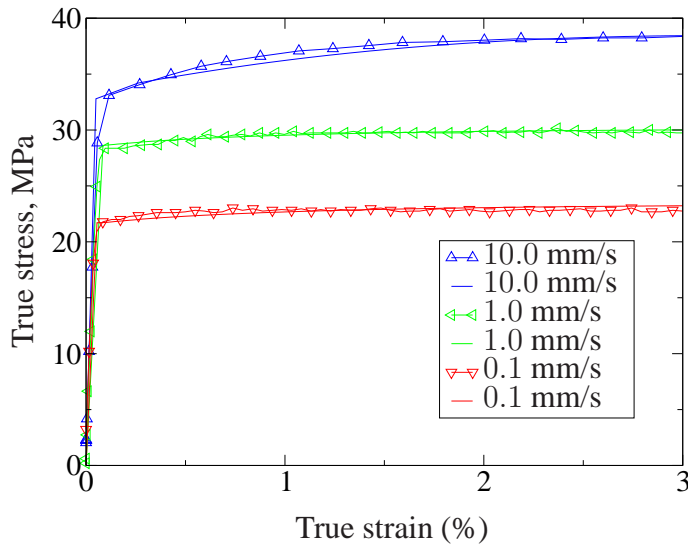


Figure 5.6: Comparison of experimental (lines with triangles) and simulation results of the Orowan based hardening model for EN AW-6082 at 723 K for different head displacement rates.

predicts a lower ram force than experimental results with the maximum ram force in steady state condition, whereas the ram force predicted by the second model is closer to the experimental results. During the extrusion process the dislocation density in highly deformed areas increases and the average grain size decreases. The new dislocations hinder the deformation and increase the required ram force for the deformation. The simulation result of the second model presented in Figure 5.7 shows that the required ram force decreases, after reaching the maximum value during the hardening phase.

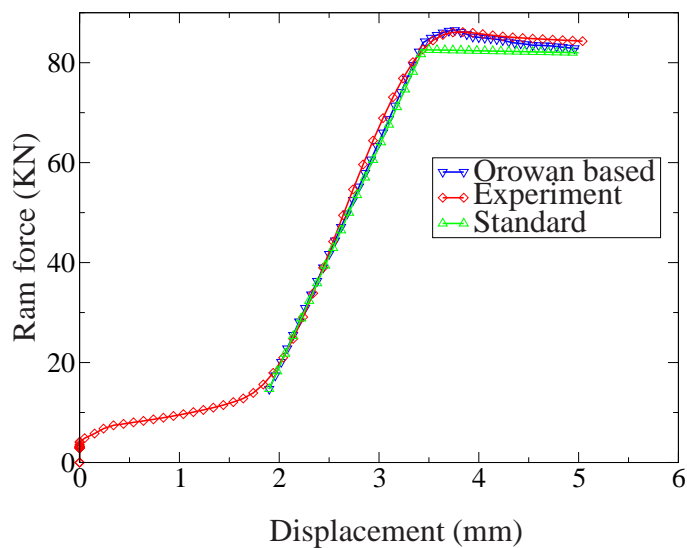


Figure 5.7: Comparison of experimental and simulation results of the ram force during the extrusion process for the two presented models with and without hardening (by courtesy of the IUL, TU Dortmund).

## **5.7 Summary and conclusions**

Two different models based on a thermoelastic viscoplastic approach for the material behavior of aluminum alloys in large deformation processes were presented in this work. The first model ignores the hardening effect due to grain refinement during the forming process. The comparison of simulated results of the first model with experimental simple tension test shows the underestimated simulated results for stress. In the second model a hardening model based on interaction of microstructure and material behavior was presented. According to this model the material hardens with the increasing size of grains. The finer grain size represents the higher density of dislocations in material which hinder the plastic deformation and leads to hardening of the material. The results of this Orowan type model are in good agreement with experimental results of the simple tension test at different temperature and deformation rates. Both models are used in the case of extrusion of aluminum alloy to obtain the ram force. The first model predicts the ram force lower than the experimental one whereas in the second model the predicted ram force is close to the experimental one. Moreover, similar to the experiment, the ram force reaches a maximum value before the steady state condition. This maximum value represents the hardening period of the material.



# Appendix A

## Basics of continuum mechanics

This appendix gives a short description of the continuum mechanics relations which are used in this work. A more detailed explanation of the topics of continuum mechanics can be found in text books such as Chadwick (1999) and Gurtin et al. (2009).

### A.1 Kinematics

The motion of a continuum body  $\Omega$  in the space can be divided in two parts: rigid body displacement which is deformation free, and deformation. In rigid body displacement, the body moves with rotation and displacement without any change in its shape.

The motion of a body from **reference configuration**  $\Omega_r$  to the **current configuration**  $\Omega_c$  can be explained by function  $\Phi(\mathbf{X}, t)$  which transforms every material point of the reference configuration to the current configuration

$$\mathbf{x} = \Phi(\mathbf{X}, t) \quad (\text{A.1})$$

where  $\mathbf{X}$  and  $\mathbf{x}$  are the coordinates of the material point in the reference and current configuration, respectively.

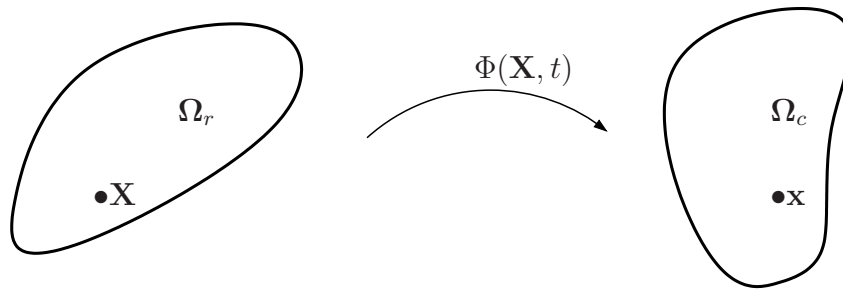


Figure A.1: The motion of a continuum body from its reference configuration  $\Omega_r$  to the current configuration  $\Omega_c$  in Euclidean space.

The vector  $d\mathbf{X}$  in reference configuration can be transformed to vector  $d\mathbf{x}$  in current configuration by

$$d\mathbf{x} = \mathbf{F}d\mathbf{X} \quad (\text{A.2})$$

where  $\mathbf{F}(\mathbf{X}, t)$  is called the **deformation gradient** tensor

$$\mathbf{F}(\mathbf{X}, t) = \frac{\partial \mathbf{x}}{\partial \mathbf{X}} = \frac{\partial \Phi(\mathbf{X}, t)}{\partial \mathbf{X}}. \quad (\text{A.3})$$

Moreover the Jacobian  $J$  of the tensor  $\mathbf{F}$  is obtained by

$$J = \det \mathbf{F}(\mathbf{X}, t). \quad (\text{A.4})$$

and represents the transformation of a volume from reference configuration to the current configuration

$$dv = JdV. \quad (\text{A.5})$$

The deformation gradient  $\mathbf{F}$  can be decomposed to two tensors by polar decomposition:

$$\mathbf{F} = \mathbf{R}\mathbf{U} = \mathbf{V}\mathbf{R} \quad (\text{A.6})$$

where the **rotation tensor**  $\mathbf{R}$  is a proper orthogonal tensor,  $\mathbf{R}\mathbf{R}^T = \mathbf{I}$ , and  $\mathbf{U}$  and  $\mathbf{V}$  are positive definite symmetric tensors called **right** and **left stretch tensor**, respectively. From equation A.6

$$\mathbf{F}\mathbf{F}^T = \mathbf{V}\mathbf{R}\mathbf{R}^T\mathbf{V}^T = \mathbf{V}\mathbf{V}^T = \mathbf{V}^2 \quad (\text{A.7})$$

and

$$\mathbf{F}^T\mathbf{F} = \mathbf{U}^T\mathbf{R}^T\mathbf{R}\mathbf{U} = \mathbf{U}^T\mathbf{U} = \mathbf{U}^2 \quad (\text{A.8})$$

where  $\mathbf{C} = \mathbf{F}^T\mathbf{F} = \mathbf{U}^2$  and  $\mathbf{B} = \mathbf{F}\mathbf{F}^T = \mathbf{V}^2$  are called **right Cauchy-Green tensor** and **left Cauchy-Green tensor**, respectively.

In the case of plastic deformation of the material, the deformation gradient  $\mathbf{F}$  can be decomposed to elastic  $\mathbf{F}_E$  and inelastic part  $\mathbf{F}_P$

$$\mathbf{F} = \mathbf{F}_E\mathbf{F}_P. \quad (\text{A.9})$$

## A.2 Strain

There are two measurements of strain which are most widely used. **Green-St. Venant strain tensor**

$$\mathbf{E} = \frac{1}{2}(\mathbf{F}^T\mathbf{F} - \mathbf{I}) = \frac{1}{2}(\mathbf{C} - \mathbf{I}) \quad (\text{A.10})$$

and **Euler-Almansi strain**

$$\mathbf{e} = \frac{1}{2}(\mathbf{I} - (\mathbf{F}\mathbf{F}^T)^{-1}) = \frac{1}{2}(\mathbf{I} - \mathbf{B}^{-1}). \quad (\text{A.11})$$

Another measure of strain is the logarithmic, or true strain

$$\boldsymbol{\epsilon} = -\frac{1}{2} \ln(\mathbf{F}^{-T}\mathbf{F}^{-1}) = -\frac{1}{2} \ln(\mathbf{B}^{-1}) \quad (\text{A.12})$$

which from equation A.8 can be written as

$$\boldsymbol{\epsilon} = \ln \mathbf{V}. \quad (\text{A.13})$$



Considering the elastic part of the deformation gradient  $\mathbf{F}_E$ , the elastic left Cauchy-Green tensor tensor

$$\mathbf{B}_E = \mathbf{F}_E \mathbf{F}_E^T \quad (\text{A.14})$$

results in

$$\mathbf{V}_E = (\mathbf{F}_E \mathbf{F}_E^T)^{\frac{1}{2}} = (\mathbf{B}_E)^{\frac{1}{2}} \quad (\text{A.15})$$

for the elastic left stretch tensor  $\mathbf{V}_E$  and

$$\ln \mathbf{V}_E = \frac{1}{2} \ln(\mathbf{B}_E) \quad (\text{A.16})$$

for the elastic left logarithmic stretch tensor  $\ln \mathbf{V}_E$ .

### A.3 Stress

Stress is the measurement of the internal forces caused by deformation in a body. The source of deformation can be external forces and displacement as well as temperature changes in a body. Cauchy's theorem of stress states that, as a consequent of balance of forces, a tensor  $\mathbf{T}$  called **Cauchy stress**, exists on an arbitrary cross section of a material body so that

$$\mathbf{t} = \mathbf{T} \mathbf{n} \quad (\text{A.17})$$

where  $\mathbf{t}$  is defined as the ratio of the force  $\Delta \mathbf{f}$ , acting on the cross-sectional area  $\Delta \mathbf{A}$ , and  $\mathbf{n}$  is the normal vector of the surface  $\Delta \mathbf{A}$ . The Cauchy stress tensor  $\mathbf{T}$  should be symmetric to satisfy the balance of angular momentum.

The Kirchhoff stress  $\mathbf{K}$  is one of the popular measurements of stress and is defined as

$$\mathbf{K} = \det(\mathbf{F}) \mathbf{T}. \quad (\text{A.18})$$

Other measurements which can be obtained from Kirchhoff stress  $\mathbf{K}$  are first Piola-Kirchhoff stress

$$\mathbf{P} = \mathbf{K} \mathbf{F}^{-T} \quad (\text{A.19})$$

and second Piola-Kirchhoff stress  $\mathbf{S}$

$$\mathbf{S} = \mathbf{F}^{-1} \mathbf{P}. \quad (\text{A.20})$$

### A.4 Balance equations

Balance laws are physical laws which apply to all material bodies. In continuum mechanics these laws explain the balance of mass, linear momentum, angular momentum and energy in a moving body. The first balance equation is the balance of mass and in local form may written as

$$\dot{\rho} + \rho \operatorname{div} \mathbf{v} = 0 \quad (\text{A.21})$$

where  $\rho$  is the mass density and  $\mathbf{v}$  is the velocity. Balance of linear momentum explains that the change of linear momentum in time is equal to the sum of all external forces acting on the body and is written as

$$\rho \dot{\mathbf{v}} = \operatorname{div} \mathbf{T} + \rho \mathbf{b} \quad (\text{A.22})$$

where  $\mathbf{b}$  represents the body forces per unit of volume. The balance of angular momentum in a spatial integral form can be written as

$$\int_{\partial\Omega} \mathbf{r} \times \mathbf{t} da + \int_{\Omega} \mathbf{r} \times \mathbf{b} dv = \overline{\int_{\Omega} \mathbf{r} \times (\rho \mathbf{v}) dv} \quad (\text{A.23})$$

where  $\mathbf{r}$  is the position vector of the material points with respect to the origin. The Balance of angular momentum equation results in the symmetry of the Cauchy stress tensor  $\mathbf{T}$

$$\mathbf{T} = \mathbf{T}^T. \quad (\text{A.24})$$

The energy balance (or the first law of thermodynamics) asserts that the total energy of the material changes in time due to mechanical work performed by the material on its environment, and heating of the material by its environment. Both of these represent a thermomechanical interaction between the material and its environment. The local form of the first law of thermodynamics can be obtained as

$$\rho \dot{U}_{int} = \mathbf{T} \cdot \mathbf{D} - \operatorname{div} \mathbf{q} + \rho r \quad (\text{A.25})$$

here  $U_{int}$  is the internal energy per unit mass,  $\rho$  the mass density,  $\mathbf{v}$  the velocity,  $\mathbf{T}$  the Cauchy stress,  $\mathbf{b}$  the body forces per unit mass,  $\mathbf{q}$  the heat flux,  $r$  the specific heat source and  $\mathbf{D}$  is the rate of deformation.

# Appendix B

## Microstructure of deformed materials

The aim of this appendix is to give a short overview of different micro-mechanisms which are involved in the large deformation of single-phase metals. More detailed issues on this topic can be found in books such as Humphreys and Hatherly (2004) and Gottstein (2004).

### B.1 Deformed state

The building components of the metals are crystals. Crystals are the repeated arrangement of atoms. The most common crystal structures for metals are face-centered cubic (fcc), body-centered cubic (bcc) and hexagonal closed-pack (hcp). The crystal structure of the material is not ideal and contains imperfections. These imperfections or defects are the irregular arrangement of atoms. There are three different type of defects in the structure of crystals: point defects, line defects (dislocations) and planar defects (grain boundaries). The defects in crystal structures have a significant effect on the behavior of the materials. The microstructure of a polycrystal consists of high-angle grains, subgrains (cells) and dislocations. Grains are characterized as regions with different orientations. The average misorientation angle of both grain and subgrain boundaries increases by accumulation of strain and stress.

There are two methods of deformation in cubic metals: slip and twinning. The deformation method in metals depends on the value of the **stacking fault energy**  $\gamma_{SFE}$ . In metals with high stacking fault energy the deformation may occur by slip whereas in metals with lower values of stacking fault energy, the mobility of dislocations in the crystal structure is lower and twinning is the preferred method of deformation.

During deformation the microstructure of a metal changes in several ways. The grains change their shape and there is a large increase in the total grain boundary area. The new grain boundary area has to be created during deformation and this is done by incorporating some of the dislocations that are continuously created during the deformation process. Plastic deformation in crystals normally occurs by the movement of the dislocations. Grain boundaries are obstacles for movement of dislocations. Therefore finer grains make the material harder.

The energy of plastic deformation is mostly converted to the heat. A small part of this energy causes the microstructure evolutions during and after deformation. The gained energy from deformation is stored in the material in form of dislocations. Because of this, investigation of the deformation microstructure during recovery and recrystallization must be based on the density, distribution and arrangement of dislocations. The dislocations are of two basic types: edge dislocation and screw dislocation. Dislocations are quantitatively represented by the Burgers vector  $\mathbf{b}$ . In the case of edge dislocation the Burgers vector is perpendicular to the dislocation

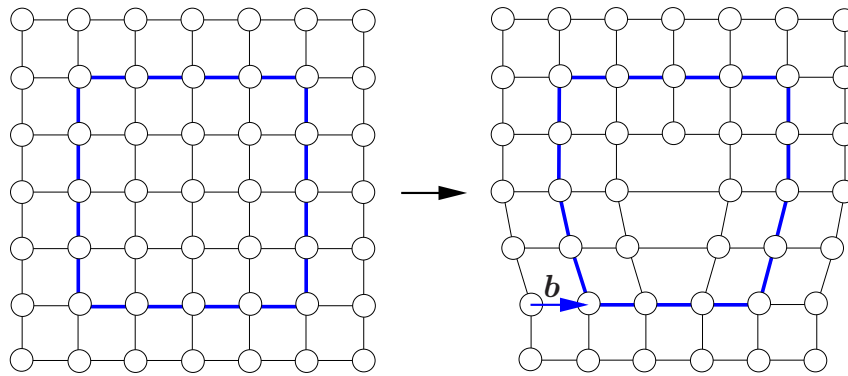


Figure B.1: Edge dislocation in crystal structure. Burgers vector  $\mathbf{b}$  represents the magnitude of the structural defect and is perpendicular to the dislocation line in the case of edge dislocation.

line and in the case of screw dislocation, it is parallel to the dislocation line. The edge dislocation and screw dislocation are presented in Figures B.1 and B.2, respectively. In reality there is a mixed combination of edge and screw dislocations in the crystal structure.

The microstructure evolutions happening during the deformation are categorized as "dynamic evolutions" and those happening after the deformation are called "static evolutions".

The stored dislocations during the plastic deformation hinder the movement of dislocations and cause the material to harden. The dislocations generated during deformation of the material are thermomechanically unstable. During the annealing process the stored energy in microstructure is released and the material softens again. The mechanisms leading to softening during annealing are mainly recovery and recrystallization.

## B.2 Recovery

Recovery can be defined as all annealing processes occurring in deformed materials without the migration of a high angle grain boundary. High angle boundaries are defined as boundaries with misorientations greater than  $15\text{-}20^\circ$  (Bellier and Doherty, 1977). During recovery the dislocations annihilate or rearrange so that the total stored energy decreases. Recovery usually occurs before recrystallization starts. In fact recovery and recrystallization are in competition to minimize the stored energy of deformation. Recovery lowers the driving energy for recrystallization and it can influence the recrystallization process. The dislocation density decreases during recovery and consequently the material ductility increases.

An important parameter affecting the recovery is the stacking fault energy of the material. In metals with low stacking fault energy, the dislocation climb is difficult and therefore the recovery process is very short. On the other hand in metals with high stacking fault energy such as aluminum, the recovery is more significant compared to the recrystallization. Apart from stacking fault energy, temperature is an important factor in the recovery process. Although the dislocations in the deformed grain structure are thermodynamically unstable, the deformed structure is mechanically stable and dislocations have less chance to move at lower temperature.

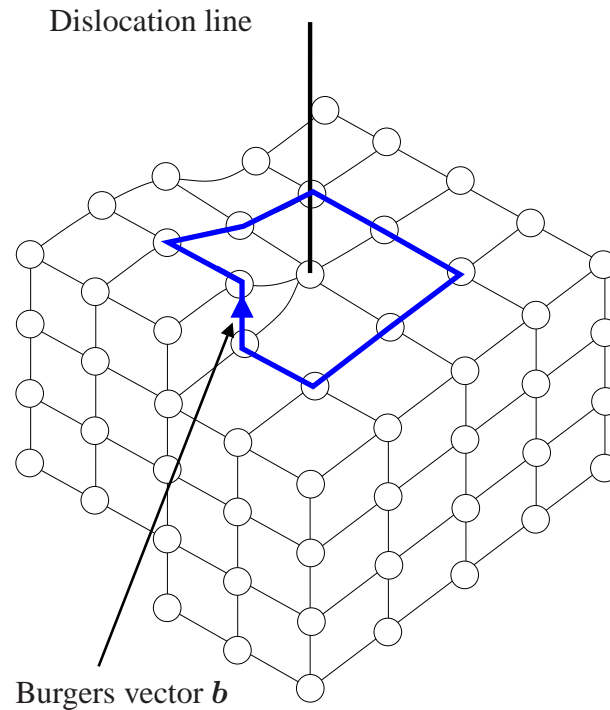


Figure B.2: Screw dislocation in crystal structure. Burgers vector  $b$  is parallel to dislocation line in the case of screw dislocation.

### B.3 Recrystallization

After the recovery is completed, the grains are still in a relatively high strain energy state. Recrystallization is the formation of a new set of strain-free and equiaxed grains with low dislocation densities. These new grains grow and consume the deformed or recovered grains. Recrystallization occurs in two steps: nucleation (the initial formation of new grains) and growth. Nucleation is defined as "crystallite of low internal energy growing into deformed or recovered material from which it separated by a high angle grain" (Humphreys and Hatherly, 2004). The formation of new grains is initiated in deformed subgrains with high local misorientation and larger size (Doherty, 1978). A nucleus is surrounded by a high-angle grain boundary which can grow inside the deformed microstructure.

Burke and Turnbull (1952) have defined the general laws of recrystallization as follows:

- recrystallization can occur only by reaching a minimum level of deformation.
- the smaller the degree of deformation, the higher the temperature necessary for recrystallization.
- increasing the annealing time decreases the temperature necessary for recrystallization.
- the final grain size depends mainly on the degree of deformation and to a lesser extent on the annealing temperature.
- the larger the original grain size, the greater the amount of cold deformation required to give equivalent recrystallization temperature and time.

- the amount of cold work required to give equivalent deformational hardening increases with increasing temperature of working.
- if annealing is continued after recrystallization is complete, the grain size increases.

These rules are based on experimental observations and are valid in most of the cases.

For metals such as aluminum no phase transformation occurs and recrystallization is the only way to form a completely new grain structure. Aluminum alloys generally have low hot worked dislocation densities and therefore DRX normally does not occur in aluminum alloys. However sufficient amount of hard second phase particles can cause nucleation and growth of new grains in aluminum alloys by increasing dislocation density around these particles (McQueen et al., 1984).

Recrystallization might be continuous or discontinuous. In continuous recrystallization, the nucleation and growth occur homogeneously in the material, whereas during discontinuous recrystallization nucleation starts in few points which have reached a high degree of deformation, and with further deformation of the material, the growth of the new grains is hindered by increasing dislocation density.

In aluminum and its alloys during large deformation at elevated temperature, high-angle grain boundaries become closer in one direction although the size of the low-angle grain does not change. During this process the elongated grains serrate and form new equiaxed high-angle grains which are approximately the size of subgrains (Gholinia et al., 2002). This phenomenon is called geometric dynamic recrystallization (GDX) which was introduced by McQueen and also observed by other researchers (McQueen et al., 1985; McQueen et al., 1989; Solberg et al., 1989). During GDX the grains are divided into shorter segments which are hard to distinguish from the subgrains (McQueen, 2001). In the case of aluminum the starting high-angle boundaries are serrated as a result of subgrain boundary formation (Kassner and Barrabes, 2005; Kassner and McMahan, 1987).

## **B.4 Grain growth**

After recrystallization is completed, the structure is still not in the stable condition and the grains may grow. Grain growth can be defined as a process involving the migration of grain boundaries when the driving force for migration is only the reduction of the grain boundary area itself.

Grain growth can be divided to normal grain growth and abnormal grain growth. During normal grain growth the grains grows homogeneously and the grain size is uniform in the material. In abnormal grain growth, some of the grains start to grow at the cost of the other grains with a lower rate of growth.

## **B.5 Measurement of microstructure**

There are several methods to measure the microstructure and texture of the materials. In the current work Electron Backscattered Diffraction (EBSD) method is used for this purpose. In

this method the crystal orientation at each point of the sample is obtained by analyzing the reflected diffraction patterns on a phosphor screen in a scanning electron microscope (SEM). A low light CCD (charge-coupled device) camera records the obtained pattern on the phosphor screen. An image processing system analyses this pattern and determines the related crystal orientation of this pattern (Engler and Randle, 2010). The crystal orientations are given by three Euler angles. In the current work a MATLAB toolbox called MTEX (Quantitative Texture Analysis Software) is used for visualization of the crystal orientations in form of grains.





## References

- Abaqus, Theory manual of Abaqus, version 6.9, 2009.
- Abedrabbo, N., Pourboghrat, F., Carsley, J., Forming of AA5182-O and AA5754-O at elevated temperatures using coupled thermo-mechanical finite element models, *International Journal of Plasticity*, Volume 23, pp. 841–875, 2007.
- Baxter, G. J., Furu, T., Zhu, Q., Whiteman, J. A., Sellars, C. M., The influence of transient strain-rate deformation conditions on the deformed microstructure of aluminium alloy Al-12367–2376, 1999.
- Bellier, S., Doherty, R., The structure of deformed aluminium and its recrystallization–investigations with transmission Kossel diffraction, *Acta Metallurgica*, Volume 25, pp. 521–538, 1977.
- Blum, W., Zhu, Q., Merkel, R., McQueen, H., Geometric dynamic recrystallization in hot torsion of Al–5Mg–0.6Mn (AA5083), *Materials Science and Engineering A*, Volume 205, pp. 23–30, 1996.
- Bontcheva, N., Petzov, G., Microstructure evolution during metal forming processes, *Computational Materials Science*, Volume 28, pp. 563–573, 2003.
- Bontcheva, N., Petzov, G., Parashkevova, L., Thermomechanical modelling of hot extrusion of Al-alloys, followed by cooling on the press, *Computational Materials Science*, Volume 38, pp. 83–89, 2006.
- Burke, J., Turnbull, D., Recrystallization and grain growth, *Progress in Metal Physics*, Volume 3, pp. 220–292, 1952.
- Chadwick, P., *Continuum Mechanics: Concise Theory and Problems*, Dover Publications, Mineola, New York, 1999.
- Chen, L.-Q., Phase-field models for microstructure evolution, *Annual Review of Materials Research*, Volume 32, pp. 113–140, 2002.
- Coupez, T., Fourment, L., Chenot, J., Ladeveze, P., Oden, J., Adaptive solutions in industrial forming process simulation, in *Advances in Adaptive Computational Methods in Mechanics*, Volume 47, pp. 365–381, Elsevier, 1998.
- De Pari Jr., L., Misiolek, W. Z., Theoretical predictions and experimental verification of surface grain structure evolution for AA6061 during hot rolling, *Acta Materialia*, Volume 56, pp. 6174–6185, 2008.
- Doherty, R., A correlation between heterogeneous nucleation activity and melting point ratio for binary metallic systems, *Scripta Metallurgica*, Volume 12, pp. 591–594, 1978.
- Doherty, R. D., Hughes, D. A., Humphreys, F. J., Jonas, J. J., Jensen, D. J., Kassner, M. E., King, W. E., McNelley, T. R., McQueen, H., Rollett, A. D., Current issues in recrystallization: a review, *Materials Science and Engineering A*, Volume 238, pp. 219 – 274, 1997.
- Duan, X., Sheppard, T., Simulation and control of microstructure evolution during hot extrusion of hard aluminium alloys, *Materials Science and Engineering A*, Volume 351, pp. 282–292,

2003.

- Duan, X., Sheppard, T., The influence of the constitutive equation on the simulation of a hot rolling process, *Journal of Materials Processing Technology*, Volume 150, pp. 100–106, 2004.
- Engler, O., Randle, V., *Introduction to Texture Analysis: Macrotecture, Microtexture, and Orientation Mapping*, second edition, CRC Press, New York, 2010.
- Fan, D., Chen, L. Q., Computer simulation of grain growth using a continuum field model, *Acta Materialia*, Volume 45, pp. 611–622, 1997.
- Furu, T., Ørsund, R., Nes, E., Subgrain growth in heavily deformed aluminium—experimental investigation and modelling treatment, *Acta Metallurgica et Materialia*, Volume 43, pp. 2209–2232, 1995.
- Furu, T., Shercliff, H. R., Sellars, C., Ashby, M., *Physically-Based Modelling of Strength, Microstructure and Recrystallisation during Thermomechanical Processing of Al-Mg Alloys*, *Material Science Forum*, Volume 217-222, pp. 453–458, 1996.
- Gautham, B. P., Goyal, S., Gandhe, A., Boundary controlled automatic remeshing for 2D simulation of metal forming, *Journal of Materials Processing Technology*, Volume 134, pp. 108–114, 2003.
- Gholinia, A., Humphreys, F. J., Prangnell, P. B., Production of ultra-fine grain microstructures in Al-Mg alloys by conventional rolling, *Acta Materialia*, Volume 50, pp. 4461–4476, 2002.
- Gosh, S., Finite element simulation of some extrusion processes using the arbitrary Lagrangian-Eulerian description, *Journal of Materials Shaping Technology*, Volume 8, pp. 53–64, 1990.
- Gottstein, G., *Physical Foundations of Materials Science*, Springer-Verlag, Berlin, 2004.
- Grass, H., Kremaszky, C., Reip, T., Werner, E., 3-D Simulation of hot forming and microstructure evolution, *Computational Materials Science*, Volume 28, pp. 469–477, 2003.
- Grong, Ø., Shercliff, H. R., *Microstructural modelling in metals processing*, *Progress in Materials Science*, Volume 47, pp. 163 – 282, 2002.
- Guo, Y., Nakanishi, K., A backward extrusion analysis by the rigid-plastic integralless-meshless method, *Journal of Materials Processing Technology*, Volume 140, pp. 19–24, 2003.
- Gurtin, M. E., Fried, E., Anand, L., *The Mechanics and Thermodynamics of Continua*, Cambridge University Press, Cambridge, 2009.
- Güzel, A., Jäger, A., Parvizian, F., Lambers, H.-G., Tekkaya, A. E., Svendsen, B., Maier, H.-J., A new method for determining dynamic grain structure evolution during hot aluminum extrusion, *Journal of Materials Processing Technology*, submitted, 2011.
- Hinton, E., Campbell, J. S., Local and global smoothing of discontinuous finite element functions using a least squares method, *International Journal for Numerical Methods in Engineering*, Volume 8, pp. 461–480, 1974.

- Humphreys, J., Hatherly, M., Hot Deformation and Dynamic Restoration, in Recrystallization and Related Annealing Phenomena, second edition, 416, Elsevier, Oxford, 2004.
- Hurley, N. D., Geertruyden, W. H. V., Misiolek, W. Z., Surface grain structure evolution in hot rolling of 6061 aluminum alloy, *Journal of Materials Processing Technology*, Volume 209, pp. 5990–5995, 2009.
- Jiang, W., Wang, G., Lu, S., Li, J., Prediction of microstructure evolution of Al-1% Mg alloy during hot forming and sequential heat treatment, *Journal of Materials Processing Technology*, Volume 182, pp. 274–280, 2007.
- Kassner, M., Barrabes, S., New developments in geometric dynamic recrystallization, *Materials Science and Engineering: A*, Volume 410-411, pp. 152–155, 2005.
- Kassner, M., McMahon, M., The dislocation microstructure of aluminum, *Metallurgical and Materials Transactions A*, Volume 18, pp. 835–846, 1987.
- Kayser, T., Parvizian, F., Klusemann, B., Svendsen, B., Experimental and theoretical investigation of the microstructural evolution in aluminium alloys during extrusion, *Computational Methods and Experiments in Materials Characterisation IV*, 209–216, 2009.
- Kobayashi, S., Oh, S.-I., Altan, T., Metal forming and the finite-element method, Oxford University Press, New York, 1989.
- Lou, S., Zhao, G., Wang, R., Wu, X., Modeling of aluminum alloy profile extrusion process using finite volume method, *Journal of Materials Processing Technology*, Volume 206, pp. 481–490, 2008.
- Mahnken, R., Schneidt, A., A thermodynamics framework and numerical aspects for transformation-induced plasticity at large strains, *Archive of Applied Mechanics*, Volume 80, pp. 229–253, 2010.
- McQueen, H. J., Dynamic Recovery and Recrystallization, in Buschow, K. H. J., Cahn, R. W., Flemings, M. C., Ilchner, B., Kramer, E. J., Mahajan, S., Veyssi re, P. (editors), *Encyclopedia of Materials: Science and Technology*, 2375 – 2381, Elsevier, Oxford, 2001.
- McQueen, H. J., Celliers, O., Application of hot workability studies to extrusion processing: Part II. Microstructural development and extrusion of Al, Al-Mg, AND Al-Mg-Mn Alloys, *Canadian Metallurgical Quarterly*, Volume 35, pp. 305–319, 1996.
- McQueen, H. J., Celliers, O., Application of hot workability studies to extrusion processing. Part III: Physical and mechanical metallurgy of Al-Mg-Si and Al-Zn-Mg alloys<sup>5</sup>, *Canadian Metallurgical Quarterly*, Volume 36, pp. 73–86, 1997.
- McQueen, H. J., Evangelista, E., Bowles, J., Crawford, G., Hot deformation and dynamic recrystallization of Al-5Mg-0.8Mn alloy, *Metal science*, Volume 18, pp. 395–402, 1984.
- McQueen, H. J., Knustad, O., Ryum, N., Solberg, J., Microstructural evolution in Al deformed to strains of 60 at 400 C, *Scripta Metallurgica*, Volume 19, pp. 73–78, 1985.
- McQueen, H. J., Poschmann, I., Subgrain development in hot working of Al and Al-5Mg, *Materials Science and Engineering A*, Volume 234-236, pp. 830–833, 1997.

- McQueen, H. J., Solberg, J., N. Ryum, N., Nes, E., Evolution of flow stress in aluminium during ultra-high straining at elevated temperatures. Part II, *Philosophical Magazine A*, Volume 60, pp. 473–485, 1989.
- Nes, E., Constitutive laws for steady state deformation of metals, a microstructural model, *Scripta Metallurgica et Materialia*, Volume 33, pp. 225–231, 1995.
- Nes, E., Furu, T., Application of microstructurally based constitutive laws to hot deformation of aluminium alloys, *Scripta Metallurgica et Materialia*, Volume 33, pp. 87–92, 1995.
- Nes, E., Marthinsen, K., Modeling the evolution in microstructure and properties during plastic deformation of f.c.c.-metals and alloys - an approach towards a unified model, *Materials Science and Engineering A*, Volume 322, pp. 176–193, 2002.
- Parvizian, F., Güzel, A., Jäger, A., Lambers, H.-G., Svendsen, B., Tekkaya, A. E., Maier, H.-J., Modeling of dynamic microstructure evolution of EN AW-6082 alloy during hot forward extrusion, *Computational Materials Science*, Volume 50, pp. 1520–1525, 2011.
- Parvizian, F., Kayser, T., Hortig, C., Svendsen, B., Thermomechanical modeling and simulation of aluminum alloy behavior during extrusion and cooling, *Journal of Materials Processing Technology*, Volume 209, pp. 876–883, 2009.
- Parvizian, F., Schneidt, A., Svendsen, B., Mahnken, R., Thermomechanically coupled modeling and simulation of hot metal-forming processes using adaptive remeshing method, *GAMM-Reports*, Volume 33, pp. 801–813, 2010.
- Rollett, A., Srolovitz, D., Doherty, R., Anderson, M., Computer simulation of recrystallization in non-uniformly deformed metals, *Acta Metallurgica*, Volume 37, pp. 627–639, 1989.
- Rosakis, P., Rosakis, A. J., Ravichandran, G., Hodowany, J., A thermodynamic internal variable model for the partition of plastic work into heat and stored energy in metals, *Journal of the Mechanics and Physics of Solids*, Volume 48, pp. 581–607, 2000.
- Saha, P., Aluminum extrusion technology, first ed., ASM International, Materials Park, Ohio, 2000.
- Schikorra, M., Donati, L., Tomesani, L., Kleiner, M., Microstructure analysis of aluminum extrusion (Part I): Grain size distribution in AA6060, AA6082 and AA7075 alloys, in *Proceedings of Advances in Materials and Processing Technologies*, Korea, 2007a.
- Schikorra, M., Donati, L., Tomesani, L., Kleiner, M., The role of friction in the extrusion of AA6060 aluminum alloy, process analysis and monitoring, *Journal of Materials Processing Technology*, Volume 191, pp. 288–292, 2007b.
- Schikorra, M., Donati, L., Tomesani, L., Tekkaya, A., Microstructure analysis of aluminum extrusion: grain size distribution in AA6060, AA6082 and AA7075 alloys, *Journal of mechanical science and technology*, Volume 21, pp. 1445–1451, 2007c.
- Schikorra, M., Donati, L., Tomesani, L., Tekkaya, E., Microstructure analysis of aluminum extrusion: grain size distribution in AA6060, AA6082 and AA7075 alloys, *Journal of Mechanical Science and Technology*, Volume 21, pp. 1445–1451, 2007d.

- Schikorra, M., Donati, L., Tomesani, L., Tekkaya, E., Microstructure analysis of aluminum extrusion (Part II): Prediction of microstructure on AA6060 alloy, in Proceedings of Advances in Materials and Processing Technologies, Korea, 2007e.
- Schikorra, M., Lambers, H., Donati, L., Maier, H., Tomesani, L., Tekkaya, A., Microstructure Development during Extrusion of AA6060, AA6082 and AA7075 alloys, in Proceedings of the 9th International Conference on Technology and Plasticity, 1471–1477, Gyeongju, Korea, 2008.
- Sellars, C. M., Microstructural evolution during thermomechanical processing, in Chandra, T., Sakai, T. (editors), International Conference on Thermomechanical Processing of Steel & Other Materials (THERMEC'97), 3–11, 1997.
- Sellars, C. M., Zhu, Q., Microstructural modelling of aluminium alloys during thermomechanical processing, Materials Science and Engineering A, Volume 280, pp. 1–7, 2000.
- Sheppard, T., Prediction of structure during shaped extrusion and subsequent static recrystallisation during the solution soaking operation, Journal of Materials Processing Technology, Volume 177, pp. 26–35, 2006.
- Shercliff, H. R., Lovatt, A. M., Modelling of microstructure evolution in hot deformation, Philosophical Transactions of the Royal Society A: Mathematical, Physical and Engineering Sciences, Volume 357, pp. 1621–1643, 1999.
- Solberg, J., McQueen, H., Ryum, N., Nes, E., Influence of ultra-high strains at elevated temperatures on the microstructure of aluminium, Part I, Philosophical Magazine A, Volume 60, pp. 447–471, 1989.
- Steinbock, K., Weidig, U., Scholtes, B., Zinn, W., Innovative flexible metal forming processes based on hybrid thermo-mechanical interaction, Steel research international, Volume 76, pp. 154–159, 2005.
- Svendsen, B., On the modelling of anisotropic elastic and inelastic material behaviour at large deformation, International Journal of Solids and Structures, Volume 38, pp. 9579–9599, 2001.
- Vatne, H. E., Furu, T., Ørsund, R., Nes, E., Modelling recrystallization after hot deformation of aluminium, Acta Materialia, Volume 44, pp. 4463–4473, 1996.
- Velay, X., Prediction and control of subgrain size in the hot extrusion of aluminium alloys with feeder plates, Journal of Materials Processing Technology, Volume 209, pp. 3610–3620, 2009.
- Weidig, U., Hübner, K., Steinbock, K., Scholtes, B., Zinn, W., Bulk Steel Products with Functionally Graded Properties Produced by Differential Thermo-mechanical Processing, Steel research international, Volume 79, pp. 59–65, 2008.
- Williams, A., Croft, T., Cross, M., Computational modelling of metal extrusion and forging processes, Journal of Materials Processing Technology, Volume 125-126, pp. 573–582, 2002.
- Wriggers, P., Computational contact mechanics, second edition, Springer-Verlag, Berlin, 2006.

- Yassar, R. S., Murphy, J., Burton, C., Horstemeyer, M. F., Kadiri, H. E., Shokuhfar, T., Microstructure history effect during sequential thermomechanical processing, *Materials Science and Engineering: A*, Volume 494, pp. 52–60, 2008.
- Zhang, H., Li, L., Yuan, D., Peng, D., Hot deformation behavior of the new Al-Mg-Si-Cu aluminum alloy during compression at elevated temperatures, *Materials Characterization*, Volume 58, pp. 168–173, 2007.
- Zhu, Q., Shercliff, H. R., Sellars, C. M., Modelling hot deformation behaviour based on evolution of dislocation substructure, in Chandra, T., Sakai, T. (editors), *International Conference on Thermomechanical Processing of Steel & Other Materials (THERMEC'97)*, 2039–2045, 1997.
- Zienkiewicz, O., Zhu, J., The superconvergent patch recovery (SPR) and adaptive finite element refinement, *Computer Methods in Applied Mechanics and Engineering*, Volume 101, pp. 207–224, 1992.
- Zienkiewicz, O. C., Zhu, J. Z., Superconvergence and the superconvergent patch recovery, *Finite Elements in Analysis and Design*, Volume 19, pp. 11–23, 1995.

# Acknowledgments

The work presented in this thesis was carried out between 2006 and 2011 during my time as a Ph.D. student at the Institute of Mechanics, Technical University of Dortmund. Having come to the end, I would like to express my thanks to all the people here who gave me tremendous support and help during these years.

First of all I would like to sincerely thank my academic advisor, Professor Bob Svendsen, for his scientific support during my Ph.D. work. Without his kind support and advice this thesis could not be accomplished.

Moreover, I would like to thank Professor Rolf Mahnken, Jun. Prof. Björn Kiefer and Professor Dirk Biermann for their interest in my work and willingness to act as examiners of this thesis. I would also like to thank Professor A. Erman Tekkaya for taking the chairmanship of the examination committee.

My special thanks go to my dear colleagues Mr. Tobias Kayser and Dr. Christian Hortig for their close cooperation, scientific discussions and sharing ideas for improving my work and for the friendly working atmosphere. I would like to thank my fellow workers Dr. Benjamin Klusemann and Mr. Till Clausmaier for their support and friendliness during these past years.

I would also like to thank Mr. Andreas Jäger and Mr. Ahmet Güzel, from the Institute of Forming Technology and Lightweight Construction (IUL), for their excellent work in performing the extrusion experiments and providing the required experimental data for verification of the modeling and simulation results in this work.

My special thanks would go to Ms. Kerstin Walter for her years of warm support regarding administrative issues. Sincere thanks to Ms. Christine Vu, Ms. Daria Walencyk and Ms. Christina McDonagh for their great language support and the correction of my thesis and papers.

I would also like to thank all of other members of the Institute of Mechanics for their support and friendliness.

Last but not least I would like to thank my family, especially my mother, for their moral support during these past years.

Dortmund, April 2011

Farhad Parvizian





# Curriculum Vitae

## Personal

Name: Farhad Parvizian  
Date of Birth: February 02, 1981  
Place of Birth: Esfahan, Iran  
Nationality: Iranian

## Education and Experience

1995-1999 High school, Esfahan, Iran  
1999-2003 B.Sc. in Mechanical Engineering, Department of Mechanical Engineering,  
Esfahan University of Technology, Esfahan, Iran  
2003-2005 M.Sc. in Computational Engineering, Ruhr University of Bochum, Germany  
2006-2011 Research fellow, Institute of Mechanics, TU Dortmund, Germany

